Electrical Stimulation Can Reintroduce Non-Exercise Daily Activity into an Astronaut's Day in Order to Further Reduce Bone Loss

Thomas J. Abitante[1,2], Dava J. Newman[4], Kevin R. Duda[3]

[1]Harvard-MIT Health Sciences and Technology, [2]Draper Scholar, The Charles Stark Draper Laboratory, Inc. [3]The Charles Stark Draper Laboratory, Inc. [4]The MIT Media Lab

ABSTRACT

For a long duration mission to Mars, the current exercise regimen does not mitigate bone loss to a degree that will adequately reduce the risk of a lower body bone fracture. This is in part because astronauts experience negligible skeletal loading outside of exercise and are missing the high number of lower magnitude events that occur on Earth. In order to add more skeletal loading, more exercise is not desirable due to the high caloric demand. Neuromuscular electrical stimulation (NMES) is a technique that causes muscular contractions, but the feasibility of NMES as a spaceflight bone loss countermeasure is unknown. In order to determine feasibility, first the potential efficacy must be determined. This was accomplished with a strain model, as strain is the primary driver of bone health, and by comparing the strain to other activities that have been investigated for long term bone loss prevention. Second, it must be determined if NMES addresses the shortcomings of additional exercise, specifically caloric expenditure. The results of our studies show that NMES could effectively replicate the strains of low impact activity at a low metabolic cost, implying that it is a viable solution to add numerous low impact loading events to the skeleton throughout a day, improving outcomes without significant caloric expenditure, effectively reintroducing non exercise daily activity into an astronaut's day.

INTRODUCTION

- Astronauts lose bone as a result of microgravity and currently use a rigorous exercise regimen to reintroduce loading and mitigate the loss[1].
- Despite the efficacy of exercise, deficits and other structural changes still occur[2] at a rate that could result in a fracture on a long duration mission to Mars[3], in due part to a total absence of the high volume of lower magnitude loading events that occur on Earth as a result of typical, non exercise activity
- The addition of more exercise could result in negative caloric balances, hindering the effects[4], as well affect other operational/logistical needs.
- Neuromuscular Electrical Stimulation (NMES) creates involuntary muscle contractions, that subsequently load the skeleton and could be utilized as a non exercise based countermeasure[5,6]

METHODS

Potential Efficacy

- The maximum tolerable isometric force of the Rectus Femoris and Hamstrings during NMES was measured with a knee dynamometer
- Biomechanical models and a Finite Element Analysis Model were utilized to determine the peak strain on the proximal femur from these contractions
- These peak strains were qualitatively compared to various activities (low impact, high impact, resistance) to determine potential efficacy.

Caloric Deficit Risk

- A metabolic analysis was performed, calculating the percent increase, relative to rest, in the metabolic cost during 5 minutes of repetitive electrical stimulation at various cadences to the thighs and lower legs.
- These metabolic costs were compared to walking at various speeds, to determine whether a NMES countermeasure would incur a caloric cost like that of exercise, or non exercise activity.

RESULTS

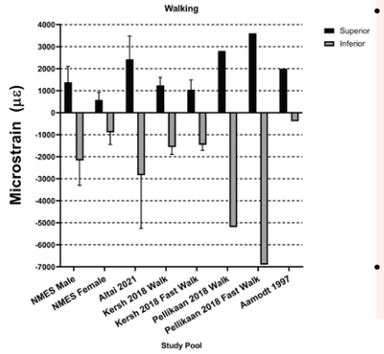

Figure 1. Peak strains of males (n=5) and females (n=5) in the proximal femur during isometric contractions of the rectus femoris and hamstrings, compared to the peak strains modeled during walking from various studies[7,8,9,10].

- The results of the strain model and qualitative comparison showed that NMES could create similar strains at the proximal femur to that during low impact activity like walking (Figure 1) or stair ascending/descending, but could not create strains like that during exercise (running, jumping, resistance training).
- Males had greater strains compared to females

- The results of the metabolic analysis (Figure 2) show that the percent increase in metabolic cost, normalized to body weight (M_{bw}), from NMES to the lower body at the fastest cadence (75 reps in 5 minutes), was significantly less than that of slow walking (2mph). ***p<0.05***
- There was no significant difference in the increase in metabolic cost between any of the three NMES cadences (1 second on and 5 v. 4 v. 3 seconds rest)

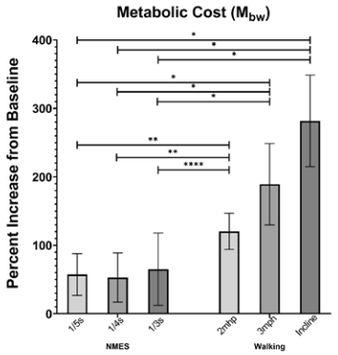

Figure 2. Increase in metabolic cost relative to resting during 3 different NMES cadences (1/5s denotes 1 second contraction with 5 second rest), compared to the increase during walking at various intensities (incline speed – 2mph). n=10
p<0.001, **p<0.005, ****p<0.05

DISCUSSION

- The strains produced during NMES to the thighs created strain similar to non exercise like activity (walking, stairs). Therefore, it could not be used to replace some of the current exercise regimen. Rather it could be used as a supplement to add more lower impact loading throughout the day. The results were highly variable, likely due to numerous physiological factors that effect NMES power and comfort, implying the efficacy would be highly individualized.
- As the metabolic cost of NMES was found to be less than that of slow walking, a regimen that introduces numerous short sets of NMES to the lower body throughout a day will unlikely risk negative caloric balance[11].
- These results highlight the feasibility of adding numerous short NMES sets throughout a given day. This could add hundreds of loading cycles to the lower body skeleton, increasing the loading stimulus. The increased distribution of loading throughout a day will better replicate the loading pattern experienced on Earth, potentially improving the results[12] and further reducing the risk of fracture on a Mars mission[1,2,3]

CONCLUSIONS

- In order to further reduce the bone loss and fracture risk on a mission to Mars, non exercise based methods to load the skeleton may be required.
- NMES presents itself as a tool that can load the skeleton in a manner where the magnitude and metabolic cost of the contractions could effectively reintroduce the non exercise daily activity that is missing from an astronauts day.

References

1. Gabel et al *Br J Sp Med* 2021
2. Vico et al *JBMR* 2017
3. Sibonga et al *HRP* 2017
4. Laurens et al *Front Physiol* 2019
5. Maffiuletti et al *Front Physiol* 2019
6. Dudley-Javoroski *Phy Ther* 2012
7. Altai et al *PLoS One* 2021
8. Kersh et al *JBMR* 2018
9. Pellikaan et al *PLoS One* 2018
10. Aamodt et al *J Ortho Res* 1997
11. Scott et al *Sci Rep I* 2020
12. Robling et al *JBMR* 2002

Thermal Spike Activated Radiation Effects in Microelectronics

Paul Johnson[1], Daniel Valencia[2], Sukesh Aghara[1]

[1]University of Massachusetts Lowell – Nuclear Engineering, [2]Draper

ABSTRACT

Space radiation has been conjectured to cause data retention loss by single event upset (SEU) in spintronic magnetoresistive random access memory (MRAM), but no solution exists to predict the MRAM heavy ion SEU rate beyond expensive heavy ion testing. A new framework with transition state modeling from ferromagnetic state obtains the same order of magnitude SEU probability as testing but predicts the threshold linear energy transfer (LET) approaching zero, which contradicts prior industry literature of immunity of this technology to ionizing radiation.

MOTIVATION

Space exploration and industrialization

Uncrewed Systems	Earth Imaging/Sensing
	Telecommunication
	GPS
	In-Situ Resource Utilization
	Satellite Repair and Cleanup
	Manufacturing
	Space-Based Solar Power
Crewed Systems	Life Support
	Command and Control
	Guidance and Navigation

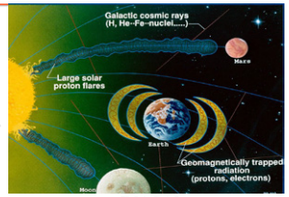

[NASA]

RESEARCH AREA

Space radiation effects in electronics

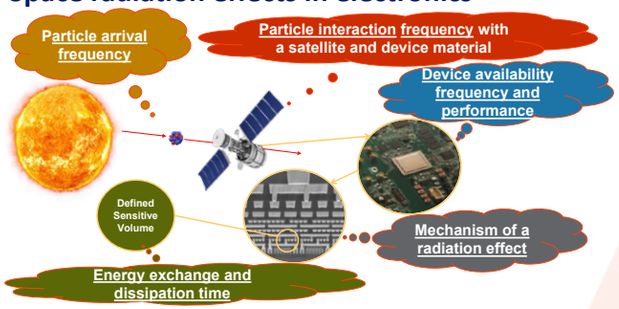

TECHNOLOGY COMPARISON

Random access memory solar flare SEU rates

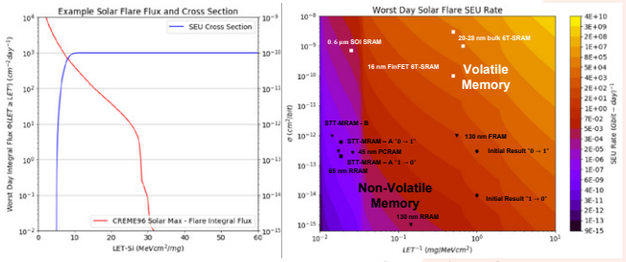

[Data sources by request]

RESEARCH GAP

SEU in spintronic MRAM

- **Data retention:** Emerging non-volatile memory maintain data with a caloric energy barrier separating ferromagnetic thin film from reaching susceptible paramagnetic state

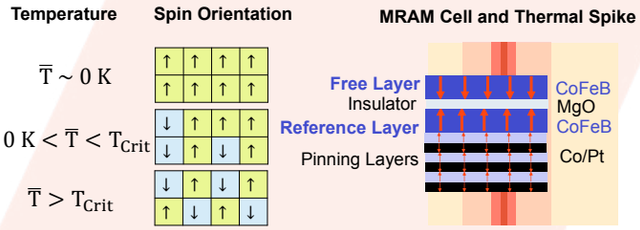

Bit "1" : Anti-parallel = High
Bit "0" : Parallel = Low

- **Space Radiation Modeling Literature:**
  - Min. LET for SEU varies in cell diameter [Kob17]
  - Heavy ion thermal spike leads to $T > T_{Crit}$ [Coi21]
- **Test Literature (USN [Mar21], JAEA [Wat20])** :
  - Threshold linear energy $\in (50 - 60)$ MeVcm^2/mg
- **Reliability Literature (Write/Read/Retention)**:
  - Kinetic models exist for failures in time analysis [Khv13]

METHODOLOGY

Hypothesis: Kinetic rate equations resolve ferromagnetic phase transition and SEU

- **Model input is MRAM reliability data [Avalanche]**
- **Phase transition w/ temperature over $T_{Crit} \in 500 - 1300$ K**
- **Heating by inf. line source given LET from $10^{-16} - 10^{-9}$ s**

Cross section density | Activation rate | Dependence on extent δ | Heating rate | Extent change w/ temperature

$$\frac{d\sigma_{SEU}}{dt} = A_{Irrad}\frac{dP_{ev}}{dt} = \left(f_0\, e^{-\frac{E_a(T)}{k_B T}} f(\delta)\right)_T + \frac{dT}{dt}\frac{df(\delta)}{dT}$$

INITIAL RESULTS

Analytic solution and test data cross section

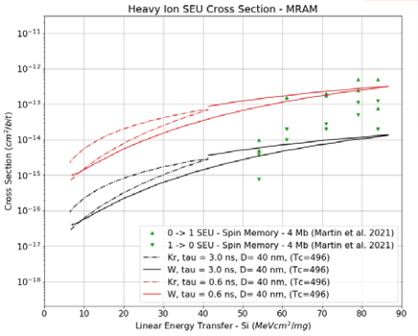

- **Initial model predicts thermal spike causes SEU:**
  - Higher rate for SEU with $0 \rightarrow 1$ transition
  - Possible no minimum linear energy transfer for SEU

ONGOING RESEARCH

Confirm no threshold LET for SEU

- **Uncertainty reduction method – Expected result:**
  - Microdosimetry simulation – Variance in LET of ~100%
  - 2,3 temperature simulation – Increased threshold LET
  - Reliability test – Worse data retention for chip than theory
  - MRAM heavy ion test – Reduced threshold LET

SIGNIFICANCE

General study of single event activation (SEA)

- **Low energy non-ionizing particles may also cause SEU**
- **SEA model applications to other radiation-reliability effects**

ACKNOWLEDGMENTS

- **A special thank you to the Draper Scholar Program, and individuals: Sukesh Aghara, Douglas Martin, Duane Larsen, Bill Schmitt, Jim Bickford, and Steve Scoppettuolo**

[Mac70] Maccallum J. and Tanner J., "Derivation of the Rate Equations used in Thermogravimetry," *Nature*, pp. 1127-1128, 1970
[Vin76] Vineyard G.,"Thermal spikes and activated processes," *Radiation Effects*, vol. 29, no. 4, pp. 245-248, 1976.
[Khv13] Khvalkovskiy et al. "Basic Principles of STT-MRAM cell operation in memory arrays", J. Phys. D: Appl. Phys. 46 074001, 2013.
[Kob17] Kobayashi D. et al. "Soft errors in 10-nm-scale magnetic tunnel junctions exposed to high-energy heavy-ion radiation", JJAP, vol. 56, no. 8, pp. 0802B4, 2017.
[Avalanche] "Endurance, Data Retention and Field Immunity of STT-MRAM", https://www.avalanche-technology.com/.
[Mar21] Martin D. et al. "Single-Event Effects in STT MRAM," 2021 IEEE 32nd Magnetic Recording Conference (TMRC), Pittsburgh, PA, USA, pp. 1-2, 2021.
[Coi21] Coi et al."SEU Mechanisms in Spintronic Devices: Critical Parameters and Basic Effects," in *IEEE TNS*, vol. 68, no. 8, pp. 1533-1541, Aug. 2021.

UMASS LOWELL DRAPER

Towards Autonomous Pole Estimation of Small Bodies

Koundinya Kuppa[1,*], Jay W. McMahon[1], and Ann B. Dietrich[2]

[1]University of Colorado, Boulder, [2]The Charles Stark Draper Laboratory, Inc., *Draper Scholar

ABSTRACT

Knowing the pole (spin) axis of an asteroid is vital to autonomous asteroid exploration and is useful for proximity navigation and shape modeling efforts. Current ground-based methods of pole estimation are time and data intensive and result in estimates with significant uncertainties. We present a new method of obtaining this information from on-board spacecraft imagery. The pole is estimated with infrared images and the camera-asteroid geometry without requiring a prior estimate. The method was tested on simulated infrared images of asteroids Bennu and Itokawa as well as infrared images of asteroid Ryugu from JAXA's Hayabusa2 mission. The average pole errors on Bennu and Itokawa images were approximately 2° and 6°, respectively. The pole estimate error on the Ryugu images was approximately 9°. This algorithm can form an important part of an autonomous navigation solution.

INTRODUCTION

- Ground-based pole estimation methods for small bodies, such as asteroids, incur significant data and resource cost and still may result in **large pole estimate uncertainties** (~5° and 30°) *[Hanus,2011]*
- Stereo-photoclinometry (SPC) or stereo-photogrammetry (SPG) use on-board data to estimate both the pole axis and shape. These can also be data intensive and also require an initial guess of the pole axis
- The method presented here **utilizes on-board infrared (IR) images** and accurately estimates the pole **without requiring a prior**.
- IR images are preferred over optical since they are **insensitive to lighting conditions** and are often part of spacecraft as they are used for achieving scientific objectives

METHODS

- A parameterized thermal model is used to efficiently generate simulated infrared images. Models the temperature increases/decreases of the asteroid as exponential functions. Figure 1 shows sample IR images of Bennu and Itokawa.
- The pole axis $\hat{\boldsymbol{u}}_P$ and the camera geometry are related by the projection of the latitude line (a circle around $\hat{\boldsymbol{u}}_P$) onto the image plane. Circular latitude lines project as ellipses into the camera frame. These ellipses encode the pole axis and camera geometry (Figure 2)
- Figure 3 shows the image processing procedure used to obtain projected ellipse(s)

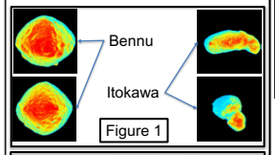

Figure 1

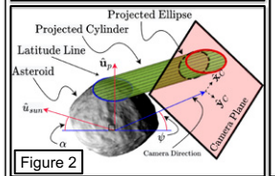

Figure 2

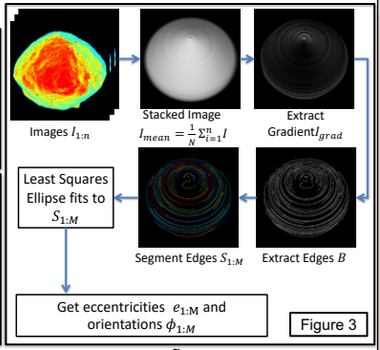

Figure 3

- From $e_{1:M}$ and $\phi_{1:M}$, get weighted average $\bar{e}$ and $\bar{\phi}$ (angle between camera x-axis and the ellipse minor axis). Weights are computed using the length of the given edge segment. Then, the pole estimate is given by:

$$\hat{\boldsymbol{u}}_P = \sqrt{1-\bar{e}}\,\hat{\boldsymbol{n}}_B + \bar{e}\left[cos\bar{\phi}, sin\bar{\phi}, 0\right]^T$$

$\hat{\boldsymbol{n}}_B$: Camera boresight

RESULTS

- Applied method to 201 simulated images of Bennu (Figure 4,5) and Itokawa (Figure 6,7) at different observer latitudes and axial tilts (ψ and α on Figure 2)
- The **average errors were 2°** (for Bennu) and **6°** (for Itokawa) Maximum errors were approximately **9°** (Bennu) and **15°** (Itokawa)

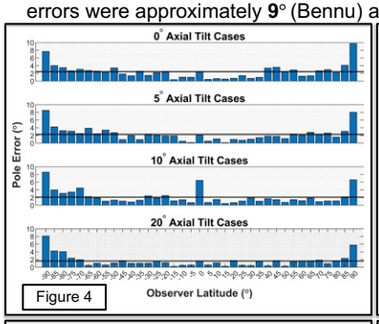

Figure 4

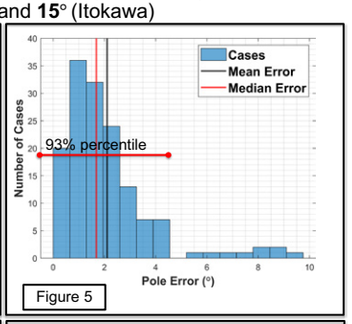

Figure 5

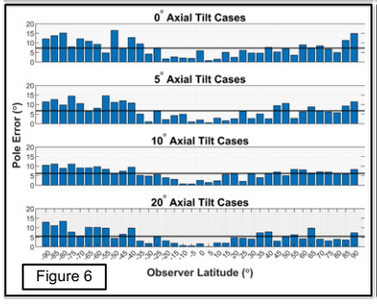

Figure 6

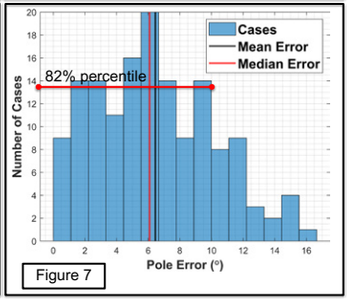

Figure 7

- Method is applied to 64 images of asteroid Ryugu (from the TIR camera on the Hayabusa2 spacecraft). Figure 8 shows the results of the processing procedure for these images (at **observer latitude of ~0°**). Ellipse fitting is applied to the rightmost image. Using the resultant **eccentricity and orientation** with a resultant pole error of 8.8069°.

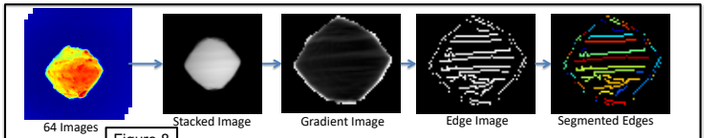

Figure 8

DISCUSSION

- Performance is worse at polar observer latitudes (around ±90°). Occurs due to the sensitivity of the ***eccentricity*** of the least-squares fits of the projected ellipses
- Reducing this "eccentricity sensitivity" would yield improvements in performance
- Bennu results are better than Itokawa (**by about 4° on average**) due to algorithm sensitivity to the asymmetric shape of Itokawa (see Figure 1)
- Approximately **93%** of the Bennu pole estimates are within 5° of the true pole axis (Figure 5). 5° is the "best-case" uncertainty from the ground-based methods
- Approximately **82%** of the Itokawa pole estimates are within 10° of the true pole axis (Figure 7)
- Both Bennu and Itokawa are **significantly better** than the average ground-based uncertainties of about **17°**
- Pole estimate for Ryugu was worse compared to Bennu and Itokawa at the same observer latitude (on **average 5.75° worse**). Difference in performance is fewer images used and lower image resolution (248x328 for Ryugu, 550x550 in the simulated cases)

CONCLUSIONS

- Developed a computationally efficient and robust pole estimation method that utilizes on-board infrared images
- Demonstrated performance on realistic simulated images and on real infrared images. Results show improved performance compared to existing ground-based methods
- This method could be extended for RPOD scenarios to characterize the pole of an uncooperative space object
- Expands the knowledge of infrared imagery and help inform its utility for terrain-relative navigation in light-constrained environments
- This algorithm could form an integral part of an **autonomous navigation and shape modeling** solution for missions to asteroids

ACKNOWLEDGMENTS OR REFS

- Hanuš, J. et al, "*A study of asteroid pole-latitude distribution based on an extended set of shape models derived by the lightcurve inversion method*," Astronomy & Astrophysics, 2011, p.A134.
- Kuppa, K. et al. "*Pole Axis and Spin Direction Estimation of Asteroids Without a Prior using Infrared Imagery*," AIAA Journal of Guidance Control & Dynamics, **(in preparation)**

Brain-on-chip Model for Characterization of Diagnostic Biomarkers and Evaluation of Therapeutics for TBIs

Peter Hsi[1,2,3], David L. Kaplan[3], Vishal Tandon[1]

[1] Draper, [2] Draper Scholar, [3] Department of Biomedical Engineering, Tufts University

ABSTRACT

Traumatic brain injuries (TBIs) are widespread among warfighters and military personnel [1] and can lead to chronic dysfunction and long-term disability. Diagnosis and characterization of TBIs is highly challenging because observation of patients during the acute period after injury is often impossible, and TBIs can result in long-term symptoms even when short-term symptoms are not observed. In vitro 3D brain models for TBI have the potential to elucidate some of the cellular and molecular mechanisms underlying TBIs, but models generated to date lack integration with a blood-brain-barrier model and the throughput necessary for therapy development. Current diagnostics are not sufficiently predictive, and no treatments for TBI have progressed past phase II clinical trials. Here we propose integration of a novel brain model based on silk scaffolds into Draper's Predict96 organ-on-chip platform for investigation of diagnostic biomarkers and evaluation of potential therapeutics, such as exosome-based therapies.

Introduction

Traumatic brain injury (TBI) affects millions of individuals worldwide, but current diagnostics for TBI are relatively crude and single biomarker-based diagnostics have been poor predictors of outcomes [2]. Further, there are no effective therapeutics that can regenerate brain tissue or prevent the progression of secondary injury such as neuronal apoptosis. Human tissue models can help provide information about injury that is difficult to obtain from patients, but TBI is a highly complex and heterogeneous condition that current in vivo and in vitro models cannot recapitulate effectively to complement clinical data. A complex and physiologically relevant 3D brain model is needed to advance the field of TBI diagnostics and therapeutics.

We will develop a high-throughput brain injury model based on Draper's Predict96 high-throughput organ-on-chip platform [3] using 3D silk-based tissue scaffolds from the Kaplan Lab at Tufts University. This model can be used to discover panels of biomarkers for diagnostics, and to evaluate promising new exosome-based treatment modalities.

Draper's Predict96 Organ-On-Chip System

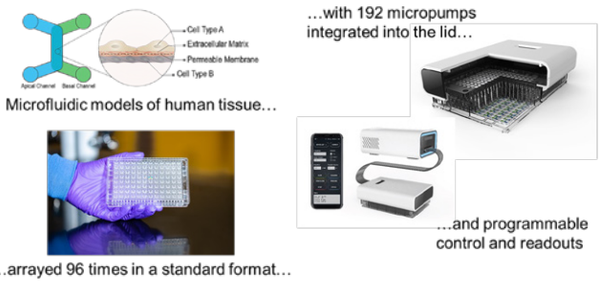

Proposed Approach (Long-Term)

Develop TBI Injury Model

1. Establish in vitro multi-cell culture 3D brain model in Draper's Predict96 platform using human cells
   - Neurons, astrocytes, microglia
2. Integrate 3D brain model with blood-brain-barrier (BBB) vasculature and fluid flow
   - Brain microvascular endothelial cells, pericytes
3. Establish TBI injury model
   - Controlled cortical impact or blast (simulated using focused ultrasound)

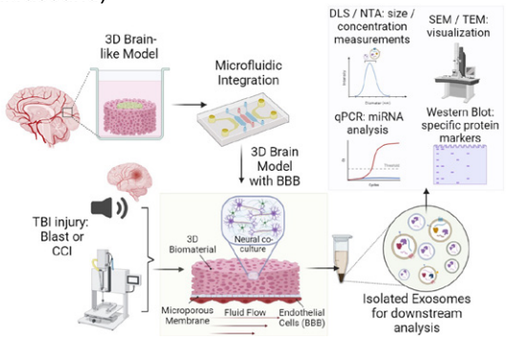

Investigate Exosomes as a Potential Diagnostic or Therapeutic

1. Isolate and characterize secreted exosomes
   - microRNA and protein biomarkers
2. Challenge the model using loaded exosomes as a therapeutic

Anticipated Results

A functional brain model will…

- Exhibit viable co-culture growth (>70%) of including neurons, astrocytes, microglia and show distinct axonal projections and dense neuronal networks
- Expect flow (perfusion) to result in higher-quality tissue
- Loss of viability and increase of inflammatory markers in response to injury

Discussion

Draper will first adapt and integrate an established 3D brain model from the Kaplan Lab at Tufts University into our platform to create a high-throughput testing platform to study complex brain and nervous system disorders. A biocompatible porous silk and collagen scaffold will be used as the support network required for the neurons and glial cells to grow in 3D. The unique scaffold provides mechanical integrity with high porosity to allow for neurons to anchor and extend their axons to make connections [4].

In the future, Draper may explore additional materials for scaffolds, including 3D organoid based approaches. In developing these models, it will be important to maintain the ability to screen conditions in high-throughput as the complexity of the model is increased.

References

[1] Swanson, et al. (2017). Traumatic Brain Injury Incidence, Clinical Overview, and Policies in the US Military Health System Since 2000. Public Health Rep, 132(2), 251-259.

[2] Ghaith, H. S., et al. (2022). A Literature Review of Traumatic Brain Injury Biomarkers. Mol Neurobiol, 59(7), 4141-4158.

[3] Azizgolshani, H., et al. (2021). High-throughput organ-on-chip platform with integrated programmable fluid flow and real-time sensing for complex tissue models in drug development workflows. Lab on a Chip, 21(8).

[4] Cairns, D. M., et al. (2020). A 3D human brain like tissue model of herpes induced Alzheimer's disease. Science Advances, 6(19).

On-the-fly Transfection for Printing Genetically Patterned Tissues

Aric Lu[1,2,3,4], Carlos Marquez[1,2], Paul Stankey[1,2], Jonathan Coppeta[3], and Jennifer Lewis[1,2]

[1]Harvard John Paulson School of Engineering and Applied Sciences, [2]Wyss Institute for Biologically Inspired Engineering, [3]Draper Laboratory, [4]Draper Scholar

ABSTRACT

Engineered tissues for therapeutic applications require multiple cell types organized into specific structures for organ function. Recent advances in genetic engineering approaches to stem cell differentiation promise unparalleled speed and efficiency for cell sourcing to meet these needs for cellular diversity and organization. To leverage these advances, we have developed on-the-fly transfection, a new 3D bioprinting technology that uses electroporation to selectively modify cells during the tissue fabrication process. We designed a functionalized printing nozzle to electroporate segments of a cell-laden ink. Then, we developed an agarose microparticle based ink compatible with both printing and electroporation. We demonstrate high cell viability and transfection efficiency of eGFP mRNA in HEK-293T cells and human induced pluripotent stem cells (hiPSCs). Finally, we use our hiPSC-laden ink to program patterns of eGFP expression within a printed tissue, demonstrating how on-the-fly transfection can recreate the cellular patterning found in native human organs.

Advantages of on-the-fly transfection:

- Engineering cellular diversity reduces the need to generate multiple cells types for tissue engineering
- Genetic approaches to cell differentiation are faster and more efficient than other methods
- Highly modular – can mix and match different genes and cell types to get desired cell types

Nozzle design:

Nozzle rendering

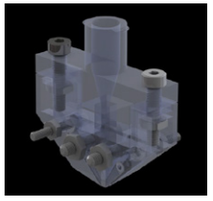

Printed part

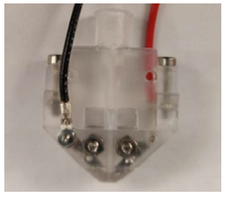

Electrode layout

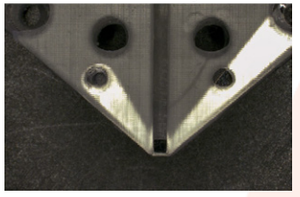

- Platinum electrodes to apply electric field across nozzle outlet
- 3D printed nozzle for customizable geometry
- Nozzle geometry affects resolution of both print and gene pattern

Ink characterization:

MP size distribution

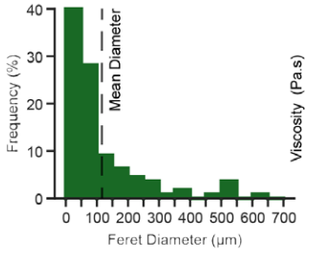

Shear-thinning behavior

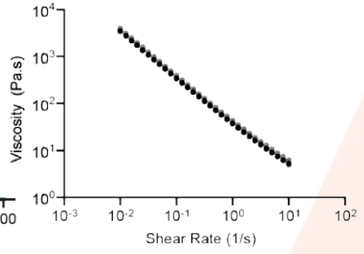

Yield-stress behavior

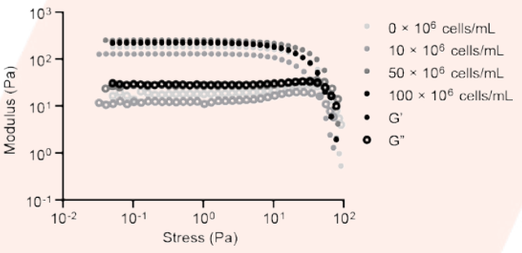

- Ink is composed of cells mixed with microparticles with mean diameter 116 μm
- Agarose microparticle inks have proper shear-thinning and yield stress behavior across range of cell concentrations
- Agarose does not bind nucleic acids and maintains their availability for transfection

Viability and transfection efficiency:

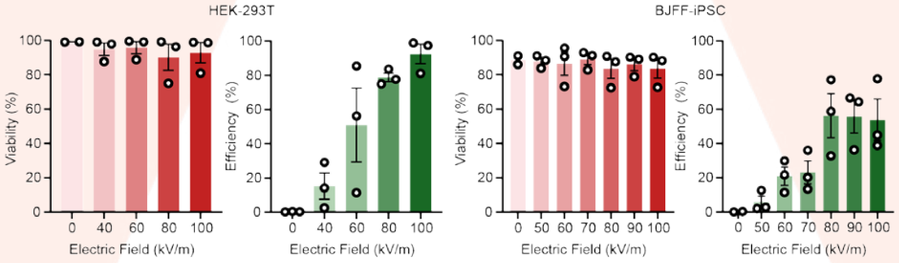

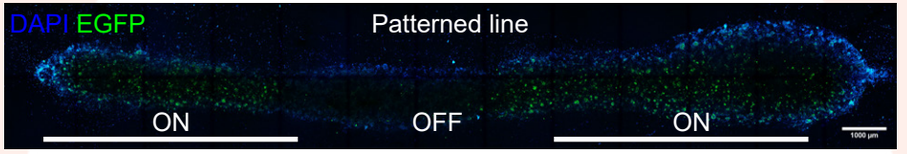

Tissue design

Printed pattern

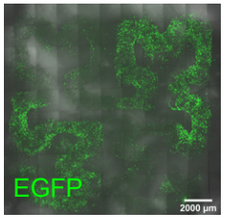

- High viability and transfection efficiency across multiple cell types using mRNA as a delivery vehicle
- Patterns can be printed in hiPSC-derived tissues using eGFP mRNA as a reporter gene
- Demonstrates tech feasibility

Next steps:

- Optimize and evaluate pattern resolution and its relationship to nozzle geometry
- Test other mRNAs for controlling cell phenotype in hiPSCs
- Demonstrate transfection of other cell types, such as iPSC-derived cardiomyocytes

Lidar Retrieval of Snowpack Properties

Connor Henley[1,2,*], Joseph Hollmann[2], Colin Meyer[3], and Ramesh Raskar[1]

[1]MIT Media Lab, [2]The Charles Stark Draper Laboratory, Inc., [3]Dartmouth College
*co24401@mit.edu, Connor Henley is a Draper Scholar

ABSTRACT

When a snowpack is illuminated by a laser pulse, most photons in the pulse scatter many times beneath the snowpack surface before returning to the receiver. We show that the additional time delay caused by this volumetric scattering can be exploited to estimate important snowpack properties—namely, ice grain radius, snowpack density, and concentration of light absorbing impurities. We develop a method for estimating these quantities from photon time-of-flight histograms, and successfully demonstrate our method on snow samples with varied properties.

1. Introduction

- Lidar is widely used to map **snowpack surface geometry** (i.e. depth, area)
- Most photons in laser pulse scatter many times within **snowpack volume** before returning to receiver
- We use the signature of **volumetric scattering** to estimate following snowpack properties:
  - **Mass density**: Required to compute amount of water stored in snowpack
  - **Ice grain radius**: Controls snowpack albedo and melt-rate
  - **Light absorbing impurities:** Concentration of soot, dust, or organic carbon.

- **Applications:** Water resource monitoring, snow-melt forecasting, glacier mass balance, avalanche prediction

2. Experiment

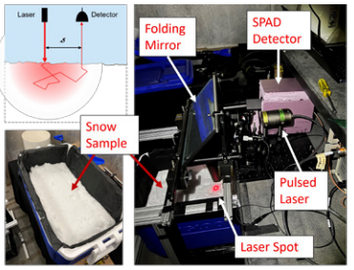

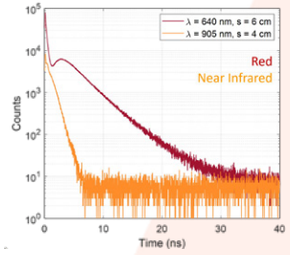

3. Photon Diffusion Model

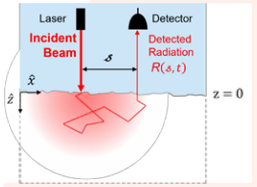

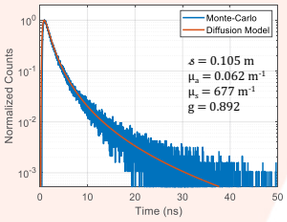

Photon Diffusion Model [1]

$$R(s,t) = \alpha \frac{{z_0}^2}{(2Dc_*t)^{5/2}} \exp\left(-\mu_a c_* t - \frac{s^2 + {z_0}^2}{4Dc_*t}\right)\left[1 + \frac{7}{3}\exp\left(-\frac{10{z_0}^2}{9Dc_*t}\right)\right]$$

Mie Scattering Model [2, et al.]

$$\mu_s = \frac{3Q_s}{4}\frac{v_*}{r_*} \quad , \quad \mu_a = \left(\frac{3Q_a}{4r_*} + \rho_{ice}\beta_{bc}C_{bc}\right)\times v_* \quad , \quad c_* = \frac{c}{1 + (n_{ice} - 1)v_*}$$

Scattering Parameters

μ_a = absorption coefficient (m^{-1})
μ_s = scattering coefficient (m^{-1})
g = scattering asymmetry factor (unitless)
c_* = mean speed of light (m/s)

Snowpack Parameters

v_* = ice volume fraction (unitless)
r_* = grain radius (m)
C_{bc} = black carbon concentration (g b.c. / g snow)

4. Estimation Algorithm

Model fit → **Parameter Lookup**

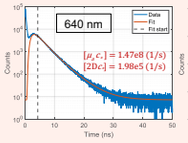

Fit model to time-of-flight histograms at two wavelengths

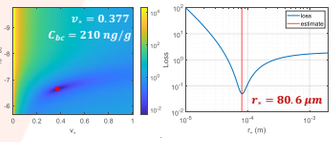

Lookup Table for Volume Fraction, Grain Radius, and Impurity Concentration

5. Results

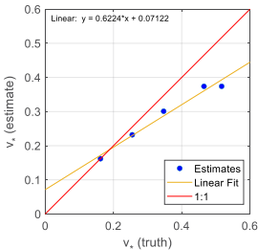

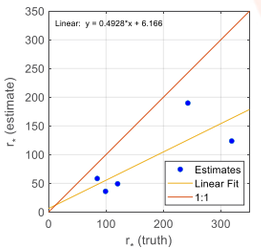

Ground truth sources:

- (v_*) Melt test
- (r_*) Micro-CT
- (C_{bc}) Soot Photometer (still to-do)

- Measured five snow samples with varied properties
- Ice volume fraction estimates linearly dependent on true values
- Positive correlation between true and estimated grain size estimates
- Validation of black carbon estimates is forthcoming

6. Conclusions

- Time-domain diffuse optical measurements enable retrieval of grain size, ice volume fraction, and impurity content
- Experimental results are consistent with ground truth
- Future work: Extend to remote sensing platform and design device for user-friendly *in situ* measurements

7. References

[1] Kienle, A. and Patterson, M.S. (1997), Improved solutions of the steady-state and time-resolved diffusion equations for reflectance from a semi-infinite turbid medium. J. Opt. Soc. Am. A, 14, 246-254.

[2] Smith, B.E. et al. (2018). Modeling biases in laser-altimetry measurements caused by scattering of green light in snow. Remote Sensing of Environment, 215, 398-410.

This material is based on work supported by the Office of Naval Research under Contract No. N00014-21-C-1040. Any opinions, findings, and conclusions or recommendations expressed in this material are those of the authors and do not necessarily reflect the views of the Office of Naval Research.

Reducing Hypersonic Window Heating via Cavity Flow

Matthew Schofield[1], Arthur Huang[2], and Wesley Harris[3]

[1]Massachusetts Institute of Technology and Draper Scholar, [2]The Charles Stark Draper Laboratory Inc, [3]Massachusetts Institute of Technology

ABSTRACT

Extreme surface temperatures on hypersonic vehicles induce significant heating rates into glass windows located on the surface. Recessing the window into the surface produces a cavity geometry that reduces this heating. Contrasting this reduction with the aero-optical distortions induced by the complex flow these geometries create, I will find a length-to-depth ratio that reduces the heating rate while producing minimal aero-optical distortions.

INTRODUCTION

- Window bending caused by high surface heating on hypersonic vehicles can be reduced by placing the window at the bottom of a cavity.

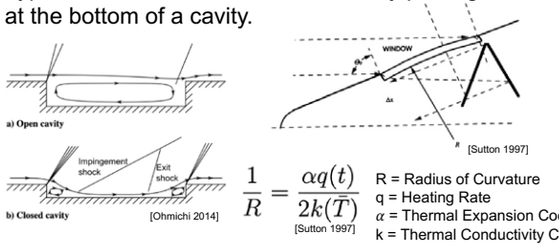

$$\frac{1}{R} = \frac{\alpha q(t)}{2k(\bar{T})}$$ [Sutton 1997]

R = Radius of Curvature
q = Heating Rate
α = Thermal Expansion Coeff.
k = Thermal Conductivity Coeff.

- The complex flow behavior found with a cavity geometry, while reducing window-induced distortions, may produce significant aero-optical distortions.

METHODS

- A flat place case, with no cavity recession, will be used as the control. With this, distortions attributed to varying length-to-depth ratios will be analyzed and compared.
- All simulations will be run with an unstructured, implicit, finite volume solver.
- Solver will be equipped with conjugate heat transfer to fully understand the effect of window heating.

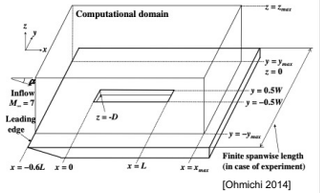

ANTICIPATED RESULTS

- Plots depicting heating rate at different points in the cavity for different length-to-depth ratios, similar to the plots depicted, will be presented, along with a table providing aero-optical distortions, like that below.
- The plots will clearly illustrate the effect of cavity geometry on these two types of distortions.
- Additionally, a distinction will be made between open cavities and closed cavities in order to emphasize the clear distinction of flow behavior.

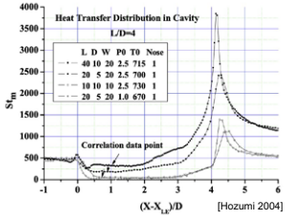

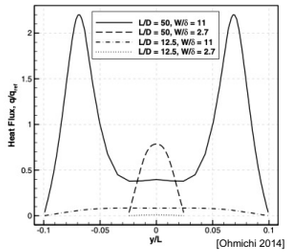

L/D:	4	6	8	10	14	16	18	20
y = 0	0.21	0.18	0.14	0.13	0.06	0.04	0.02	0.009
y = 0.2W	0.24	0.21	0.19	0.14	0.07	0.04	0.02	0.011

NOTIONAL

Optical Path Difference for Varying L/D ratios at centerline and off-centerline

ANTICIPATED DISCUSSION

- Hypothesis: aero-optical distortions created by open-cavity flow overshadow the large heating rate reduction; therefore, the optimal length-to-depth ratio will be found in the closed-cavity regime.
- Open cavity reduces the heating rate, but has significant aero-optical distortions.
- Closed cavity has minimal aero-optical distortions, but a less severe reduction in heating rate.
- An optimal length-to-depth ratio in the closed-cavity regime limits both types of distortion.
- Research provides insight into the best length-to-depth ratio to use for hypersonic vehicle window design.

CONCLUSIONS

- This research aims to quantify the effects of cavity flow on window bending and aero-optical distortion. It will produce a length-to-depth ratio that optimizes this tradeoff.

ACKNOWLEDGMENTS OR REFS

- [1]: Ohmichi, Y., & Suzuki, K. (2014). Flow structures and heating augmentation around finite-width cavity in hypersonic flow. AIAA Journal, 52(8), 1624–1631. https://doi.org/10.2514/1.j052647
- [2]: Sutton, G. W. (1997). SPIE Proceedings. https://doi.org/10.1117/12.294472
- [3]: Hozumi, K., Koyama, T., & Hirabayashi, N. (2004). Experimental Study on Hypersonic Heating Characteristics of Cavity Wake Flow. 24th International Congress of the Aeronautical Sciences.
- This work is funded through the Draper Scholars Program.

Insights into the Role of Endothelial Dysfunction in Severe COVID-19

Michelle Nguyen[1-2,5], Scott Seitz[4-5], Corin Williams[3], Ashley Gard[3], and John Connor[1,4-5]

[1]Department of Pharmacology and Experimental Therapeutics, Boston University School of Medicine, Boston, MA, [2]Draper Scholar Program, Cambridge, MA, [3]The Charles Stark Draper Laboratory Inc., Cambridge, MA, [4]Department of Microbiology, Boston University School of Medicine, Boston, MA, USA [5]National Emerging Infectious Diseases Laboratories, Boston University, Boston, MA

ABSTRACT

Endothelial dysfunction and blood clotting pathologies are striking features of severe COVID-19. Despite the frequency of severe COVID-19, it remains unclear whether endothelial cells of human blood vessel express the entry receptor for SARS-CoV-2 infection. We use various tissue culture approaches to investigate how SARS-CoV-2 directly breaches the endothelium or indirectly mediates endothelial dysfunction. To accomplish this goal, we study viral entry in diverse endothelial cell types using vesicular stomatitis virus and SARS-CoV-2. Under flow-derived mechanical cues, we find endothelial cultures respond to virus with loss of cell monolayer but without direct infection. These findings show a phenotype that may be relevant to studying COVID-19 associated blood vessel complications.

INTRODUCTION

- Endothelial dysfunction (endotheliopathy) and propensity for fatal blood clots (coagulopathy) have been observed since the first cases of severe COVID-19.

Figure 1. How SARS-CoV-2 Infection leads to Severe COVID-19

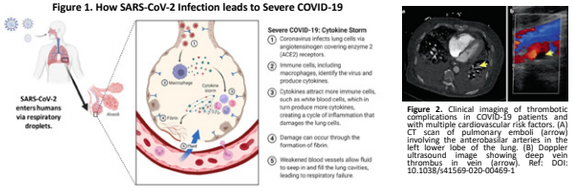

Figure 2. Clinical imaging of thrombotic complications in COVID-19 patients and with multiple cardiovascular risk factors. (A) CT scan of pulmonary emboli (arrow) involving the anterobasilar arteries in the left lower lobe of the lung. (B) Doppler ultrasound image showing deep vein thrombus in vein (arrow). Ref: DOI: 10.1038/s41569-020-00469-1

- These features are more common in COVID-19 than other respiratory illnesses.
- Endothelial cells of this tissue have little to no expression of the ACE2 receptor required in SARS-CoV-2 infection. It is unclear how these cells are affected in severe COVID-19.
- This gap is due to the lack of predictive models to study human SARS-CoV-2 pathogenesis and endotheliopathy.
- Animal models are not representative of human physiology and patient biopsies capture terminal stages of disease.
- Applying microphysiological systems (MPS) to address these limitations supports robust investigations into earlier stages of diseases which can be targeted in therapeutic strategies to prevent this pathology.

SPECIFIC AIMS

Goal: Understand how SARS-CoV-2 infection leads to endotheliopathy and coagulopathy.
Hypothesis: SARS-CoV-2 induces host immune responses that ultimately lead to endothelial dysfunction irrespective of direct endothelial cell infection.

- **Aim 1:** To determine a direct mechanism of how SARS-CoV-2 endothelial dysfunction occurs.
- **Aim 2:** To investigate the contribution of host antiviral immune factors in COVID-19-related endotheliopathy.

METHODS

***In Vitro* Screening of Endothelial Cell Tropism**

Do endothelial cells possess the host entry receptor for direct infection?

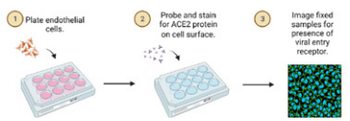

Can SARS-CoV-2 infect cells irrespective of the host entry receptor, ACE2?

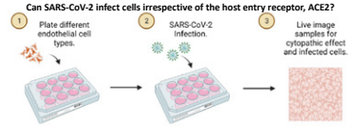

Screening for Viral Infection under Physiological Conditions in PREDICT96

Can SARS-CoV-2 enter endothelial cells under shear stress?

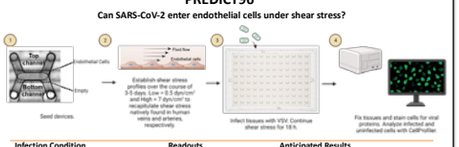

Infection Condition	Readouts	Anticipated Results
Mock	• Viral Protein (Matrix/VSV-M) • DAPI counter stain to visualize cells	Remains healthy under shear stress
Wildtype Vesicular Stomatitis Virus (WT VSV)		Cells are permissive to infection, loss of cells, direct infection
Pseudotyped SARS-CoV-2 (VSV backbone with CoV-2-Spike glycoprotein)		Cells are permissive to infection, loss of cells, direct infection
Pseudotyped Lassa (VSV backbone Lassa glycoprotein)		Cells are permissive to infection, loss of cells, direct infection

RESULTS

Endothelial Cells Lack ACE2 Expression

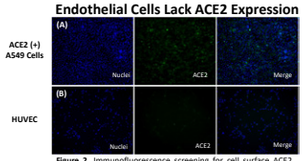

Figure 2. Immunofluorescence screening for cell surface ACE2 receptor. **(A)** A549 cells overpressing ACE2 (green), positive control for the entry receptor for SARS-CoV-2 infection. **(B)** Human umbilical endothelial vein cells do not express ACE2 (shown in green). Counter stain of non-ACE2 cells shown in blue.

PREDICT96 as an *In Vitro* Disease Model of Infection

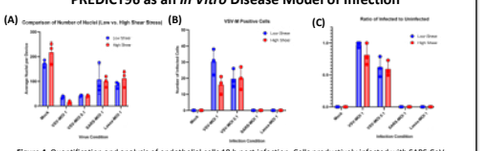

Figure 4. Quantification and analysis of endothelial cells 18 h post infection. Cells productively infected with SARS-CoV-2 express VSV-M. Cells not infected lack VSV-M. **(A)** With respect to Mock, infected conditions show reduction in number of nuclei after 18 h exposure to circulating virus. **(B)** Reduction in number of nuclei does not directly correspond to number of infected cells, and **(C)** Reduction in number of nuclei does not directly correspond higher ratios of infected to uninfected cells.

Endothelial Cells are Resistant to SARS-CoV-2 Infection in 2D Cell Culture

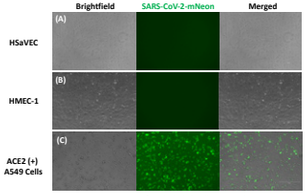

Figure 3. Live imaging of endothelial cells exposed to SARS-CoV-2 tagged with mNeon reporter gene. Cells productively infected with SARS-CoV-2 express mNeon. Cells not infected do not express reporter gene. **(A)** Human saphenous vein cells, **(B)** Immortalized human microvascular endothelial cells derived from dermis, and **(C)** A549 cells overpressing ACE2 as positive control.

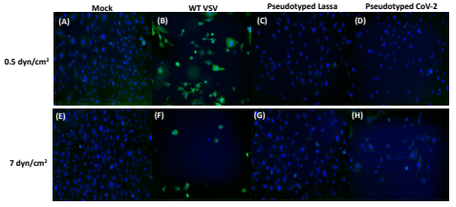

Figure 5. Immunofluorescence screening for presence of viral protein in vascular PREDICT96 tissues. Tissues were infected with multiplicity of infection (MOI) of 1. Upper panel represents tissue exposed to low shear (0.5 dyn/cm²). Lower panel represents tissues exposed to high shear (7 dyn/cm²). Nuclei of cells stained with DAPI. Viral protein, VSV-M stained in green. **(A&E)** uninfected tissues, **(B&F)** WT VSV infected tissues as positive control, **(C&G)** Pseudotyped Lassa infected cells, and **(D&H)** Pseudotyped SARS-CoV-2 infected cells.

DISCUSSION

- *In vitro* screening for endothelial cell tropism shows that endothelial cells do not express the ACE2 receptor and are not susceptible to SARS-CoV-2 infection.
- There was no presence of viral protein in pseudotyped SARS-CoV-2 infected tissues which correlated with previous findings in 2D tissue culture using authentic virus.
- Overall, there was a loss of cells in infected tissues with respect to uninfected tissues.
- Reduction in nuclei count suggests that there was damage to endothelial monolayers as result of exposure to circulating virus or tissue secreted factors during infection.
- These patterns occurred irrespective of the shear stress profile (low or high shear) but were unique to type of virus infection condition.
- We attribute lack of infection in certain tissues to potential cell polarization under shear stress conditions.

CONCLUSIONS & FUTURE DIRECTIONS

- A mechanism of direct SARS-CoV-2 infection of endothelial cells remains unknown.
- Shear stress is a required to observe endothelial damage in response to different types of infections.
- Endothelial damage occurs without direct infection under physiological conditions within 18 h in PREDICT96. Further staining for other endothelial injury markers would support validation of findings.
- Future work would explore if it is possible to observe infection in PREDICT96 with presence of other viral proteins found in authentic SARS-CoV-2.

ACKNOWLEDGMENTS

- This research was supported by the Office of Special Programs, Education Office, and IRAD (HIPPI). I would also like to acknowledge Dr. John Connor, Ms. Ashley Gard, and Dr. Corin Williams for their mentorship.

BOSTON UNIVERSITY NEIDL National Emerging Infectious Diseases Laboratories DRAPER

Design Exploration of a MEMS Stirling Engine

Ryann Hee[1,2]

[1]Massachusetts Institute of Technology, [2]Draper Scholar

ABSTRACT

As technologies continue to advance there is a desire to make energy sources as small as possible and as powerful as possible. Space probes and other high reliability systems have a need for power in remote, harsh environments that require novel materials development to meet growing power and thermal management requirements while still maintaining small form factors. Today there are no micro power systems that have efficiencies greater than ~2% which meet all mechanical, thermal, and system requirements for space probes and other small form factor power needs [1]. However, Stirling engines are a promising heat engine technology and are known to achieve high efficiency (30-40%) [2]. If this efficiency can be maintained in a small form factor, miniaturized Stirling engines would be a widely desired technology. This study seeks to explore the design space of a 2W miniaturized Stirling engine for applications in small-scale (mm), high efficiency power generation. Previous work has laid out a solid thermodynamic foundation for miniaturized Stirling engines and shown major gaps in the technology, one of those being the overwhelming parasitic losses that occur at such a small scale [3]. Our design aims to mitigate these losses and find an optimal efficiency through modeling done in Simulink. Early models have displayed a 7.1% mechanical efficiency at 2W. We predict that as we continue to optimize each of the parameters in our model and focus on parasitic losses, we will be able to achieve a much greater efficiency compared to what is currently available.

INTRODUCTION

- Stirling engines operate by compressing and expanding a 'working fluid' to generate heat energy which can be converted into mechanical energy.
- Stirling engines have some of the highest efficiencies compared to competing technologies.
- Miniaturized Stirling engines were first studied in 1989 and a fundamental thermodynamic framework was built up from there.
- In 2018 a research group produced and tested a prototype at the mm scale. The prototype did not work as predicted and this was likely due to unaccounted parasitic losses[3]. Key components here are the heat source, working fluid (gas), free piston design, and regenerators

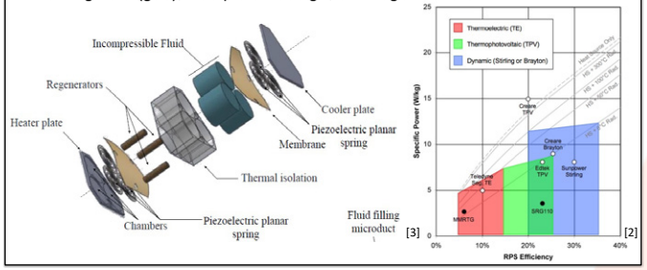

METHODS

Our design considered key findings in past work and prioritized mitigating parasitic losses.

- Firstly, Stirling engines gain efficiency based on the temperature differential, as you scale down it becomes exponentially harder to maintain a large temperature difference between hot and cold sides. This means that we want to create as much distance between the hot and cold side as possible → maximize piston length
- Second, we need to manage our parasitic losses one of the largest being conductive heat loss. A free piston design allows for a completely closed system (easier to contain heat), no mechanical linkage (reduces complexity and increases lifetime), and high thermal efficiency.
- Regenerators are also key component as they store excess heat that might normally be lost and maximize heat transfer between the pistons.

MODEL

Double acting Stirling with balanced pistons:

- At such a small-scale deviations in the piston motion could eventually lead to reduced efficiency or in some cases a non-operational system. The design need here is to make sure we have balanced piston motion.
- We have also included regenerators in the system to help maximize heat transfer.

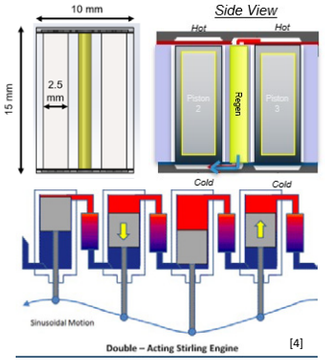

We were able to model this design using Simulink to start observing the engine performance and pull an estimated mechanical efficiency from the model. The idea is that each pair of pistons will create a sinusoidal motion to offset the other. However, our model first ran into stability issues resulting from the four pistons deviating. We corrected this issue by adding a hard stop to the ends of this pistons.

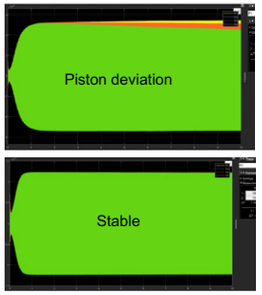

Model inputs:
- Material properties and dimensions (traditional MEMS materials)
- Temperature gradient

Model outputs:
- Piston motion
- Efficiency (mechanical efficiency)
- Total heat flow
- Heat flow through the housing

Key parameters:
- Damping
- Housing area
- Spring constant
- Piston mass
- Gas pressure
- Gas type
- Regenerator size

RESULTS

Glass was chosen as the housing around the pistons because of its low thermoconductivity. Early runs of our model showed we were losing a significant portion of heat through the housing, which made this a priority parameter to optimize for. Since we can relate heat through the housing:

$$Q \propto \frac{(A \cdot Th)}{L}.$$

By reducing the overall housing area it increased our overall mechanical efficiency from 4% to 7%!

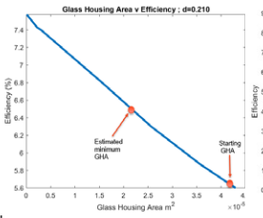

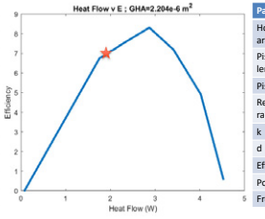

Parameter	Value	Units
Housing area	2.204	mm^2
Piston length	14	mm
Piston side	2.5	mm
Regen radius	0.65	mm
k	100	
d	0.0213	
Efficiency	~7.1%	
Power	2.00	W
Frequency	~ 100	Hz

CONCLUSIONS

We will continue to explore the model with the goal of establishing a viable design space for a MEMS Stirling engine given a 2W threshold. Our exploration will also explore the space for non-traditional materials in search of the highest attainable efficiency for this design.

ACKNOWLEDGMENTS

I would like to thank my advisors Kasia Oleske and Jeffrey Hoffman for their support in this project. I would also like to thank the IRaD group at Draper with special mention to Brian Munroe, Jim Dombrowski, Joe Aghia, Rob McNabb, and Jim Bickford.

[1] Wilson, et al. "Radioisotope Heater Unit-Based Stirling Power Converter Development at NASA Glenn Research Center," NASA/TM (2018).

[2] Lee S. Mason, "Realistic Specific Power Expectations for Advanced Radioisotope Power Systems," NASA, (2006).

[3] Begot, et al. "A novel model and design of a MEMS Stirling engine," International Journal of Heat and Technology, (2018).

[4] Velumani, Siriam. "Double - Acting Stirling Engine - Renewable Energy - Stirling Engine." *Renewable Energy - Stirling Engine*, 2016, https://sites.google.com/a/emich.edu/cae54681615/history/types/double---acting-stirling-engine. (2016)

Massachusetts Institute of Technology

DRAPER

Oxygen sensing in a high-throughput organ-on-chip platform for assessment of drug-induced nephrotoxicity

Samuel H. Kann[1,2], Erin M. Shaughnessey[1,3], Xin Zhang[2], Joseph L. Charest[4], Else M. Vedula[4]

[1]Draper Scholar, [2]Boston University, [3]Tufts University, 4Draper

ABSTRACT

Pre-clinical assessment of drug-induced kidney injury remains a challenge due to the failure of animal models and simple 2D cell culture to recapitulate the function of the human kidney. Additionally, standard toxicological assays often rely on invasive or endpoint readouts that fail to capture kinetic tissue responses during drug exposures. Kidney-on-chip systems culture human tissue with improved physiological function and allow integration of sensors for non-invasive and near real-time monitoring of tissue health. Here, we investigate the use of optical-based oxygen sensing in an array of kidney-on-chips for monitoring the onset and progression of drug-induced kidney injury during clinically relevant drug exposures.

INTRODUCTION

Organ-on-chip and integrated sensing for studying drug toxicity

Pre-clinical assessment of drug-induced nephrotoxicity, injury to the kidney due to drug exposure, remains a challenge. Organ-on-chips improve toxicological assessments due to the capability to support human cell culture in a semi - complex microenvironment and accommodate sensors for rapid, label-free, and on-chip readouts.

PREDICT96: High-throughput organ-on-chip platform with integrated oxygen sensing

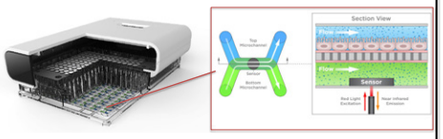

Objective: We investigated a technique for measurement of oxygen consumption in PREDICT96 for assessment of drug-induced nephrotoxicity in a microfluidic human primary co-culture model of the kidney PT (mcPT).

Methods

Experimental design and workflow for oxygen sensing & assessment of drug-induced nephrotoxicity

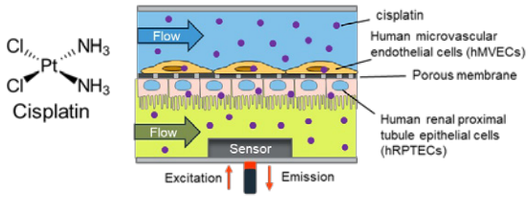

- An optical-based oxygen sensor was bonded to the floor of each bottom microchannel. Human primary renal proximal tubule epithelial cells (hRPTECs) and human primary microvascular endothelial cells (hMVECs) were co-cultured on the central membrane and exposed to flow on both sides.
- We measured steady state oxygen levels during continuous perfusion and delivery of cisplatin, a nephrotoxic compound for a clinically relevant exposure duration of 5 days.

Results

Monitoring steady-state oxygen levels enables detection of hRPTEC oxygen consumption

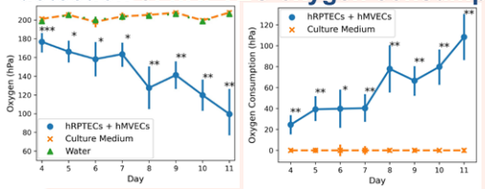

- Oxygen and oxygen consumption measurements on days 4-11 in devices containing hRPTECs +hMVECs (n=5) were significantly different than devices containing water (n=16) and culture medium (n=4) (*p < 0.05, **p < 0.01, ***p < 0.001 compared to culture medium controls, Kruskal-Wallis and Dunn's post-hoc test).

Oxygen consumption correlated with hRPTEC nuclei density following 5 days of cisplatin exposure

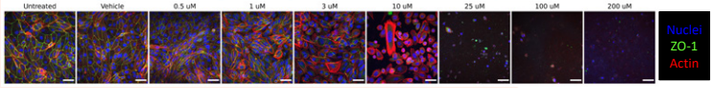

- Representative images of hRPTECs stained with nuclei, actin, and ZO-1 indicated a dose-dependent injury response following 5 days of drug exposure

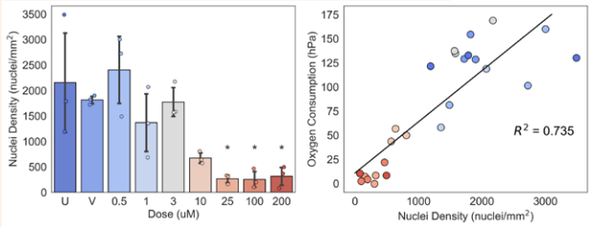

- Dose-dependent decrease in nuclei density (* p < 0.05 relative to untreated group, Kruskal-Wallis and Dunn's post hoc test)
- Oxygen consumption on day 5 of the cisplatin exposure correlated with hRPTEC nuclei density with an R^2 value of 0.735 (p < 0.001)

Oxygen sensor-enabled monitoring of cisplatin-induced injury to hRPTECs over 5 days

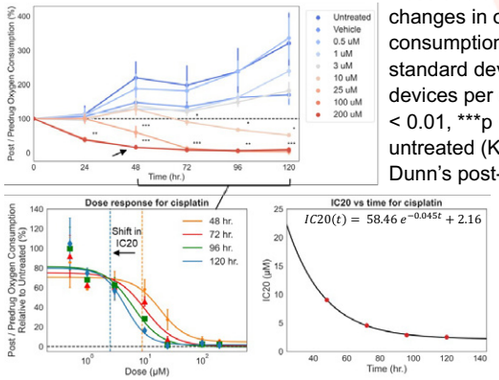

- Dose and time-dependent changes in oxygen consumption. Data are mean ± standard deviation of n=4-6 devices per dose. *p < 0.05, **p < 0.01, ***p < 0.001 relative to untreated (Kruskal-Wallis and Dunn's post-hoc test).
- Dose-dependent reduction in post/predrug oxygen consumption (markers) with fitted hill equations (solid lines) for estimation of the IC20at different timepoints.
- The IC20 (red circles) for cisplatin decreased exponentially over time from 19.8 to 2.2 μM over 5 days (R^2=100)

CONCLUSIONS

Our results demonstrated the utility of monitoring steady state oxygen levels in a high-throughput organ-on-chip platform for non-invasive and rapid assessment of oxygen consumption and nephrotoxicity in a human co-culture PT model. The presented technique will provide a valuable tool in drug development for evaluating injury in microfluidic kidney models for toxicological screening and investigation of potential therapies.

ACKNOWLEDGMENTS

This work is supported by the Draper Scholar Program. This material is based upon work supported by the National Science Foundation under Grant No. 1804845 and 1804787. Any opinions, findings and conclusions or recommendations expressed in this material are those of the author(s) and do not necessarily reflect the views of the National Science Foundation.

Surrogate Neural Networks for Efficient Simulation-based Trajectory Planning Optimization

[1]Evelyn Ruff, [2]Piero Miotto, [2]Matthew Stoeckle, [2]Rebecca Russell & [3]Jonathan P. How

[1]Draper Scholar, The Charles Stark Draper Laboratory; Inc., [2]The Charles Stark Draper Laboratory, Inc.; [3]The Massachusetts Institute of Technology

ABSTRACT

This paper presents a novel methodology that uses surrogate models in the form of neural networks to reduce the computation time of the simulation-based optimization of a reference trajectory. The reference trajectory planning simulation is highly nonlinear and computationally expensive, making it challenging to optimize iteratively. In contrast to the large datasets used to create the surrogate models in the prior literature, our methodology minimizes the number of simulation executions. This is proven to be more efficient than hand-tuning the inputs through trial-and-error or randomly sampling the input parameter space. Our approach yields better simulation outcomes achieved more rapidly. We found a significantly better performing reference trajectory compared to nominal, and the numerical results clearly demonstrate a substantial reduction in computation time for designing future trajectory planning configurations.

INTRODUCTION

- Simulation-based optimization (SO) is necessary when there is no analytical model accessible. Instead, SO is used to find the input values that lead to the desired outcome.
- The Approach and Landing trajectory planning simulation for the hypersonic vehicle is highly nonlinear and expensive to run, making it very difficult to optimize.
- Surrogate models are used to imitate simulations, especially if the simulation is computationally expensive.
- This methodology uses data from the simulation to train a neural network as a surrogate model of the simulation. We then use the predictions of the surrogate model to optimize the simulation input parameters to achieve an optimal reference trajectory for landing the hypersonic vehicle.

METHODOLOGY

1) Query an initial dataset from a quasirandom sampling
2) Train a neural network model $f^{nn}(x)$ to approximate $f(x)$
3) Initialize set of quasi-randomly distributed input parameters x across initial dataset
4) Use stochastic gradient descent with $f^{nn}(x)$ to find the x that minimizes the objective function $g(x)$
5)Choose input x that produces minimum loss according to objective function
6)Query $y = f^{true}(x)$ for these selected x and add them to the training dataset
7) Repeat from Step 2 until the stopping criterion is reached

RESULTS

The input-output data was used to train a neural network to imitate the trajectory planning simulation. The gradients of the surrogate neural network were then successfully used to optimize the inputs to achieve the desired output. Shown below is a two-dimensional representation of the input parameter space and the from the objective function predicted by the surrogate model. The algorithm then iteratively queries the trajectory planning simulation to improve the surrogate model's fidelity in promising areas of the input parameter space. Through these intelligent queries, this methodology finds the optimal values for the input parameters that lead to the desired landing of the hypersonic vehicle. The new reference trajectory is much better than the existing one, as shown in the table below, and it was also found in only 10 simulation queries. Hence, this algorithm is significantly faster than the current practice of hand-tuning or random search.

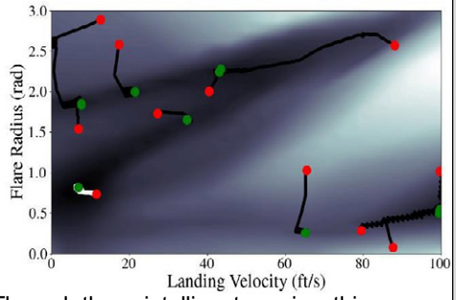

	Performance Results of Trajectories			
	Sink Rate (ft/s)	Horizontal Velocity (knots)	Downrange Position (ft)	Loss
Target	2.00	18.0	400.0	0.00
Nominal	1.48	23.3	193.2	0.24
New	2.00	17.9	378.4	0.11

DISCUSSION

- This methodology efficiently optimizes the large input parameter space to the trajectory planning simulation. It is proven to be consistently faster than random search
- Existing algorithms that also use the gradients of a surrogate neural network for optimization rely on collecting far more training data, meaning they are less efficient.
- Every existing trajectory optimization algorithm requires an analytical model of the dynamics, which is not available for this application.

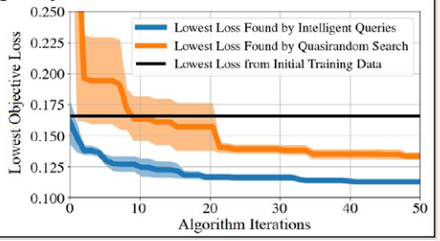

CONTRIBUTIONS

- Novel algorithm using neural network gradients to intelligently select simulation input values for simulation-based optimization
- Computationally efficient methodology for optimizing general black-box simulations with desired outputs
- New optimal trajectory planning tool for hypersonic vehicles

ACKNOWLEDGMENTS

Endless thanks to Piero Miotto, Matthew Stoeckle, Rebecca Russell, and Jonathan P. How for your guidance and support.

Data-Stream Clustering for Event-Based Camera Navigation

Yehia Helwa (Draper Scholar)[1,2], Lou Kratchman [2], and Robert Bishop [1]

[1]University of South Florida, [2] The Charles Stark Draper Laboratory, Inc.

ABSTRACT

Event cameras are bio-inspired vision sensors that have higher dynamic range and lower latency than standard cameras while requiring novel algorithms to process their unique output. This thesis adapts data stream clustering algorithms for feature identification and tracking of event data streams and analyzes their viability for visual-inertial odometry (VIO).

INTRODUCTION

- UAV VIO currently depends on conventional frame cameras that will suffer from motion blur at higher speeds degrading navigation performance
- Event cameras are imaging sensors that possess:
  - High update rate, no motion blur
  - Unconventional output, cannot use traditional computer vision algorithms
- The unconventional output of the event camera is due to its independent asynchronous pixels that trigger when a brightness change occurs, creating an ”event”

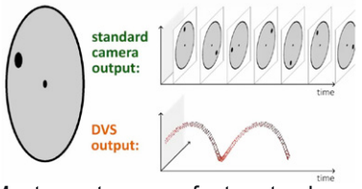

Event Time	X	Y
0.000000000	43	140
0.000082999	43	141
0.000149999	43	139
0.000157000	40	141
0.000161999	44	141
0.000174000	44	144

- Most event camera feature trackers convert events to frames and use traditional feature tracking approaches, ignoring rather than leveraging the properties of events
- The asynchronous nature of event streams means that features will generate a continuous flow of events in pixel-time space, tracking these “flows” would perform feature identification and matching simultaneously
- Leveraging existing data-stream clustering work done with DenStream, EventDenStream aims to create feature tracks for VIO by clustering event streams in real time.

PSEUDOCODE

Algorithm 1 EventDenStream (event stream, decaying factor λ, core weight threshold μ, tolerance factor β, neighborhod threshold ϵ, cluster lifetime threshold ξ)

```
for each event that arrives do
    Find nearest p-micro cluster and temporarily merge event
    if new radius of p-micro cluster ≤ε then
        Completely merge event into p-micro cluster
    else
        Remove event from p-micro cluster
        Find nearest o-micro cluster and temporarily merge event
        if new radius of o-micro cluster ≤ε then
            Completely merge event into o-micro cluster
            if new weight of o-micro cluster ≥βμ then
                Upgrade o-micro cluster into p-micro cluster
            end if
        else
            Initialize new outlier cluster with event
        end if
    end if
    Decay each cluster weight using lambda
    for each p-micro and o-micro cluster do
        if cluster weight ≤ξ then
            Delete cluster
```

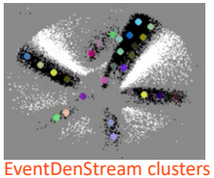

EventDenStream clusters extracted from event stream of a ceiling fan

Clustering performance experiment setup with motion capture cameras, event camera mounted on quadcopter and sample feature object (Rubik’s cube).

METHODS

UNDERWAY

- **Experiment 1 – Clustering Performance**
  1. Use motion capture to track UAV mounted event camera and feature object throughout movement
  2. Get clustering results from EventDenStream
  3. Use camera parameters to project objects onto image plane
  4. Calculate error between tracked cluster locations and “true” projected position on image plane
  5. Repeat and compare with other event camera feature tracking approaches

UNDERWAY

- **Experiment 2 – Maximum Event Rate**
  1. Record datasets of scenes with multiple object/textures that create various event rates
  2. Calculate error between time required to record datasets and process on RB5 flight computer
  3. Repeat and compare with other event camera feature tracking approaches

EXPECTED RESULTS

- Reprojection error is average RMSE between the cluster pixel location and the “true” projected pixel location
- Collect and plot reprojection errors between EvenDenstream and other event-based feature trackers (eCDT, HASTE, ACE, etc.) with experimental and publicly available datasets
- Good reprojection error is important for VIO navigation performance as it indicates how accurately tracked features correspond to physical features

Increasing Enterprise Performance
A Case Study in System Dynamics Modeling

Julia Koron[1,3] ; Chad Gibson[2] ; Hung Phan[3], Ph.D

[1]Draper Scholar; [2]The Charles Stark Draper Laboratory, 555 Technology Square, Cambridge, MA, 02139; [3]Department of Mathematics and Statistics, University of Massachusetts Lowell, Lowell, MA, 01852

ABSTRACT

The Engineering Operations Team manages the hiring and staffing of engineers at Draper. This process relies on the underlying demand for engineering work. Forecasting the amount of work to do, drives the number of engineers Draper needs. The relationship between engineering supply and demand is complex. The time to hire and train engineers within each skill set varies, demand increases and decreases over various time scales, and Draper engineers are not necessarily interchangeable. This system is complex, with underlying relationships between variables. To manage this complexity, Draper needs a tool to model the system. We have created an initial simplistic model utilizing the idea of "Modeling for Learning". The next step is to create focus groups with Draper leadership to formulate a detailed model diagram. Incorporating Draper leadership throughout the modeling process helps ensure completeness and delivery of a tool Draper leadership will use. The goal is to increase the performance of the enterprise by using a leader driven system dynamics model that can support enterprise level scenario planning.

INTRODUCTION

System Dynamics Modeling is a technique used to frame, understand, and discuss complex systems. Modeling complex systems allows for the understanding of the relationships that exist between the variables in our system. Our team is leveraging the idea of using System Dynamics Modeling to represent Draper's complex human enterprise.

A model generated simulation provides information on a possible scenario in the future. Scenario planning gives leaders a tool to create strategies for different futures and see the impact a decision or approach has on the overall system. **The purpose of the model is to provide leaders with a better understanding of their decision implications on the enterprise.**

METHODS

"Modeling for Learning" is a modern view of modeling. Instead of focusing on making a model for a given prediction, we are utilizing leadership throughout the model building process. This stimulates leaders' view on the current system and allows them to learn the dynamics of the complex system as the model is being built.

Our goal is to deliver a tool that multiple leaders can own and manipulate. We are executing this methodology by conducting multiple focus groups throughout the modeling process. Our team has created a simplistic model which represents the high-level processes happening within the system. We are viewing this initial model as a draft that we will bring to focus groups to finalize a complete detailed model diagram.

RESULTS

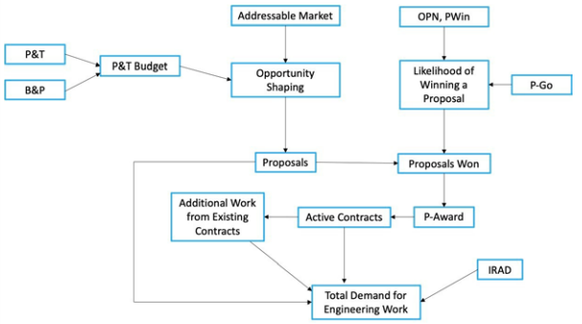

Figure 1. Demand Side of Simplistic Model

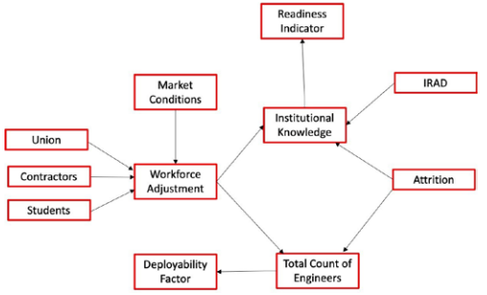

Figure 2. Supply Side of Simplistic Model

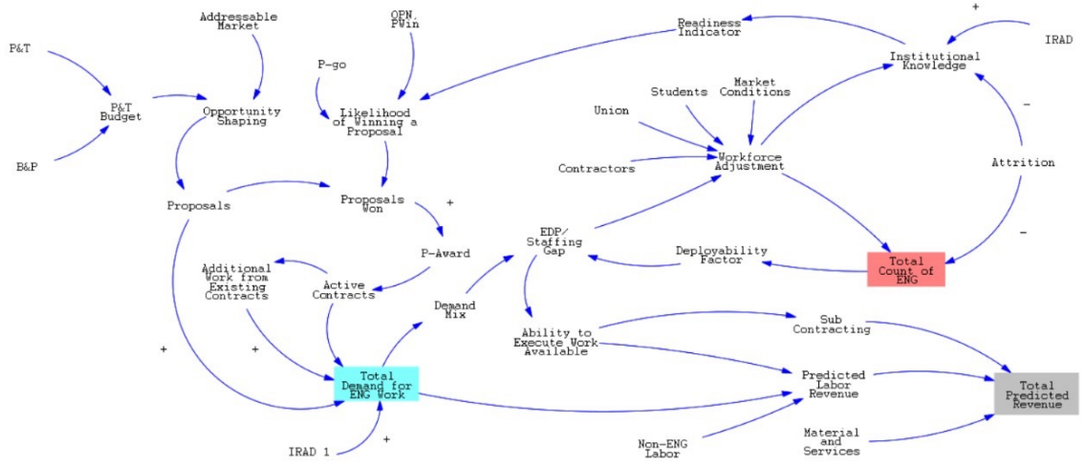

Figure 3. Simplistic Model in Vensim

DISCUSSION

Our team is still in the beginning stages of our project. We have created an initial model, but more steps need to be taken in order to produce a useful product for Draper. Below are some of the current questions we have and will be asking in our focus groups.

- What data sources can we use to increase fidelity?
- What relationships are we missing?
- What variables, or functionality, do we need for this model to be a useful tool in your decision-making process?

CONCLUSIONS

- A simplistic model representing Draper's enterprise was created
- In May, we are conducting multiple focus groups to finalize a complete model diagram
- This summer we will run simulations in the software Vensim
- A second round of focus groups will provide feedback on the model's outputs
- By March 2024 we anticipate being completed with the model building process and anticipate using the model **with Draper leadership to perform scenario planning and determine where the enterprise can increase performance**

REFERENCES

- Morecroft, John, and John Sterman. *Modeling for Learning Organizations*. Productivity Press, 1994.
- Sterman, John. *Business Dynamics : Systems Thinking and Modeling for a Complex World*. Boston, Irwin/Mcgraw-Hill, 2000.

jkoron@draper.com

Addressing Challenges of Visual Terrain Relative Navigation

Dominic Maggio[1*,2], Courtney Mario[1], Brett Streetman[1], Ted Steiner[1] and Luca Carlone[2]

1Draper, [2]MIT, *Draper Scholar

ABSTRACT

Visual Terrain Relative Navigation (TRN) is the task of estimating the position and orientation of a camera given a prior terrain map and has applications ranging from navigation of drones to spacecraft entry decent and landing (EDL). We present a threefold contribution for TRN. **Firstly**, we present an experimental analysis of visual TRN on data collected from a high altitude balloon beginning at an altitude of 33 km and descending to near ground level (4.5 km) with 1.5 hours of flight time and demonstrate less than 290 meters of average position error over a trajectory of more than 150 kilometers. Additionally, we evaluate performance on data collected by two cameras inside the capsule of Blue Origin's New Shepard rocket traveling at speeds up to 880 km/h, and demonstrate less than 55 meters of average position error. **Secondly,** we leverage recent advances in neural implict scene representation (NeRF) for localization and break ground on the potential to replace classical maps used for TRN by developing a localization method coined Loc-NeRF. **Thirdly,** we present a novel approach coined VERF to assert confidence that a pose estimation is correct. For this, we again leverage NeRF and couple probabilistic constraints from two and three view image geometry.

INTRODUCTION

We address three key challenges of Terrain Relative Navigation (TRN):

Challenge: *Visual TRN is difficult to deploy in high altitude and high speed regimes for spacecraft entry decent and landing (EDL) due to a lack of system validation on realistic test data.*

Contribution 1: an experimental validation of TRN on both a high altitude balloon and sub-orbital rocket with added improvements for high altitude missions. [1]

Challenge: Accurate map representation of terrain is at the core of TRN performance. Current classical representations struggle with variable lighting and 3D structures.

Contribution 2: development of a novel approach using a neural implict map representation (NeRF) with future potential to handle 3D terrain at low altitudes and lighting variation [2]

Challenge: TRN is often used in high risk missions such as spacecraft landing. However, there are limited solutions to verify a monocular camera pose estimate is correct.

Contribution 3: a method to verify if a pose estimate is correct without requiring direct depth information [3]

METHODS

Contribution 1 - We use Draper's Image Based Absolute Localization (IBAL) software for experiments

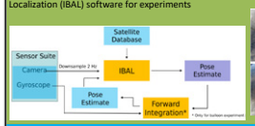

Two cameras mounted to the balloon payload (left) and inside rocket capsule (right)

Contribution 2 - Loc-NeRF:

- Uses a particle filter backbone with NeRF as an implicit map representation
- Particles are propagated with motion model
- Sample of pixels are rendered from NeRF for each particle and compared to sensor image. Less likely particles are pruned
- Pose is determined by weighted average of particles

Particle Convergence

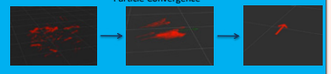

Contribution 3 - VERF: Verifiable Pose Estimation utilizing Neural Radiance Fields

- Given a NeRF, a sensor image I_{gt}, and an estimated pose x_{est} for I_{gt} determine if x_{est} is within ε of the true pose, i.e. $|| x_{est} - x_{gt} || < \varepsilon$ (*)
- Render an image I_{est} at x_{est} with NeRF
- Compute optical flow between I_{est} and I_{gt} and estimate relative offset vector $\hat{x}_{gt}^{est}$
- Pick a test pose $x_{test} = x_{est} + \xi * \hat{x}_{gt}^{est}$ and render I_{test} with NeRF
  -> (*) can now be reduced to an image ordering problem!
- Use geometric constraints to reject outliers and compute confidence score of correctness

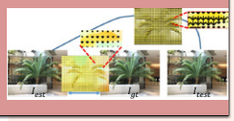

RESULTS

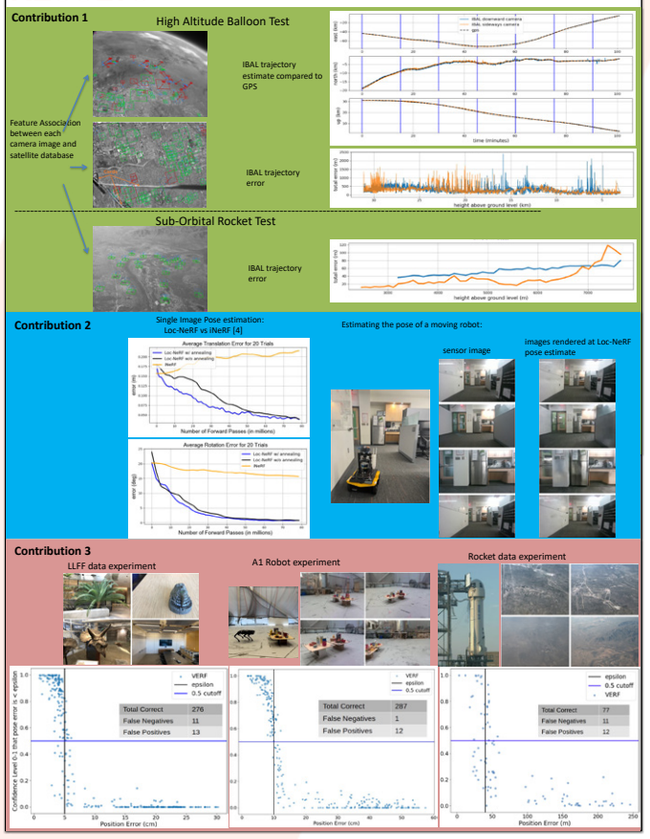

DISCUSSION

Contribution 1:

- IBAL is able to accurately estimate the balloon trajectory over an altitude range of 33 to 4.5 km with average position error less than 290 m. We also demonstrate robustness to dynamic obstruction and rotations over 20 degrees per second.
- IBAL maintains a position error less than 55 m despite the rocket reaching speeds up to 880 km/hr. An anomaly on flight NS-23 triggered the capsule abort system, and thus only partial flight data is included

Contribution 2: Loc-NeRF demonstrates ability to use NeRF as a map for localization with results more accurate than the prior state of the art [4]. Loc-NeRF is also shown to localize a robot on recorded data in real-time.

Contribution 3: VERF shows estimated confidence that a pose estimate has error less than a specified epsilon. Confidence approached 0,1 for errors far from epsilon.

CONCLUSIONS

Contribution 1: IBAL tests demonstrate Draper's TRN algorithm in challenging high altitude and high speed regimes for planetary exploration missions.

Contribution 2: Loc-NeRF provides a promising approach to remove dependancy on classical TRN map representations boosting performance.

Contribution 3: VERF provides a validation method to reduce concerns of using complex TRN algorithms in high risk missions

References

[1] **Maggio, D.**, Mario, C., Streetman, B., Steiner, T. J., & Carlone, L. (2023). Vision-Based Terrain Relative Navigation on High Altitude Balloon and Sub-Orbital Rocket. AIAA SciTech Forum.

[2] **Maggio, D.**, Abate, M., Shi, J., Mario, C., & Carlone, L. (2023). Loc-NeRF: Monte Carlo Localization using Neural Radiance Fields. ICRA.

[3] **Maggio, D**, Mario, C., & Carlone, L. (2023). VERF: Verifiable Pose Estimation Utilizing Neural Radiance Fields. Soon to be Released.

[4] L. Yen-Chen, P. Florence, J. T. Barron, A. Rodriguez, P. Isola, and T.-Y. Lin, "iNeRF: Inverting neural radiance fields for pose estimation," IROS, 2021.

SPARKlab

DRAPER

SCALABLE STEREOLITHOGRAPHY-BASED MONOLITHIC MICROFLUIDIC DEVICE CREATION FOR RAPID BIOLOGICAL SAMPLE ANALYSES

Alex W. Markoski (Draper Scholar)[1,2], Ian Y. Wong[2], Jeffrey T. Borenstein[1]

[1]Draper, Cambridge, MA, USA, [2]Brown University, Providence, RI, USA

ABSTRACT

Microfluidic manipulation and perfusion of multicellular spheroids often utilize device geometries with relatively large channels but smaller trapping features, which are tricky to fabricate with robust bonding. Here, we demonstrate one-step light-directed 3D printing of a sealed monolithic device with enclosed channels and pillar arrays, which we validate for capturing and imaging multicellular spheroids in varying flow. Our approach links computer-aided design with finite element simulations of flow and oxygen conditions, which were experimentally realized. We envision these design and fabrication approaches may be useful in generating rapidly designed multiplexed monolithic arrays for preclinical drug testing in cancer.

Background

- This report describes a monolithic 3D printed microfluidic device for physiologically relevant testing of cancer therapies.
- The 3D printed device was validated via the use of CT26 cancer spheroids.
- Active perfusion and 3D spheroids allow for more in vivo like results compared to static 2D culture.

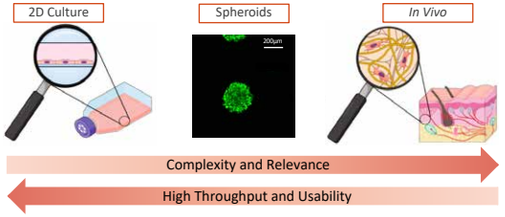

[1]

Device Fabrication

[2]

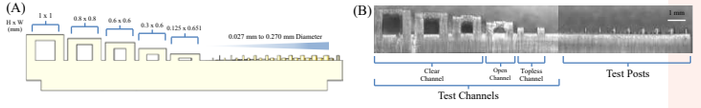

- The Asiga MAX X27 Stereolithography 3D Printer was used in conjunction with the Pro3dure GR-10 resin.
- Printing was optimized using custom resolution testing device seen above in A and B.
- Minimum Resolvable Post Diameter (μm): 81
- Minimum Resolvable Channel Dimensions (μm): 600 H x 600 W

Device Design

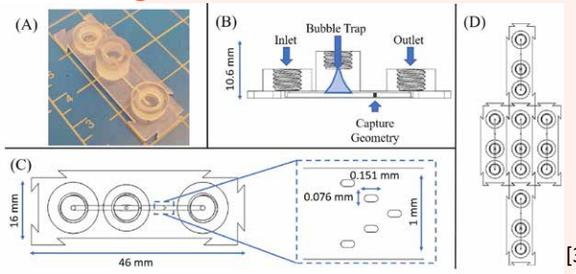

[3]

- Devices can be printed and ready for use within an hour and a half.
- Optimized to capture 200-500μm diameter spheroids.
- Device is cleaned, polished, and post cured in UV and N2.
- New version allows for 80 channels in the space of a 96 well plate.

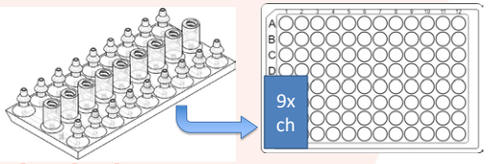

Device Analysis

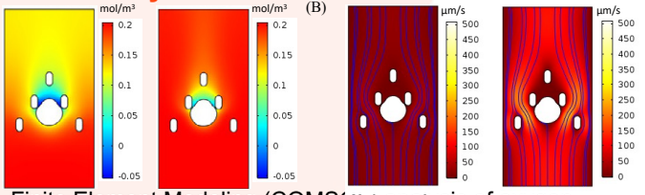

- Finite Element Modeling (COMSOL) analysis of oxygen consumption (A) and velocity intensity (B) on 300μm diameter spheroid.
- Validation of printed dimensions done via scanning white light interferometer.

Spheroid Testing

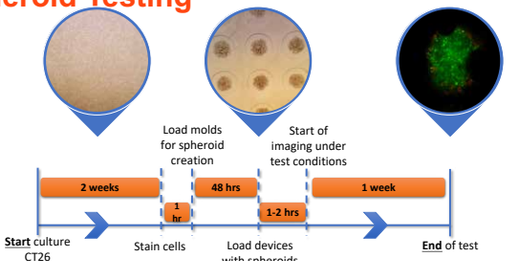

- CT26 cells were pre-treated with CellTracker Green and Annexin V for recording viability over time.
- Flow vs no flow control viability test using 300μm diameter spheroids over the course of 3 days.

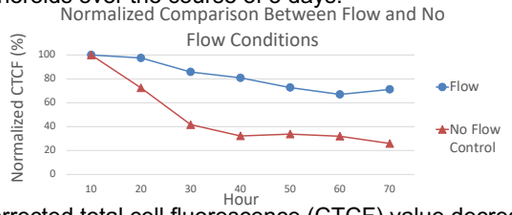

- Corrected total cell fluorescence (CTCF) value decrease by 28% for flow and 74% for no flow control.

Conclusions

- The data presented validates the development of a scalable 3D microfluidic platform for capturing, imaging, and perfusing cancer spheroids.

Acknowledgment

Thanks to the Draper Scholars Program and Brown University for the support.

References

[1] Charwat et al, Cell Culture Technology, 2005
[2] (). Asiga Max UV. Available: https://www.asiga.com/products/printers/max_series/max/.
[3] Markoski A, Borenstein J, Wong I. 3D printed monolithic device for the microfluidic capture, perfusion, and analysis of multicellular spheroids. Frontiers in Medical Technology. 2021.
[4] Beckwith, Ashley L., Jeffrey T. Borenstein and Luis Fernando Velasquez-Garcia. "Monolithic, 3D-Printed Microfluidic Platform for Recapitulation of Dynamic Tumor Microenvironments." Journal of Microelectromechanical Systems 27.6 (2018): 1009-1022.
[5] Beckwith, Ashley L., Luis F. Velásquez-García and Jeffrey T. Borenstein. "Microfluidic Model for Evaluation of Immune Checkpoint Inhibitors in Human Tumors." Advanced Healthcare Materials 8.11 (2019): e1900289-n/a. PubMed. Web <https://onlinelibrary.wiley.com/doi/abs/10.1002/adhm.201900289>.
[6] Moore, Nathan, et al. "A Multiplexed Microfluidic System for Evaluation of Dynamics of Immune-Tumor Interactions." Lab on a chip 18.13 (2018): 1844-1858. MEDLINE - Academic.

BROWN

DRAPER

TEER as a readout of kidney injury in a high-throughput microfluidic human proximal tubule-microvascular model

Erin Shaughnessey[1], Samuel Kann[2], Hesham Azizgolshani[3], Joseph Charest[3], Else Vedula[3]

[1]Draper Scholar, Tufts University; [2]Draper Scholar, Boston University; [3]Draper

ABSTRACT

Acute kidney injury is a common but life-threatening condition with a breadth of causes. To better understand the pathophysiology, there is a need for in vitro models that can replicate multiple forms of kidney injury as well as enhance experimental efficiency. Here, we developed approaches that mimic two major forms of kidney injury in a high-throughput microfluidic model, PREDICT96 (P96), and evaluated rapid trans-epi/endothelial electrical resistance (TEER) sensing as a non-invasive metric of injury response for human primary proximal tubule (PT)-microvascular tissues. Tissue barrier integrity was measured at least daily with the P96 rapid TEER system, which took less than 8 minutes for all 96 devices. Tissues exhibited dose-dependent TEER changes in response to a nephrotoxic compound, and injury was identified within 24 hours of exposure prior to significant cell death. TEER revealed an unexpected tightening of the tissue barrier during exposure to static low oxygen conditions, mimicking ischemia, which was dependent on loss of fluid shear stress (FSS). Rapid TEER sensing provided novel insights into kidney injury response with improved efficiency and sensitivity compared to other metrics, demonstrating the potential to strengthen kidney injury research.

BACKGROUND

PREDICT96 (P96)

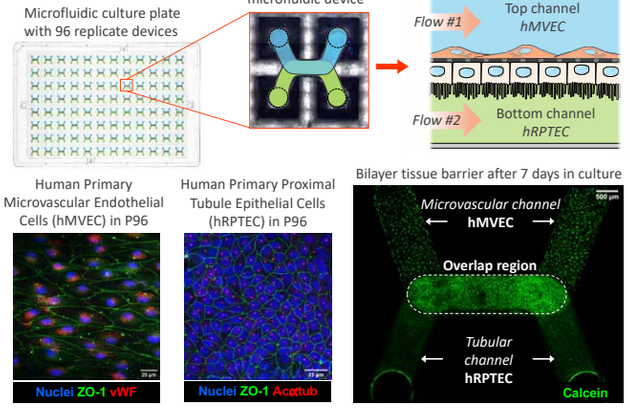

Trans-Epi/Endothelial Electrical Resistance (TEER)

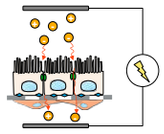

TEER = Electrochemical resistance across a tissue barrier
- Measured by applying AC and sensing voltage drop across tissue
- Higher resistance associated with 'tighter'/stronger tissue barrier
- Can be an indicator of tight junction formation/disruption

P96 microfluidic pump with integrated TEER measurement

Independent fluid flow & TEER measurement for each device

Kidney model forms in-vivo-like *"leaky"* barrier within a week under fluid flow

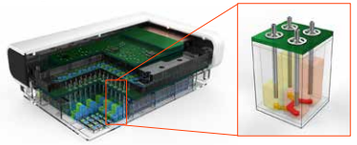

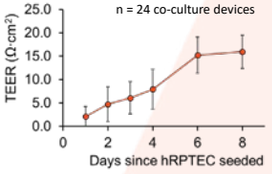

OBJECTIVE

Evaluate the use of TEER for monitoring response of human primary derived-kidney tissue in multiple injury settings in a flow-enabled high-throughput system

METHODS

Drug-induced toxicity

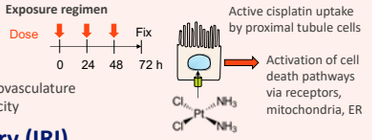

Cisplatin (5, 15, 25 µM in normal saline)
- Model nephrotoxin impacting PT & microvasculature
- Well-characterized dose-dependent toxicity

Ischemia-reperfusion injury (IRI)

- Loss of perfusion that prevents delivery of oxygen/nutrients and removal of wastes
- Static conditions yield hypoxic microenvironment in the P96 device

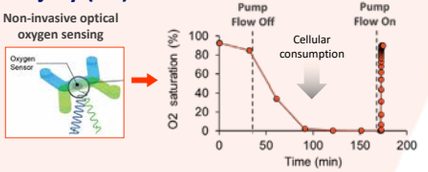

RESULTS

Toxicity – Change in TEER depends on nephrotoxic dose, physiological FSS impacts hRPTEC functional response

Fluid shear stress (FSS)
0.01 dyn/cm²
0.70 dyn/cm²

Dose and **FSS** have a significant impact on barrier function after 24 and 48 hours of exposure, respectively (two-way ANOVA, $P<0.001$)

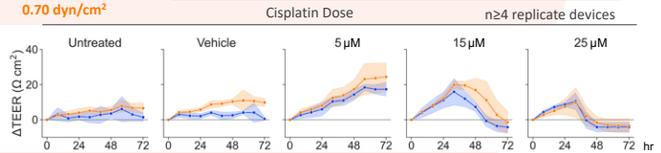

hRPTEC tight junctions (ZO-1) after exposure for 72 h:

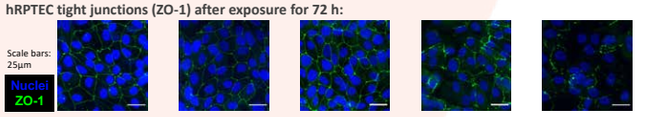

Toxicity - TEER detects tissue response to cisplatin sooner than standard cell death assay

Cell death vs. TEER after 72 h exposure

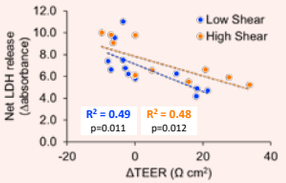

After 24 h exposure to 15 µM cisplatin, only TEER detects significant change

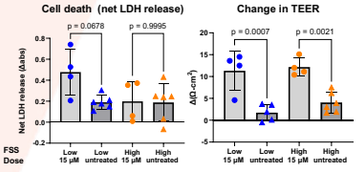

IRI - TEER reveals distinct responses to injury phases dependent on loss of FSS & oxygen

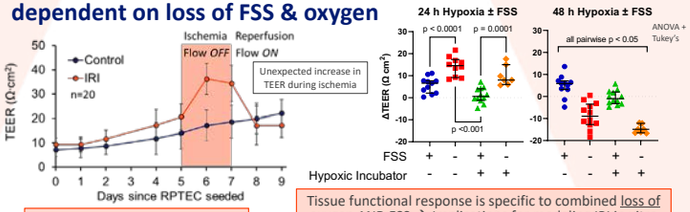

Loss of hRPTEC polarity after IRI in P96, a hallmark of IRI in vivo

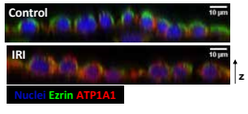

Tissue functional response is specific to combined loss of oxygen AND FSS → Implications for modeling IRI in vitro

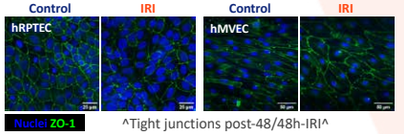

^Tight junctions post-48/48h-IRI^

IRI - TEER enables long-term tracking with high resolution

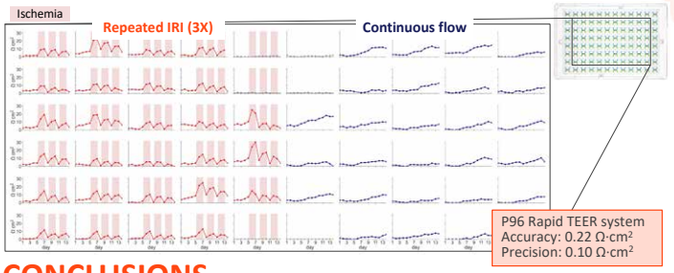

P96 Rapid TEER system
Accuracy: 0.22 Ω·cm²
Precision: 0.10 Ω·cm²

CONCLUSIONS

- TEER captures the dynamic responses of human primary kidney tissues to multiple types of injury and has the potential to deliver novel insights not provided by existing metrics
- **Toxicity**: TEER demonstrated dose dependence of tissue barrier function and offered improved sensitivity over a standard toxicity assay
- **IRI**: TEER revealed an unexpected increase in barrier function and highlighted distinct role of FSS during loss of oxygen, an important consideration for IRI in vitro modeling

IMPACT

- Non-invasive & label-free: continuous tissue monitoring, no sacrificial replicates
- Rapid, scalable & accurate: readouts for 96 replicates in < 8 minutes
- Current work sets the stage for real-time automated TEER measurement during active unidirectional flow in the incubator

April 2023

This work was supported by the Draper Scholar Program. This work was supported by NSF Grant Award Number 1804845 (PI Vedula). This material is based upon work supported by the National Science Foundation Graduate Research Fellowship under Grant No. 1842474. Any opinions, findings and conclusions or recommendations expressed in this material are those of the author(s) and do not necessarily reflect the views of the National Science Foundation.

References:
Hoste, *et al.*, *Nat Rev Nephrol* **14**, 607–625 (2018)
Azizgolshani, Coppeta, Vedula *et al.*, *Lab Chip* **8**, 1454-1474 (2021)
Kann *et al.*, *Microsyst Nanoeng* **8**, 109 (2022)
Shaughnessey *et al.*, *Sci Rep* **12**, 13182 (2022)

DRAPER

Engineering topological materials for one-way energy transport and next generation infrared detection

Morgan Blevins (Draper Scholar)[1,2], Mark Witinski[2]

[1] Department of Aeronautics and Astronautics, Massachusetts Institute of Technology, Cambridge, MA 02139, USA
[2] The Charles Stark Draper Laboratory Inc., Cambridge, MA 02139, USA

ABSTRACT

Dirac and Weyl semimetals, materials which were first physically synthesized only in the last decade, are referred to as the "3D" cousins of graphene due to their unique properties which make them attractive candidates for encoding quantum information, enabling unidirectional energy transport, and designing infrared detectors. First, we present modeling as well as new theory showing that applying *in situ* strain and *ex situ* bias current and optical pumping can widely tune the nonreciprocal response of Weyl semimetals for unidirectional energy transport applications. Next, we are building infrared detectors from Weyl semimetals that are sensitive to light wavelength *and* polarization (linear vs. circular). These devices have applications in highly sensitive infrared photodetection and fundamental transport studies. We aim to show that strain enhances the photo response of these devices.

I. ENGINEERING ONE-WAY ENERGY TRANSPORT

We can engineer materials to have unidirectional optical modes, which enable efficient energy transfer and reduced noise in optical systems like lasers or integrated photonics

- *Surface plasmon polaritons* are an optical mode that exists as the interface of a dielectric and metal
- In this work we present new models and theory around engineering nonreciprocal surface plasmon modes

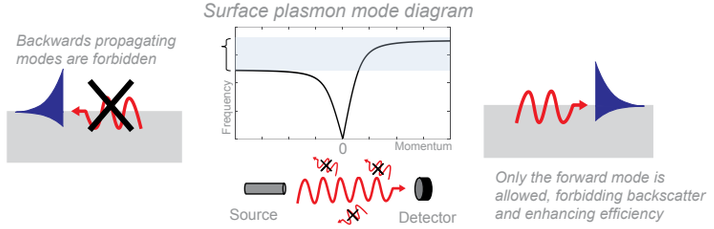

A. Strain Engineering

- We modeled how straining a Weyl semimetal can induce and tune the nonreciprocity of optical modes
- Modeled mode diagrams show tunable one-way transport:

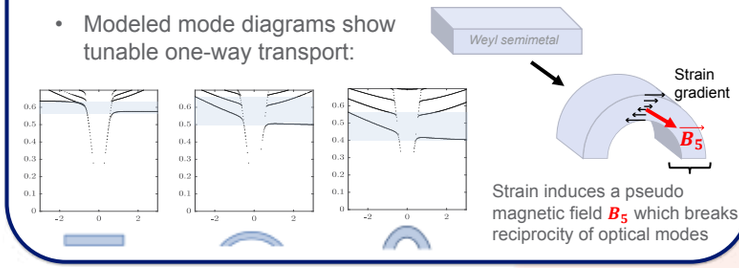

Strain induces a pseudo magnetic field B_5 which breaks reciprocity of optical modes

B. Current drag

- Drift current imparts a **Doppler shift on optical surface modes**
- We have derived the optical response expected in a Weyl semimetal due to this effect

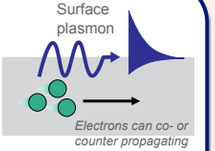

Optical conductivity model:

$$\sigma^{drift}(\omega, q) = \frac{\omega}{\omega_0}\sigma(\omega_0, q_0)$$

$$\omega_0 = \gamma(\omega - uq), \quad q_0 = \gamma\left(q - \frac{u}{v_F^2}\omega\right), \quad \gamma = \sqrt{1 - u^2/v_F^2}$$

$$\downarrow$$

$$\sigma^{drift}(\omega, q) \neq \sigma^{drift}(\omega, -q)$$

C. Optical pumping

- We propose that **ultrafast photocurrent in Dirac and Weyl semimetals can induce appreciable current drag**, a pumping mechanism not yet explored for this application
- In the modeling we show that under realistic conditions, sizable nonreciprocity is achieved

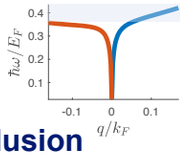

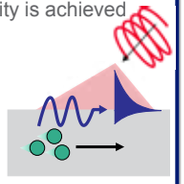

D. Conclusion

We have proposed and modeled *in situ* and *ex situ* stimuli to induce nonreciprocal transport in Weyl semimetals, **unlocking new mechanisms for unidirectional optical devices.**

II. NEXT GENERATION INFRARED DETECTION

Building on the unique electrical and optical properties of Weyl and semimetals explored in thrust I, we are creating infrared detectors that are sensitive to infrared wavelength *and* polarization. We aim to show that strain enhances photo response of these devices.

A. Infrared detector chip preparation

We place electrode pads on the exfoliated Weyl semimetal flakes via nanofabrication, enabling electrical analysis

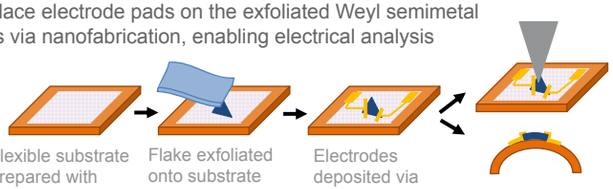

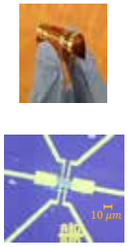

Fabricated Weyl semimetal cell

B. Next steps: Experimental characterization

- With our Weyl semimetal cell, we will soon begin photocurrent experiments
- We are building a **custom scanning photocurrent microscopy.** This will map photocurrent magnitude to the location of illumination, elucidating underlying physics of the photo response
- We will then apply strain to the samples, evaluating how it enhances photocurrent

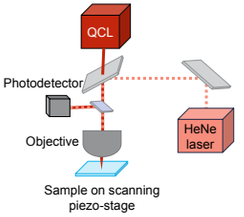

This work will pave the way to new, highly sensitive IR detectors

ACKNOWLEDGMENTS

Thank you to Dr. Pavlo Sukhachov, Dr. Yoichiro Tsurimaki and Simo Pajovic for helpful discussions on Weyl semimetal physics. Thank you to our collaborator, Thanh Nguyen, for synthesis of Weyl semimetal crystals and nanofabrication of cells.

Massachusetts Institute of Technology

DRAPER

Learning to Forecast Aleatoric and Epistemic Uncertainties over Long Horizon Trajectories

Aastha Acharya. (Draper Scholar)[1,2], Rebecca Russell[1], Nisar Ahmed[2]

[1]Draper Laboratory, 2University of Colorado, Boulder

ABSTRACT

Giving autonomous agents the ability to forecast their own outcomes and uncertainty will allow them to communicate their competencies and be used more safely. We accomplish this by using a learned world model of the agent system to forecast full agent trajectories over long time horizons. Real world systems involve significant sources of both aleatoric and epistemic uncertainty that compound and interact over time in the trajectory forecasts. We develop a deep generative world model that quantifies aleatoric uncertainty while incorporating the effects of epistemic uncertainty during the learning process. We show on two reinforcement learning problems that our uncertainty model produces calibrated outcome uncertainty estimates over the full trajectory horizon.

INTRODUCTION

Long horizon forecasting of trajectories requires accounting for two uncertainty types:

Aleatoric (irreducible): arises from data due to noise, unobserved variables, or inherent stochasticity

Epistemic (reducible): arises from model from insufficient data, out of distribution testing, modelling errors

Because **aleatoric uncertainty is naturally intertwined with epistemic uncertainty**, have to actively account for this to ensure no double-counting or miscounting of uncertainty

Contribution: new method of quantifying aleatoric uncertainty for dynamical systems that accounts for systemic epistemic uncertainty

METHODS

Use residual to define the difference between observed and forecasted trajectories. Since the difference occurs due to uncertainties, can write total residual ϵ_{total} as:

$$\epsilon_{total} = \underbrace{\epsilon_{alea}}_{\text{aleatoric}} + \underbrace{\epsilon_{epist}}_{\text{epistemic}}$$

Deep Ensembles for Epistemic Uncertainty

To place a **distribution over model parameters**, use state-of-the-art **deep ensembles** to quantify epistemic uncertainty – this allows epistemic residual to be defined as:

$$\epsilon_{epist} = \hat{\mathbf{y}}_m - \frac{1}{M}\sum_{m=1}^{M} \hat{\mathbf{y}}_m \quad \text{where} \quad \underbrace{\hat{\mathbf{y}}_m = \{\hat{\mathbf{s}}^m_{1:T}\}}_{\substack{\text{forecasted states up to time horizon } T \\ \text{from } m = 1{:}M \text{ ensemble models}}}$$

Total residual can be defined as:

$$\epsilon_{total} = \mathbf{y}_{true} - \frac{1}{M}\sum_{m=1}^{M} \hat{\mathbf{y}}_m \quad \text{where} \quad \underbrace{\mathbf{y}_{true} = \{\mathbf{s}_{1:T}\}}_{\substack{\text{observed states up to time horizon } T}}$$

METHODS

Deep Generative Models for Aleatoric Uncertainty

Aleatoric residual can be defined as:

$$\epsilon_{alea} = \epsilon_{total} - \epsilon_{epist} = \mathbf{y}_{true} - \hat{\mathbf{y}}_m$$

Use **deep generative models to learn the distribution of aleatoric residuals** given initial observed states $\mathbf{s}_0$ and an action sequence $\mathbf{a}_{1:T}$:

$$p(\epsilon_{alea,1}, \epsilon_{alea,2}, \dots, \epsilon_{alea,T} | \mathbf{s}_0, \mathbf{a}_0, \mathbf{a}_1, \dots, \mathbf{a}_T)$$

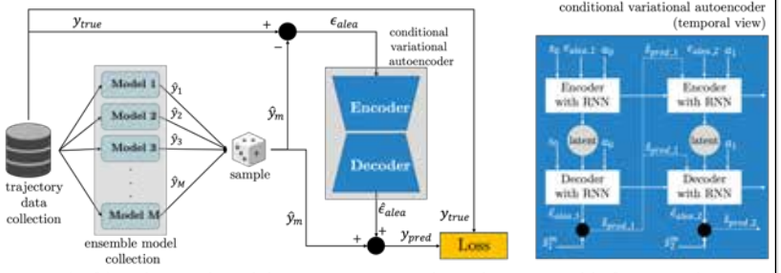

Fig. 1 (Left) End-to-end model training process where deep ensemble forecasted states are used alongside observed states to define the aleatoric residual and train the conditional variational autoencoder. (Right) Temporal view inside the conditional variational autoencoder, which is the deep generative model for aleatoric uncertainty

RESULTS

- Experiments on:
  - Two reinforcement learning environments: Pusher and UAV
  - Two levels of uncertainty: low epistemic + high aleatoric
    high epistemic + high aleatoric
- Comparison against two models: probabilistic multi-layer perceptron (MLP)
  full variational autoencoder (VAE)
- Evaluation metrics: maximum mean discrepancy (MMD) and Brier score
- **Results** for both the Pusher and UAV environments show a **close distribution match to the true distribution** and **accurate predicted probabilities** for outcomes of interest

RESULTS

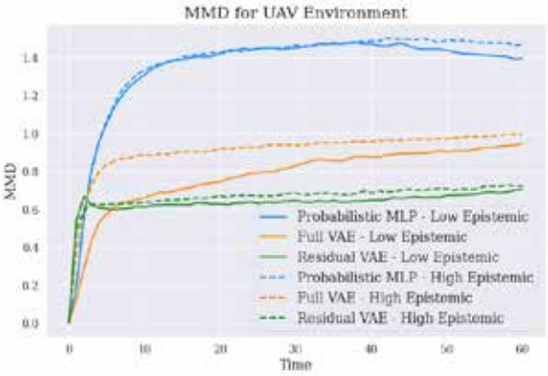

Fig. 2 Representative results showing maximum mean discrepancy (MMD) for the UAV environment in low epistemic + high aleatoric (solid line) and high epistemic + high aleatoric (dashed line) scenario. Lower MMD values are better, showing effectiveness of residual VAE (green - our model)

CONCLUSIONS

- Deep generative model in the form of conditional variational autoencoder can be trained to learn aleatoric uncertainty while accounting for epistemic uncertainty
- Results shows the effectiveness of our model in providing autonomous agents the ability to forecast their own uncertainties and outcomes, resulting in competency aware agents

ACKNOWLEDGMENTS

This material is based upon work supported by the Defense Advanced Research Projects Agency (DARPA) under Contract No. HR001120C0032. Any opinions, findings and conclusions or recommendations expressed in this material are those of the author(s) and do not necessarily reflect the views of DARPA.

Autonomous Cislunar Navigation

Omar Awad(Draper Scholar)[1], Matthew R. Stoeckle[1], and Kenshiro Oguri[2]

[1]The Charles Stark Draper Laboratory, [2]Purdue Aeronautics and Astronautics

ABSTRACT

Cislunar and high-altitude spacecraft navigation can be difficult without access to GNSS signals or NASA's Deep Space Network (DSN). Current high-altitude methods of GNSS/DSN-independent navigation are either too computationally expensive, inaccurate, or immature for practical implementation. Presented here is a fully autonomous approach with simulated results for a formation of two satellites in a Near Rectilinear Halo Orbit (NRHO) demonstrating the feasibility and accuracy of this approach.

Navigation Approach

What is required?

- Two satellites (a chief and deputy).
- One satellite (chief) hosts an Extended Kalman Filter (EKF) and sensor suite.
- Sensor suite can measure chief inertial attitude, inter-satellite range, and chief body-referenced direction of deputy satellite relative to chief.
- EKF equipped with Earth-Moon three-body gravity model.

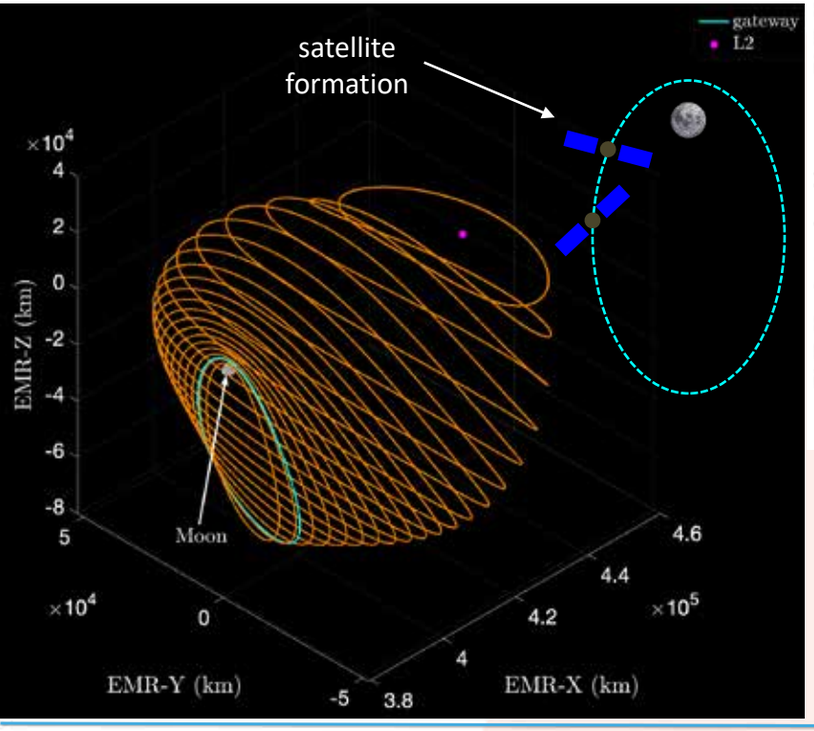

Assumptions

Reflected in the simulation results below

- Non-gravitational accelerations are not considered.
- Chief satellite inertial attitude estimates are very accurate.

Measurement Accuracy

Range, azimuth, and elevation measured

- 1m 1σ range accuracy
- 0.1° 1σ azimuth angle accuracy
- 0.1° 1σ elevation angle accuracy

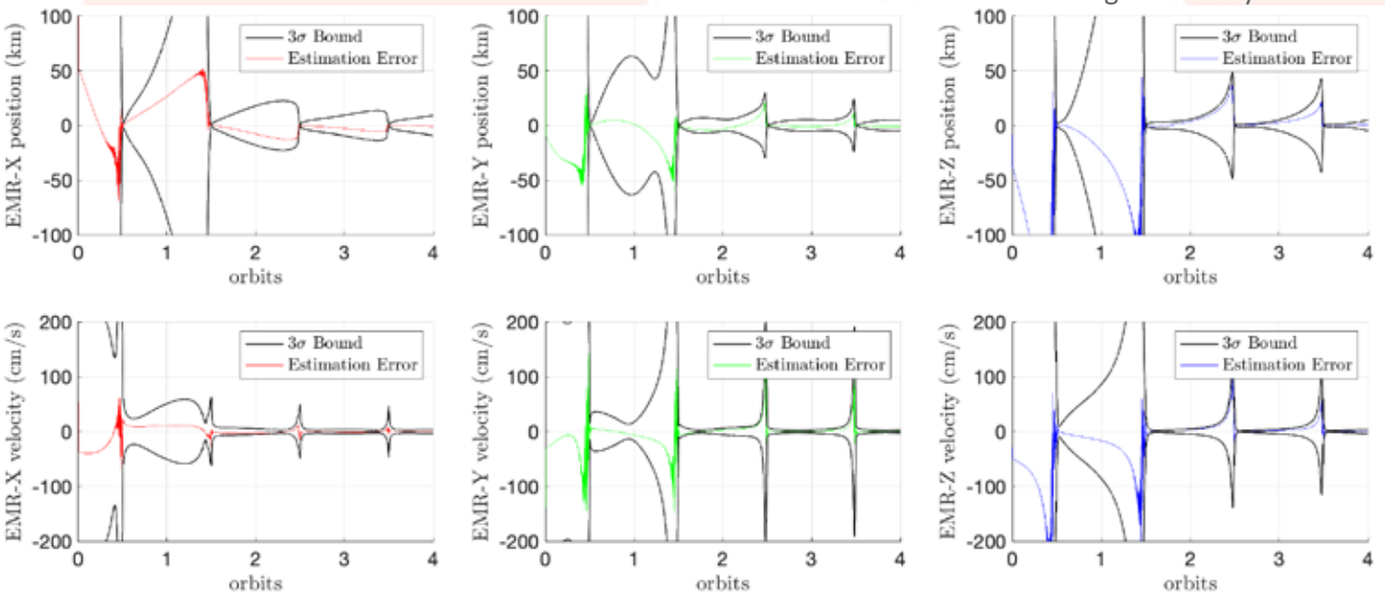

3σ	x_0 (m)	y_0 (m)	x_0 (m)	$\dot{x}_0$ (cm/s)	$\dot{y}_0$ (cm/s)	$\dot{z}_0$ (cm/s)
Min	149.5	269.9	539.7	2.138	1.685	0.937
Max	13,100	23,860	42,120	46.82	190.6	113.4

Maximum intersatellite range is 30 km. Despite nonlinear measurements and large initial uncertainty, position error 3σ falls well below 1 km per axis while velocity error 3σ falls well below 10 cm/s. These results show that this navigation system works well in a gateway-like orbit and is viable for cislunar navigation. This solution is also computationally efficient, making it more feasible for cubesat applications.

Evaluation of the Gravity Loading Countermeasure Skinsuit in Short-Duration Human Spaceflight

Rachel Bellisle[1,2], Katya Arquilla[3], Lonnie Petersen[2,3], Andrea Webb[4] and Dava Newman[2,3,5]

[1]Draper Scholar, The Charles Stark Draper Laboratory, Inc., [2]Harvard-MIT Health Sciences and Technology Program, Massachusetts Institute of Technology,
[3]Department of Aeronautics and Astronautics, Massachusetts Institute of Technology, [4]The Charles Stark Draper Laboratory, Inc., [5]MIT Media Lab

ABSTRACT

The Gravity Loading Countermeasure Skinsuit (GLCS) is a countermeasure garment for astronauts that provides axial loading on the body to simulate some effects of Earth's gravity (1G) and aims to mitigate physiological deterioration due to microgravity [2-4]. The goal of the GLCS experiment in an International Space Station (ISS) mission is to build on prior work by collecting data on an additional astronaut participant and explore new features and applications for the suit. The study aims to 1) evaluate & characterize the loading function and comfort of the GLCS during spaceflight, and 2) investigate the physiological effects of the GLCS as a musculoskeletal countermeasure in prolonged exposure to microgravity, including effects on backpain & spinal elongation, sensorimotor function, and exercise performance.

INTRODUCTION

In reduced gravity, the human body no longer experiences the constant loading provided by Earth's gravity. Muscles atrophy due to disuse, the spine elongates, which may cause back pain and discomfort, and sensorimotor changes lead to impaired posture and locomotion [1].

The Gravity Loading Countermeasure Skinsuit (GLCS) (Figure 1) aims to simulate some of the loads provided by Earth's gravity with potential applications in mitigating spinal elongation, muscle loss, and sensorimotor changes. This wearable system is intended to supplement exercise countermeasures during future missions beyond low Earth orbit and to further mitigate microgravity-induced physiological effects during current mission scenarios on the International Space Station (ISS).

***Fig. 1. The Mk-7 Gravity Loading Countermeasure Skinsuit** with A) shoulder yoke, B) longitudinal fabric tension in the loading material, C) circumferential fabric tension in the loading material, and D) stirrups secured under the sole of shoes with rigid insoles. (modified from [5]).*

The GLCS will be flying to the ISS on Axiom Mission 2 (Ax-2), a private crew mission to the ISS planned to launch in Spring 2023.

STUDY AIMS

Aim 1: To evaluate & characterize loading functions, comfort, and mobility of the GLCS during spaceflight.

Aim 2: To investigate the physiological effects of the GLCS as a musculoskeletal countermeasure in prolonged exposure to microgravity, including effects on

- back pain (Aim 2.1)
- sensorimotor function (Aim 2.2)
- exercise performance (Aim 2.3)

METHODS

- One participant was consented for this study approved by the NASA Institutional Review Board (IRB).

Fig. 2. Timeline of Experiment Sessions

Exercise Testing

- A 35-minute exercise protocol was developed for short duration inflight use with the GLCS and other low-volume equipment. The protocol includes lower body and torso resistance exercise with TheraBand® resistance bands.
- ***In-flight testing*** (Fig. 2) includes 3 suited exercise sessions and 1 unsuited (control) session, during a 10-day mission on the ISS (12 days on orbit)
- Suited and unsuited exercise testing during ***pre-flight baseline data collection*** (Fig. 2) will provide a 1G control.
- Measurements include:
  - Electromyography (EMG) to observe muscle activity (Pre-Flight Only)
  - Heart rate and respiration rate collected with a Fitbit watch
  - Body kinematics captured with video footage
  - Qualitative feedback, including ratings of perceived exertion [6]

Sensorimotor Testing

- The study includes functional tests to assess sensorimotor performance, collected pre-flight (L<50 days) and post-flight (R+0, R+1, and R+4±3 days) .
- Tests include NASA's standard measures [7] (Fig. 3), for comparison to existing NASA datasets from short duration spaceflight [8].
- Measurements include:
  - Head and torso movement, measured with inertial measurement units (IMUs)
  - Video observation of task performance
  - Task duration

***Fig. 3. NASA's Sensorimotor Standard Measures tests** including Sit-to-Stand, Tandem Walk, and Recovery from Fall (Photos from NASA [7]).*

DISCUSSION

- For exercise testing, a within-subject comparison will be performed to compare the participant's suited and unsuited performance and their 1G and microgravity performance. Hypotheses include:
  - EMG amplitude in lower body and torso muscles will be greater while using the GLCS compared to unsuited conditions
  - Heart rate, respiratory rate, and perceived exertion will be greater while using the GLCS compared to unsuited conditions

  This testing will assess the ability of the GLCS to target key muscles affected by spaceflight and augment exercise workload.
- For sensorimotor testing, a between-subject comparison will be performed, comparing the 1 suited participant to previous (unsuited) participants from short-duration spaceflight in published literature [8]. The primary hypothesis is:
  - Participants who use the GLCS in-flight will show attenuated changes between pre- and post- flight performance, as assessed with sensorimotor tests.
- This study was developed to accommodate many constraints and ISS requirements, Additionally, the single participant is a significant limitation, and led to an experiment designed for one-participant characterizations and replication of previous methods for comparison to additional participants.

CONCLUSION

The GLCS developments resulting from this investigation aim to support human health and performance in current mission scenarios on the ISS and future missions to the Moon and Mars where low-mass countermeasures will be highly valuable for space-constrained long-duration spacecraft.

ACKNOWLEDGMENTS

Thank you to the Draper Scholar Program for supporting this work. Thank you to the many team members and mentors from the MIT Human Systems Laboratory and to colleagues and collaborators at MIT Space Exploration Initiative, Axiom Space, and the NASA Neuroscience Laboratory.

REFERENCES

[1] J. Buckey, Oxford Press, 2006; [2] J. Waldie and D. Newman, Acta Astronautica, 2011; [3] R. Bellisle and D. Newman, 50th International Conference on Environmental Systems, 202.; [4] J. M. Waldie and D. J. Newman, U.S. Patent US 8,769,712 B2, Jul., 2014; [5] Bellisle, et al., IEEE Aerospace, 2022; [6] G. Borg, Psychologica, 2004.; [7] G. Clement, et al., Human Research Program Investigators' Workshop, 2020; [8] C. Miller, et al., Aerospace Medicine and Human Performance, 2018.

Optical Phase Change Materials for Integrated Photonic Devices

Brian Mills[1,2], Dennis Callahan[1], Sarah Geiger[1], Michael Moebius[1], Juejun Hu[2]

[1]The Charles Stark Draper Laboratory, Inc, Cambridge, MA, 02139
[2]Massachusetts Institute of Technology, Cambridge, MA, 02139

ABSTRACT

Phase change materials (PCMs) exhibit a large change in their material properties when transitioned between amorphous and crystalline structures. While traditionally used in electronic memory devices, new optical phase change materials has led to their use in low loss, low power consumption photonic modulators. In order realize their full potential, we analyze material related failure in cycled PCM devices and outline necessary steps for development of a robust PCM modulated photonics platform.

INTRODUCTION

Active integrated photonic devices manipulate light on-chip, a critical capability for a plethora of emerging technologies such as LIDAR, biomarker sensing and quantum information processing and communication. Utilization of phase change materials (PCMs) has been identified as a promising direction for reducing power consumption and increasing optical contrast in photonic devices. In this work we analyze failure modes in PCMs in integrated photonic devices, and suggest methods for mitigating failure and improving PCM cycling.

METHODS

1. Device Fabrication

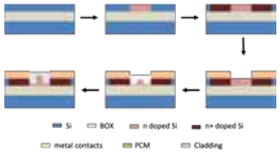

2. Device Cycling

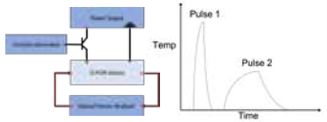

3. Post-failure Material Analysis

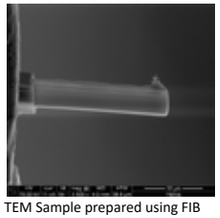

TEM Sample prepared using FIB

- Fabricate and cycle integrated photonic PCM devices.
- Identify dominant PCM failure modes.
- Mitigate failure via optimized device design.

RESULTS

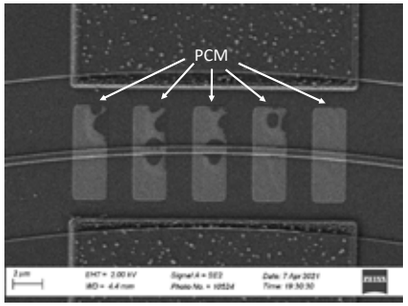

- SEM shows formation of large voids during PCM cycling due to interface instability.

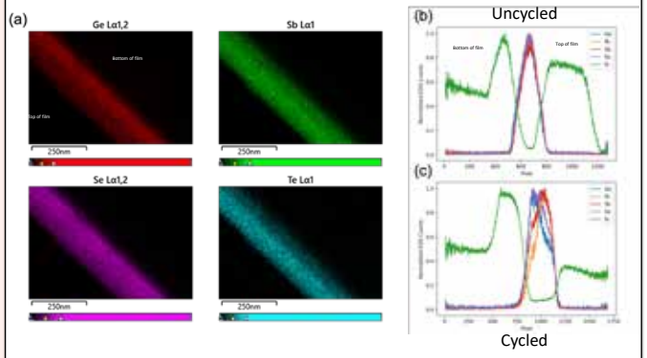

- STEM/EDS results show elemental segregation as a result of extensive PCM cycling.

DISCUSSION

- Main PCM failure is associated with morphological instability and elemental segregation.
- Curating PCM-capping interface is key to reducing material retraction during cycling.
- Elemental segregation associated with large temperature gradient.

CONCLUSIONS

- PCM integration in photonic systems is limited by their cycling capability
- Solutions should target morphological stabilization of PCM and reduction of thermal gradients.
- Future work:
  - Test alternate capping layers, and study effects of capping layer stress on PCM stability.
  - Explore new heater and PCM geometries to minimize temperature gradient

ACKNOWLEDGMENTS

We would like to acknowledge the support of the Draper Scholar Program, as well as extensive support from the QPGA team at Draper and the Photonics Materials research group at MIT.

Multi-Agent Reinforcement Learning for Collision Avoidance

2LT Caroline Vincent (Draper Scholar)[1,2], Dr. Brian Wang [1], Dr. Michael Ricard [1], and Prof. Sertac Karaman [2]

[1] Draper [2] Massachusetts Institute of Technology

ABSTRACT

Swarm technology requires the avoidance of dynamic obstacles moving at increasingly high speeds, making static object avoidance systems insufficient. This work aims to use reinforcement learning to teach multiple agents within a swarm to complete tasks without colliding into one another. Once trained, this algorithm can then be incorporated into other reinforcement learning models with different applications.

INTRODUCTION

Fully autonomous vehicles within a swarm cannot rely solely on predetermined flight paths because they make decisions depending on the unfolding environment after beginning a mission. For successful collision avoidance within swarms, each UAV must know the locations of, or recognize, neighboring UAVs to prevent them from crashing into one another. I want to use reinforcement learning to teach multiple agents within a swarm to complete tasks without colliding into one another.

METHODS

- I am using a custom environment created in PettingZoo to generate my states, agents, actions, obstacles, goals, and reward systems
- I am using a Deep Q-Network (combining Q-learning with deep neural networks) to approximate the state-value functions and generate the actions for agents at each time step
- I am employing several common RL techniques within my model such as an epsilon-greedy policy and experience replay

RESULTS

- The graphic below illustrates the custom environment used to run my simulations. I am starting with two agents in the top left, two goals in the bottom right, and obstacles throughout the grid
- In each state, the agents select an action of moving up, down, left, right, or staying in place
- Rewards are generated for reaching the goals, while penalties are given for crashing into an obstacle or agent. An episode terminates when a goal is reached, or when a crash occurs
- The total amount of rewards are tracked over time to visualize the learning taking place throughout the number of episodes run

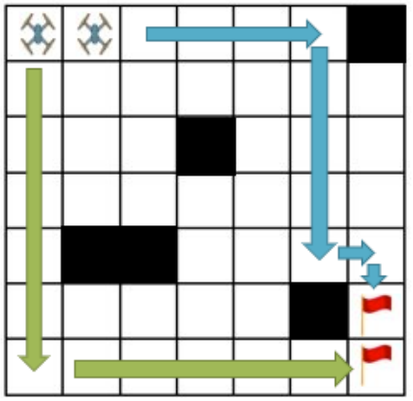

DISCUSSION

- My results thus far showcase that using a Deep Q-Network performs far better than other RL types such as Hill Climbing Algorithms or Q-Networks. The epsilon-greedy policy and experience replay also illustrate an improved performance in comparison to using the algorithm without those techniques
- I hope to prove that collision avoidance among agents in a swarm can be learned through reinforcement leaning algorithms. I want this learned behavior to have measures that allow for easy integration into other types of multiagent use cases as just one factor of performance among a range of larger goals

CONCLUSIONS

I aim to move this work from a discrete state and action space to continuous states and actions as well as simulating on a 3D grid. I also plan to expand my model to incorporate more agents and will analyze the relative learning rates among the different scopes. Additionally, I plan to expand the reward system to reward more efficient paths and consider time when evaluating how well an agent is performing.

ACKNOWLEDGMENTS OR REFS

- Draper Advisors: Brian Wang, Michael Ricard
- MIT Advisors: Sertac Karaman, Andrea Henshall

Estimating the Cost to Transition a Space System from Expendable to Reusable

Ryan de Freitas Bart[1,2], Kevin Duda[2], and Jeffrey Hoffman[1]

[1]Massachusetts Institute of Technology, [2]Draper

ABSTRACT

The large initial financial investment and technical challenges of developing reusable space systems hinder their further proliferation. One method to mitigate these challenges is to first develop an expendable version of a system then transition it to reusable when required. A significant drawback of this approach is the risk associated with developing two distinct versions of a system. To help address this issue, we created a cost estimation method to be used for design optimization of such systems.

INTRODUCTION

- High cost of developing space systems limits humanity's further expansion in space
- Hardware reusability has demonstrated cost reductions with several companies currently developing or operating reusable systems
- Reusable space systems are more difficult to develop than expendable as they require sufficient reliability to execute several flights and ability to perform the additional functions necessary for reuse
- These challenges lead organizations to pursue iterative approaches motivated by agile methodology where each iteration tackles a smaller technical challenge

METHODS

Iterative Reusable Development Program

- Development program where expendable version is first developed then transitioned to reusable when desired
- Focus on case with only one expendable and one reusable version of a system for entire program

Research Gap

- No previous work has investigated expendable to reusable transition cost estimation
- Need for method to estimate the development cost for iterative reusable development programs

COST ESTIMATION MODEL

- Divide system into entities where divisions can exist at any level of design and are determined by the user depending on available cost estimation models
- Cost expendable version first using cost estimating relationships (CERs) or analogous cost estimates
- Refine expendable design cost using factors
  - $C_{Expen} = \sum_{\forall e} f_C f_G f_I f_R f_D C_e$
- Use expendable cost as baseline to estimate transition cost by analyzing each of the entities added or modified to make system reusable
  - $C_{Reus} = \sum_{\forall m} (f_R f_C f_T - 1) C_m$
- Factors modify initial cost estimates to account for different attributes of each design

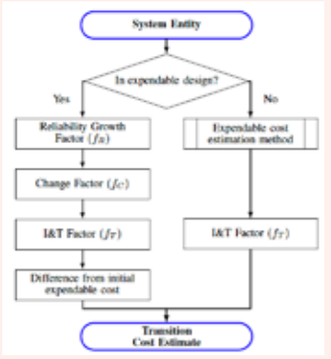

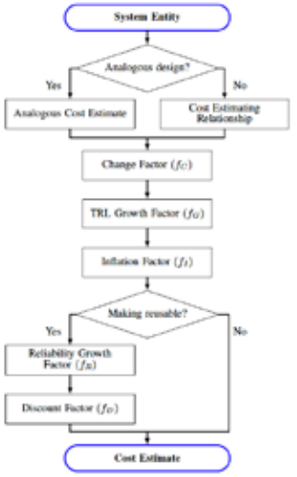

DISCUSSION

- This model provides a flexible cost estimation methodology that accounts for reusability at entity level and can be applied to wide range of space systems
- Model is also lightweight and requires minimal user judgement making it useful for calculating cost where many potential designs must be analyzed
- Primary disadvantages of model are it provides low-fidelity cost estimates and requires SME judgement for Change and Integration & Test factors

CONCLUSIONS

Applications

- Useful for design optimization during early design stage of iterative reusable development programs for tradespace exploration and understanding impact of design choices
- Can be adapted for reusable system cost estimation by using transition part model without cost differencing step

Future Work

- Create a generalized framework using multi-disciplinary design optimization to minimize life-cycle cost of reusable space systems developed with an iterative reusable development program
- Cost estimation methodology used to calculate total program cost objective values for framework

ACKNOWLEDGMENTS

Thank you to my advisors Prof. Jeffrey Hoffman and Dr. Kevin Duda for their advice and support for this work.

Large Language Model Inference for Automated Cyber Red Actors

Sam Laney[1], Stephen Moskal [2], Una May O'Reilly [2], and Felipe Vilas Boas [3]

[1] Draper Scholar (MIT), [2] MIT CSAIL, [3] Draper

ABSTRACT

Large Language Models (LLMs) such as OpenAI's GPT 3.5 exhibit promise in their ability to plan, summarize, and infer for offensive cyber tasking. Our introductory research demonstrates the feasibility of LLMs as an engine for an adaptable, fully automated cyber attack planner. Leveraging off the shelf and open source tools, it can pivot from reconnaissance to exfiltration and all steps in between on vulnerable test machines in only a few crafted language model API calls.

INTRODUCTION

- Work in conjunction with MIT CSAIL's Anyscale Learning for All (ALFA) group for their proposal to **DARPA's *Cyber Agents for Security Testing and Learning Environments (CASTLE)***
- Language Models such as **GPT 3.5** are massive neural networks trained on billions of documents from the web. These models perform next word prediction but can be leveraged to perform other impressive tasks such as **summarization and inference.**
- Professional red teamers require **years of training** to gain the experience required to navigate and exploit a network. Substitution with an **automated, AI-based alternative** allows for network operators to **more effectively tune and harden their systems.**

METHODS

- We utilize a ***Planner-Actor-Reporter*** cycle in with the LLM creates a plan to achieve the goal *(exploit the system)*, distills an action from this plan *(execute x command)*, and reports the result *(summarization, success, state changes)* back to the planner. This repeats until the strategic goal has been achieved.

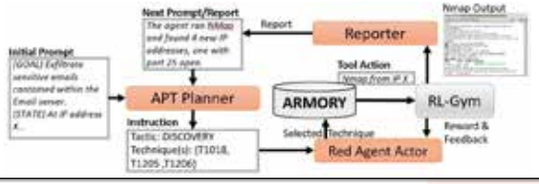

RESULTS

- Testing conducted within a virtualized Docker environment
- Red agent: Kali Linux
  - Standard OS for penetration testing
- Target: Metasploitable-2 container
  - Many vulnerable services
- Agent automatically transitions and infers between *strategic planning, reconnaissance, execution, translation, exploitation, and exfiltration* stages
- Successfully pinpoints an exploits vulnerabilities with **success rate >80%**

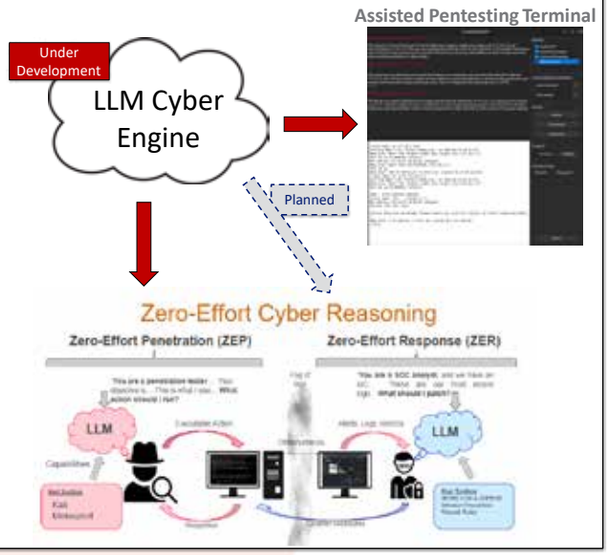

DISCUSSION

- Our initial prototypes confirm our hypothesis that, when paired with the right prompts, GPT-3.5 possesses the knowledge and reasoning capabilities to plan and execute the cyber kill chain.
- Current solutions rely on strict, rule-based formats that cannot adapt to or reason on new information, or rely a user to string together multiple automated tools.
- Future work includes:
  - Linking engine to the BRON cybersecurity database to enable lookup in addition to next word prediction
  - Data collection and testing against more hardened targets
  - Language model fine-tuning on cybersecurity-centric data
  - Automated Blue Agent that learns from and competes against Red Agent via Reinforcement Learning

CONCLUSIONS

- Our early-stage LLM-enabled cyber engine accomplishes multi-stage reasoning with chain-of-thought prompting to automate cyber-attack planning and execution.
- Enables more efficient penetration to harden defenses and train against a planned automated defensive agent.

ACKNOWLEDGMENTS OR REFS

- Work done in conjunction with MIT CSAIL's Anyscale Learning for All (ALFA) Group, led by Una-May O'Reilly
- Thank you to my advisor, Felipe Vilas-Boas (GCE8 Group Lead), and collaborator, Stephen Moskal (MIT Postdoc)

Integral Quadratic Constraints and Safety Certificates for Uncertainty Characterization and Control Safety Aware Filtering of Proximity Operations Between Satellites

Axel Garcia (Draper Scholar)[1], Richard Linares [1], Christopher Jewison [2]

[1]Massachusetts Institute of Technology, [2]Charles Stark Draper Laboratory

ABSTRACT

The main goal of this research is to create and validate a platform that performs feasibility studies of ensuring safety in proximity operations between satellites These studies incorporate analysis for the future generation of satellites The new capabilities include efficient maneuvers to perform proximity operations, while reducing the probability of collision between satellites and minimizing the propellant expenditure Two research areas, formal methods and robust optimization theory, are explored in this research with the goal of creating a platform that reduces uncertainty of system performance and updates control policies of satellite controllers to provide safety guarantees of satellite navigation at various altitudes The first area consists of exploring formal methods for safety assessment of various cases of satellite maneuvering, including rendezvous and docking, both in LEO and even cis lunar operations This approach involves the synthesis of control barrier functions, based on Lyapunov and control theory, to provide safety aware filtering for the control policies of satellites The second area to be explored in this research involves a framework based on robustness analysis theory to aid in the certification of spaceflight controllers This approach models first the satellite equations of motion (using a linear fractional transformation (on uncertainties and control laws, and then conducts robustness analysis on the system performance via applying the integral quadratic constraint (framework The novel contributions of this work focus on formulating mathematical safety guarantees, modeling controller output, and reducing uncertainty on system performance when designing fuel efficient maneuvers in a RPO mission

INTRODUCTION & METHOD

- The active satellite population is expanding rapidly and is expected to grow by an order of magnitude over the decade. This growth in space operations will require both increased spacecraft control autonomy, and techniques to provide robust safety guarantees for debris.
- Formal method technique (Lyapunov theory) is applied for safety assessment of various cases of satellite maneuvering.
- The propagation technique is validated by conducting robustness analysis on the system performance via applying an innovative integral quadratic constraint (IQC) reachability technique.

The Guidance, Navigation, Control (GN&C) is shown below.

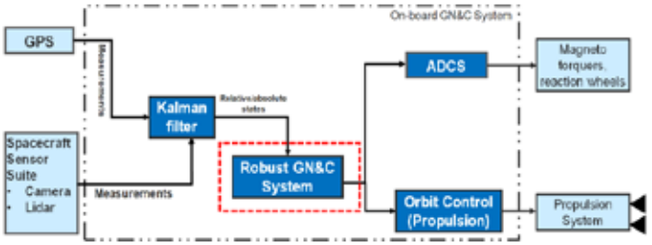

The Rendezvous, Proximity Operation (RPO) mission to be analyzed is the following:

Phases	Time Duration (seconds)
Direct Approach	[0-1,000]
Inspection mode	[1,200-1,700]
Positioning	[1,700-4,100]
Closest Approach	[4,100-5,700]
Retreat	[5,700-7,000]

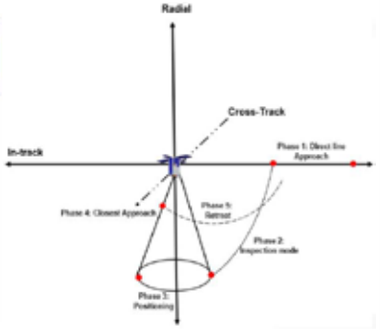

RESULTS & Discussion

The synthesis of the Control Barrier/Lyapunov Functions (CBF/CLF) are found using neural nets to develop a robust GN&C for the various RPO phases

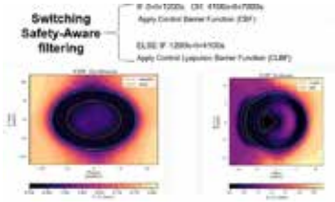

The direct approach phase is shown below. IQC is the green circle and shows the worst performance of the trajectory output at closest approach to debris. The IQC bounds does not do intersect the keep out zone specified in the mission.

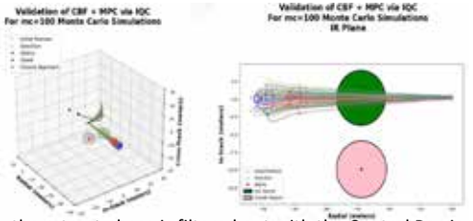

Similarly, the retreat phase is filtered out with the Control Barrier Function (CBF) so that trajectory never intersects the unsafe zone at closest approach to a debris object.

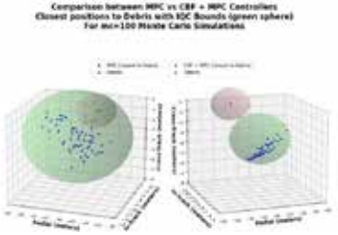

The inspection mode, positioning and closest approach phases can be filtered out with a Control Lyapunov Function (CLF) as shown below:

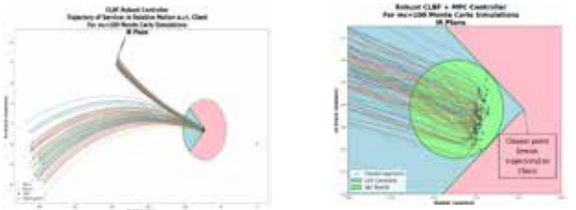

These results assumed perfect knowledge of the servicer state. Future work will incorporate measurements in the training of the CBF/CLF. The final trajectory adds 8% more fuel while ensuring safety guarantees for the whole duration of this RPO mission.

Collision Risk Assement in not included here due to space limitations

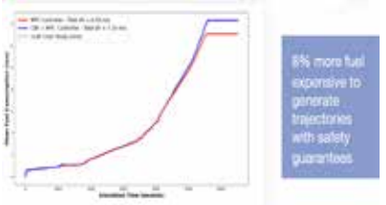

CONCLUSIONS

Reachability, control barrier functions and integral quadratic constraints provide a method to obtain strong safety guarantees for complex systems featuring the interaction of multiple subsystems with significant complexity. These methods, if applied correctly, can provide safety guarantees for interaction between multiple spacecraft controlled by different satellite operators and offer insight into collision avoidance algorithm control performance under different levels of information sharing.

ACKNOWLEDGMENTS OR REFS

I would like to thank the Draper Fellowship Program for providing funds to support this research.

MOON-BASED SENSOR PLACEMENT FOR CISLUNAR ORBIT DETERMINATION WITH EXCLUSION ZONES

Erin Shea (Draper Scholar)[1], Michele Carpenter[2], and Kenshiro Oguri[1]

[1]Purdue University, [2]The Charles Stark Draper Laboratory

ABSTRACT

Orbit determination in cislunar space is an area of interest within several communities where cislunar space domain awareness is critical to operations. A multi-gravity dynamics model is employed to attempt to accurately describe the state. Both the state estimate and error in the state are propagated using a combination of the dynamics model and physical measurements. Through an investigation of sensor placement, a location that provides the longest time in sight for the most optimal measurements can be determined and therefore enhance orbit determination performance.

INTRODUCTION

- Space domain awareness in cislunar space is a relatively novel field because legacy systems are not configured to handle the multi-body gravity field from the Earth and Moon. The Circular Restricted Three Body Problem is a method to model the dynamics of objects in this multi-body gravity field within a rotating reference frame, under several simplifying assumptions. The combination of this dynamics model and physical measurements allows for confidence in the state of an object in cislunar space. Measurements are taken from the far equatorial surface of the moon facing the L2 Lagrange point, the stationary point furthest from the Earth in the rotating frame. Areas that measurements are unable to be taken, such as range or field of regard limitations, are termed exclusion zones, and are handled only with the CR3BP dynamics model.

METHODS

- In order to incorporate measurements into the non-linear CR3BP dynamics model, and Extended Kalman Filter is used to propagate the mean and covariance of the state, through a time-step update loop.
- Measurements are simulated using an initial true state from the CR3BP model and adding Gaussian noise. Angle measurements are taken from the xz and xy planes within the rotating frame, and range measurements are taken from the sensor location on the moon, currently modeled as the equatorial surface facing the L2 Lagrange point.

RESULTS

- Below are the Extended Kalman Filter error plots, each with the error in blue and three standard deviations from the mean in red and yellow. These plots are for the state of the object- position and velocity, with the initial conditions $[x_0, y_0, z_0, v_{x0}, v_{y0}, v_{z0}]^{tr} = [1.149899, 0, -0.14667, 0, -0.21822, 0]^{tr}$

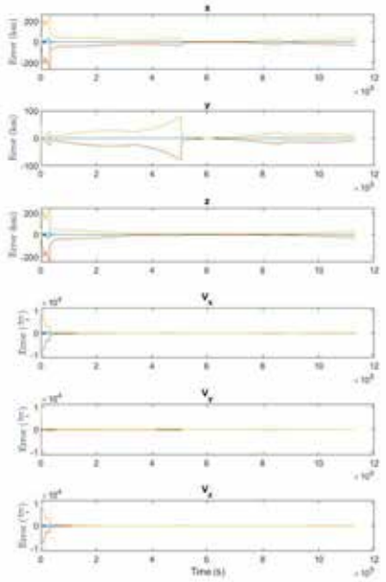

DISCUSSION

- Using a field of regard of 110 degrees, and a maximum range of the sensor of 8.3e4 km, both the position and velocity of the simulated object on the periodic L2 Halo orbit is confidently able to be determined well within 3 sigma bounds. Higher fidelity sensor and dynamics modeling will aim to more accurately describe the state and the associated error. Further sensor modeling will include detection threshold and conjunction and eclipse exclusion zones, while further dynamics modeling of the Earth-Moon-Sun system will include perturbations of each object to more accurately represent the dynamics of the system.

CONCLUSIONS

- These baseline results show the capacity of the EKF to confidently propagate the L2 Halo orbits using a moon based optical sensor. Further investigation into different sensor placements aim to produce smaller errors in state, and therefore inform moon-based sensor placement for orbit determination and cislunar space domain awareness

ACKNOWLEDGMENTS OR REFS

- T.A. Pavlak, “Trajectory Design and Orbit Maintenance Strategies in Multi-Body Dynamical Regimes” 2013, 9-17
- G.H.B. Byron D. Tapley, Bob E. Schutz, Statistical Orbit Determination, Elsevier Inc. 2004
- The views expressed in this article are those of the author and do not reflect the official policy or
- position of the United States Air Force, Department of Defense, or the U.S. Government

Rewritable Photonic Integrated Circuits

Forrest Miller[1,2], Sarah Geiger[3], and Arka Majumdar[1]

[1]University of Washington, [2]Draper Scholar, [3]The Charles Stark Draper Laboratory

ABSTRACT

Photonic Integrated Circuits (PICs) are becoming prevalent in applications such as communication, sensing, and quantum information [1]. However, prototyping these circuits requires an expensive nanofabrication facility that is ill suited to producing small batches of chips. Here, we proposeto exploit wide-bandgap non-volatile phase-change materials (PCMs) to create rewritable PICs. A PCM-based PIC can be written using a refractive index contrast induced by a nano-second pulsed laser, then the whole circuit can then be erased by heating, and a new circuit can be rewritten. We designed a dielectric-assisted PCM waveguide on top of a thin layer of wide-bandgap PCMs Sb_2S_3 and Sb_2Se_3 to minimize optical loss in the circuit. Furthermore, we analyzed the spatio-temporal laser pulse shape to write the PICs then experientially demonstrate such writing. Our proposed platform will enable low-cost PIC development and have a far-reaching impact on the rapid prototyping of PICs, validation of new designs, and photonic education.

INTRODUCTION

- Prototyping PIC designs requires an expensive nanofabrication facility that is ill-suited to making small batches of designs.
- Phase change materials (PCMs) demonstrate large changes in refractive index between their amorphous and crystalline molecular arrangements. These arrangements can be induced via heating and the refractive index contrast can guide light on chip.
- This work investigates if we can use PCMs as a cost effective testbench for passive PICs.

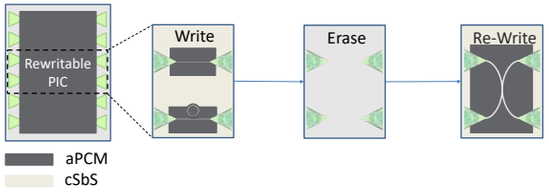

METHODS

- Via simulation: find a low loss material stack to guide the light on chip and find a laser pulse to heat the PCM layer.
- In experiment: build a confocal laser/microscope paired with a translation stage to laser write patterns on the chips.

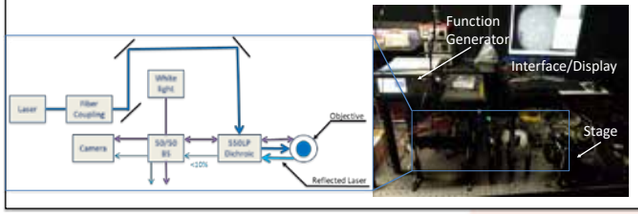

RESULTS

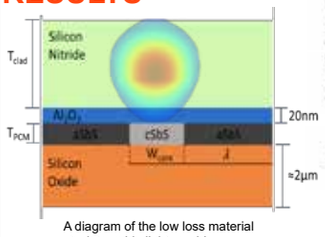

A diagram of the low loss material stack to guide light on chip.

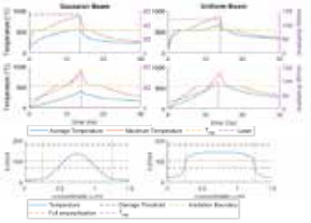

Thermal energy as a function of time and position for a variety of laser pulse types.

	73mW	70mW	68mW	66mW
6ns	Switched	Not Switched		
13ns	Switched	Switched	Not Switched	
20ns	Switched	Switched	Switched	Not Switched

Laser parameter table showing switching and non-switching irradiances.

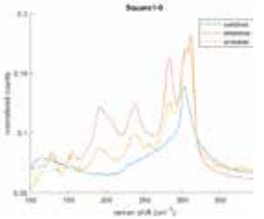

Typical Raman spectrum for a switched result.

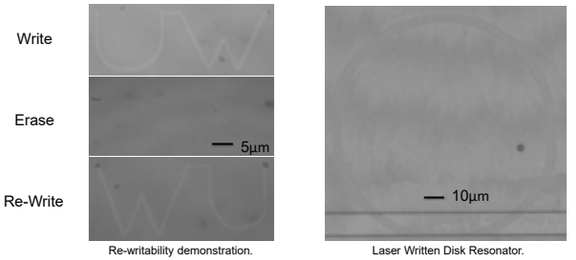

Re-writability demonstration.

Laser Written Disk Resonator.

DISCUSSION

- The material stack can guide light on chip with losses as low as 100 dB/cm using Sb_2S_3 or 86 dB/cm using Sb_2Se_3. This loss must be increased depending on the desired bend radii in the PIC.
- From simulation, we show that a nanosecond spatially gaussian and temporally rectangular laser pulse can reversibly switch a 15nm film of Sb_2S_3. We go on to experimentally demonstrate this via Raman spectrometry and by reversibly writing “UW” on the same area of a chip.
- The written disk resonator proves our setup can write patterns more than 100 μm in diameter without re-focusing. Depending on the resolution of the pattern, writing a 100 μm disk can be done in as little as 20 minutes.

CONCLUSIONS

- We show that laser writing PCM can be done inexpensively with a nanosecond laser and that such writing can make low loss waveguides. These factors offer a pathway to a rewritable PIC platform. Future work will involve writing devices and measuring their behavior.

ACKNOWLEDGMENTS OR REFS

- We would like to acknowledge support from the Draper Scholar program, the QPGA team at Draper, the University of Washington NOISE lab, and funding from an NSF-YFA award.
- [1] F. Miller, R. Chen, J. E. Froech, H. Rarick, S. Geiger, and A. Majumdar, ‘Rewritable Photonic Integrated Circuits Using Dielectric-assisted Phase-change Material Waveguides’. arXiv, 2023.

Seeking Computational Efficiency While Optimizing Formation Flying Trajectories in the Vicinity of Lagrange Points

Hailee Hettrick (Draper Scholar)[1,2], Begum Cannataro[2], and David W. Miller[1]

[1]Massachusetts Institute of Technology, [2]Draper

ABSTRACT

To consider formation flying trajectories in the vicinity of Lagrange points of two spacecraft with different naturally occurring dynamics, approximate analytical solutions from perturbation theory may be used to evaluate several trajectories in a computationally efficient manner. For a space telescope mission, line-of-sight requirements for the two spacecraft provide constraints on their positions; additionally, the incident light from bright celestial bodies further constrains the possible spacecraft positions.

INTRODUCTION

- A proposed next-gen space telescope, Habitable Exoplanet Observatory (HabEx), requires the use of two spacecraft in formation flight about Sun-Earth L_2 and will image several distant stars' exoplanets.
- Previous work on HabEx's trajectories have either failed to consider the observation time required or did not use dynamical systems theory (DST) for both spacecraft.
- The goal of this research is to optimize the mission as follows: (1) during the retargeting phase, efficiently slew the formation line-of-sight (LOS) using DST, (2) during the imaging phase, hold LOS to adhere to imaging requirements by using solar radiation pressure DST, and (3) employ approximate analytical techniques when seeking the formation's optimal path.

METHODS

- Formation flight modeling: CR3BP and CR3BP with solar radiation pressure (SRP), approximate analytical solutions determined via Lindstedt-Poincaré method
- Keepout constraints → yields set of positions with desired orbit characteristics at every time step of mission for every target star; optimize mission path using these positions

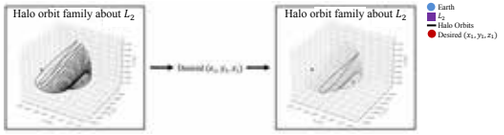

RESULTS

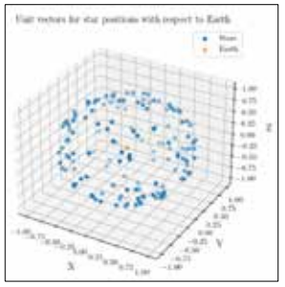

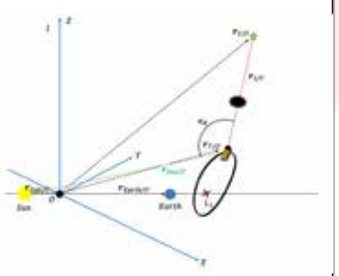

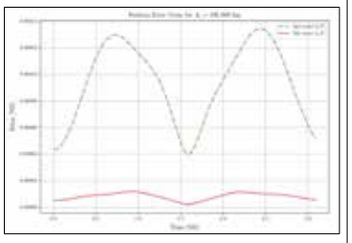

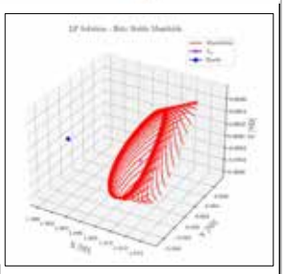

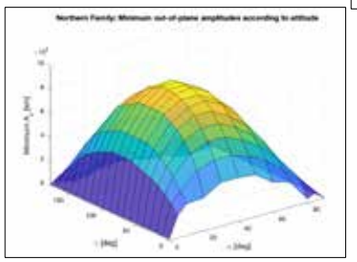

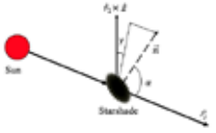

DISCUSSION

- Approximate analytical solutions for the CR3BP are complete; solutions for CR3BP with SRP in progress
  - Halo, Lissajous, Vertical, Lyapunov and corresponding manifolds
- Using keepout constraints to find all possible positions in space for the formation at every point in time enables computational efficiency in determining possible trajectories
- Given a position in the regime of CR3BP, a method using the approximate solutions determines the characteristic Halo orbit that position coincides with
- Once the CR3BP with SRP solutions are complete, the above can be used to find the optimal mission path.

CONCLUSIONS

- Approximate analytical solutions and keepout constraints corresponding to target stars drive the trajectory options to enable computational efficiency and fuel optimality
- The next step focuses on modeling the starshade via CR3BP with SRP

ACKNOWLEDGMENTS

- Thank you to my officemate, Alex, for his feedback regarding CR3BP.
- Thank you to my advisors, Dave and Begum, for their guidance and support.

Porous Silicon Nitride Ceramics for RF Radomes Fabricated by Slip Casting

Averyonna Kimery (Draper Scholar)[1,2], Prof. Carlos Martinez[1], and Dr. Tirunelveli S. Sriram[2], Prof. Rodney Trice[1]

[1]Purdue University –Materials Engineering, [2]Draper

ABSTRACT

Radomes protect antennas from the harsh environment encountered when flying at hypersonic speeds. Radome materials must have a low dielectric constant and loss to minimize reflection and attenuation of GHz radar waves. Silicon nitride is being considered as a radome material due its suitable mechanical properties along with the low dielectric constant and dielectric loss. Porosity is introduced to further reduce the dielectric constant. The fabrication of porous silicon nitride using various methods, including slip casting with pore forming agents and effect of sintering aids is explored.

MATERIAL PROPERTY REQUIREMENTS

Radomes must protect the antenna to houses from harsh environments as well as allow electromagnetic waves to be received and transmitted by the antenna with minimal interference.[1] The X, K_u, and K_a (8-40 GHz) bands are of interest.[2] Silicon nitride has become of increasing interest for radome applications because of its favorable mechanical and thermal properties. As well as for its suitable dielectric properties with a dielectric constant of 7.9 for beta silicon nitride (β-Si_3N_4[1]) which can be further reduced with incorporation of porosity.

Table 1. Radome material property requirments[1].

Properties	Requirement
Service temperature	Up to 1400°C
Dielectric constant (ε)	<9.0 (5.0 preferred)
Temperature variation of dielectric constant to 1260°C	<7.0%
Loss tangent (δ) to 1260°C	<0.1
Bending strength (4-point)	>35 MPa

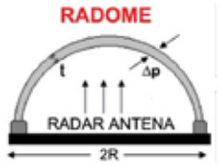

Figure 1. Typical radome design.[3]

FABRICATION OF POROUS SILICON NITRIDE

The relation of a porous body to a fully dense body is given by: $\varepsilon_{porous} = \varepsilon_{dense}^{(1-P)}$ where *P* is the pore fraction. From this equation it is seen that increasing porosity will decrease the dielectric constant. Features <1/10th of the wavelength of interest will not cause scattering of the incoming signal.

At a frequency of 40 GHz the corresponding wavelength is 7.5 mm therefore features or pores need to be maintained below 750 µm. Slip casting is a relatively simple and fast processing method that allows for fabrication of complex and large shapes. An optimized aqueous silicon nitride suspension was developed to have low viscosity and high stability which are necessary for slip casting. The optimized suspension was determined to be 30 vol% solids loading, 0.5 wt% dispersant (PEI), and pH 7. Using the optimized suspension large parts were able to be slip cast crack free with a sintered size of ~80 mm and 5 mm thick. Two different methods to incorporate porosity to the slip cast suspensions were used.

Figure 2. Sintered slip cast Si_3N_4 sample.

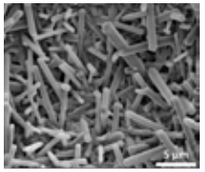

Figure 3. Beta grains formed during sintering.

RESULTS Method #1: Fugitive Additive – Carbon Black

6 wt% yttria and 2 wt% alumina were used as sintering aids in the silicon nitride suspension. A sample made from the silicon nitride suspension has a density of 92% and an average flexural strength of 590 ± 90 MPa when sintered at 1850°C for 2 hours. β-Si_3N_4 and Y_2SiO_5 (glassy phase) are formed. To increase the porosity of a fugitive additive, carbon black (CB), is used. To incorporate the fugitive a second suspension of CB (15 µm average diameter) was made at 30 vol% solids loading, 5.0 wt% PEI, and pH 7. The two suspensions were mixed at desired ratios and cast. After casting the CB is burned out at 1000°C. Pores remain in the place of the removed CB particles.

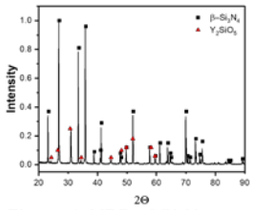

Figure 4. XRD of Si_3N_4 sample.

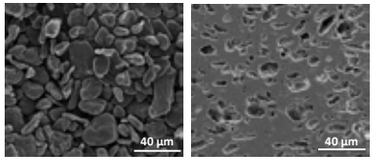

Figure 5-6. SEM images of the CB powder and resulting porosity of a sample made from 45 vol% CB suspension.

The dielectric constant and loss tangent of two samples, one was 92% dense and the other 83% dense, were measured by APL[4] from 20-40 GHz. The measured dielectric constants compare well to those expected based on the previously shown equation for a porous body.

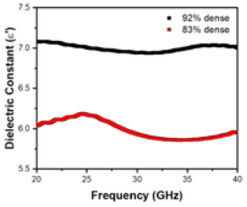

Figure 7. Dielectric constant from 20-40 GHz.[3]

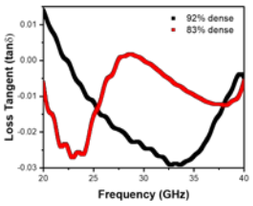

Figure 8. Loss tangent from 20-40 GHz.[3]

A cast sample made from 45 vol% CB suspension and 55 vol% silicon nitride suspension has a sintered porosity of 30.1% and has an expected dielectric constant of 4.3 (awaiting testing results).

Method #2: Ytterbium Oxide (Yb_2O_3) and Partial Sintering

Ytterbium oxide has a high melting point and high viscosity resulting glassy phase ($Yb_4Si_2O_7N_2$) when sintering with silicon nitride. Yb_2O_3 combined with modification of sintering temperature creates porosity.

Samples with 5 wt% Yb_2O_3 sintered at temperatures between 1700-1850°C were studied with resulting porosities from 21-31%. Complete beta formation occurs at and above 1800°C. Dielectric constant and loss will be measured for this materials and the expected dielectric constants range from 3.5-5.2.

Table 2. Yb_2O_3 sample properties.

Sintering Temperature (°C)	Porosity (%)	Expected Dielectric Constant (ε)	Average Flexural Strength (MPa)
1700	31.6	3.48	290 ± 30
1750	27.1	4.06	144 ± 17
1800	27.2	4.54	311 ± 32
1850	21.1	5.16	474 ± 38

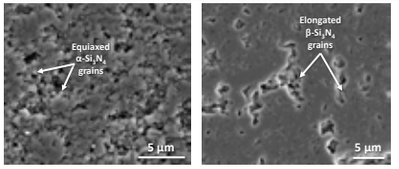

Figure 9-10. SEM images of resulting porosity in the 1700°C and 1850°C sample.

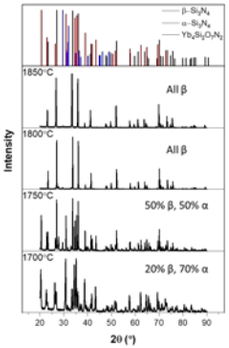

Figure 11. XRD of samples from Table 2 and reference peaks (top).

CONCLUSIONS AND FUTURE WORK

Slip casting of silicon nitride allows for the fabrication of large samples that can be tested at 20-40 GHz. Using fugitive additives and sintering aids to create porosity allows for tailoring of properties for optimal performance of the radar antenna while balancing the mechanical properties. Dielectric measurements of samples fabricated by both methods will be collected for room temperature up to 1000°C. Flexural strength and elastic modulus measurements up to 1500°C will also be completed. Using the data collected from these samples layer thickness can be configured to create a sandwich radome wall design with the different layers being sequentially cast from the selected suspensions.

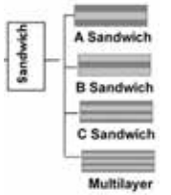

Figure 12. Radome sandwich wall designs.[3]

ACKNOWLEDGMENTS AND REFERENCES

1. Saeedi Heydari, M., Ghezavati, J., Abbasgholipour, M. & Mohammadi Alasti, B. Various types of ceramics used in radome: A review. Sci. Iran. 24, 1136–1147 (2017).
2. Radar Frequency Bands. American Institute of Aeronautics and Astronautics.
3. Nag, A., Rao, R. R., & Panda, P. K. (2021). High temperature ceramic radomes (HTCR) – A review. In *Ceramics International*.
4. Dielectric measurements completed by Collin McClain and Keith Caruso at Johns Hopkins Applied Physics Laboratory.
5. Hostaša, J., Silvestroni, L., Piancastelli, A., Sciti, D., Martino, D. di, & Esposito, L. (2012). Slip Casting of a Si3N4-Based System. *International Journal of Applied Ceramic Technology*, *9*(2), 246–258

Incorporating Correlation Uncertainty into High-Dimensional Gaussian Mixture Models

Charlie Harrington (Draper Scholar)[1, 2]

[1]Draper Laboratory, [2]Harvard University

ABSTRACT

Modeling can be particularly challenging in instances where jointly observed data is unavailable. One solution is Gaussian Mixture Models (GMMs), which can provide an approximated joint model based on available data and correlation information gathered from existing literature. This work focuses on incorporating the uncertainty of the correlation information into the model using an ensemble of GMMs. We suggest two approaches: (1) fit an ensemble to values sampled from correlation distributions, and (2) fit one model to mean correlations and generate ensemble by perturbing component correlations. We validate our overall methodology, observe predicted outcomes, and discuss areas of improvement to increase accuracy and efficiency.

INTRODUCTION

- Without jointly-observed data, we can still build using marginal data and information about variable correlations
- Gaussian Mixture Models (GMMs) can be used in these underdetermined problems
- Literature on variable relationships yields different results, providing prediction informed by average values fails to capture uncertainty and variability
- This work is in contribution to a project building a tool for military leaders to assess future performance outcomes of soldiers based on environmental factors
- We aim to incorporate uncertainty about effect sizes between variables into our models to provide better informed predictions

METHODS

- We use a bagging approach: build an ensemble of GMMs such that the correlations of the ensemble are distributed according to distribution found in literature
- Our work investigates two approaches for doing so:

1) Randomly generate effect-size matrix from distributions and fit models to them.
2) Fit one model to mean effect size, then generate ensemble by perturbing component correlations – involves sampling high-dimensional probability distribution, requiring sampling methods (e.g., Markov Chain Monte Carlo)

RESULTS AND DISCUSSION

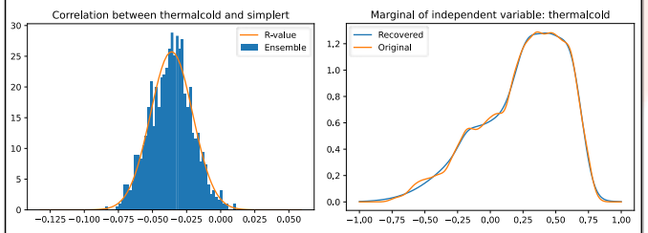

- Results on left validate overall methodology: an ensemble can capture variability in correlation information
- Chart on right demonstrates predicted (and desired) outcome, recovered marginals are smoother
- This ensemble of 1,000 models took ~70 compute hours to build, motivating need for more efficient method to make use more practical

- Chart on right demonstrates challenges in Method 2 sampling coming from constraints on parameters
- More sophisticated techniques may be necessary to explore high-dimensional manifold

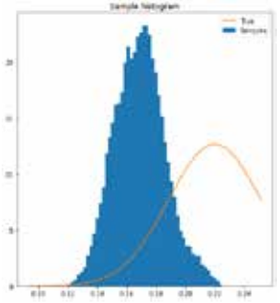

CONCLUSIONS

- Top-level methodology has been verified and produces predicted/desired “smoothening” behaviors
- Further work is needed to make its use more practical, building ensemble currently uses lots of time and memory
- Remainder of research will focus on more sophisticated sampling techniques (e.g., Hamiltonian Monte Carlo) or deep learning methods (e.g., normalizing flows).
- Our approach to incorporating uncertainty in relationships between variables yields predictions more representative of nuanced problem landscape
- When leaders use the tool below, they can know that it is informed by as much knowledge as possible

ACKNOWLEDGMENTS

Thank you to Alex Young and Louis Kim for their guidance, and to Draper Labs and the Tufts Center for Applied Brain Sciences for the opportunity to conduct this work.

Predicting Component Failures from Waivers

Frank Rossi [1], Anthony Palladino [2], Declan Knieriem [2], and Andrea Webb [2]

[1]Draper Scholar, Northeastern University, [2] Draper

ABSTRACT

A certain mechanical component and its parts are evaluated before being deployed into operational use When a component test is outside of the specified tolerance, but there is a valid reason to still use the unit, the evaluator follows a formal process to request a waiver or deviation The official forms in that waiver process contain natural language text describing the issue We aim to develop an approach to estimate which individual units may fail using only the natural language contents of the waiver forms Preliminary results show a need for further data exploration to understand latent structures in the waiver contents that can increase predictive capabilities

INTRODUCTION

- Predicting the failure of a mechanical component can be done by running several tests on the component and analyzing the numerical results. However, these predictions are far from perfect and may be enhanced by incorporating additional information about each unit into the failure predictions.
- Each component unit contains a set of waivers that describe in natural language any original requirements that have been deviated from during their construction.
- The goal of this project is to determine the extent to which the content of these waivers can predict the eventual failures of the units.

METHODS

- The dataset consists of 990 units labeled by serial number and fail/no fail, each with several waivers. Waivers take on multiple forms, each with up to 50 separate boxed-sections along with appendices. These sections are mostly similar across waiver forms but not completely.
- Waivers are translated to text documents by using OpenCV to detect the boundaries of each section and using pyTesseract OCR to convert the image to text.
- The current method of feature extraction is Bag-of-Words and Term Frequency – Inverse Document Frequency..
- In BoW, each component is represented as the set of words in its waivers. In TF-IDF, this feature vector is enhanced by emphasizing words that occur rarely in the dataset and de-emphasizing words that occur frequently in the data.
- The current goal is identifying any latent structure in the component waivers to allow for better feature extraction.

RESULTS

- Failure Prediction results are not yet complete. Early experiments using a simple Bag-of-Words model for each component never produced an F1-score above 0.5 across the whole dataset, necessitating a different method of feature extraction.
- Data Exploration results show potential for better-crafted features using the individual sections of waivers. Waivers take on multiple forms but share the most critical sections, such as the “Reason for Change” section, which is a narrative of why the waiver should be used.
- Furthermore, the same waivers and groups of waivers can often be found across multiple components. We identified only 190 unique waivers that are associated with one or more of the 990 units.

Two different waiver formats. Computer Vision and OCR must be combined to identify and extract the same section from each different format, while excluding irrelevant/noisy sections

DISCUSSION

- Most research using NLP for failure prediction uses software logging messages as data. No other papers have been found which use waiver contents
- Many of the difficulties in the dataset are logistical/processing difficulties, not classification difficulties. Data sourced as images instead of text, various waiver formats, and the inclusion of many extraneous sections in the waivers with little informative substance along with other idiosyncrasies in the data make feature extraction tedious.
- The main takeaways of this work will be the abilities of NLP techniques to capture latent information in the data even with short texts, unbalanced classes, and a small dataset, along with the usefulness of the failure predictions created for the component program.

CONCLUSIONS

- Messy data can be extraordinarily difficult to work with. The next steps are to extract common sections from every waiver and judge their predictive capabilities

ACKNOWLEDGMENTS OR REFS

- Thanks to Tesseract OCR and OpenCV for their high-quality open-source software.

This material is based upon work supported by the Strategic Systems Programs under Contract No. N0003022C6002. Any opinions, findings and conclusions or recommendations expressed in this material are those of the author(s) and do not necessarily reflect the views of Strategic Systems Programs.

Northeastern University

DRAPER

Remote Sensing and Integrated Systems Frameworks for Flood Management Decision Support in Indonesia

Seamus Lombardo[1,3], Steven Israel[2], Afreen Siddiqi[1] Leia Stiring[4], Katya Arquilla[1] and Oli de Weck[1]

[1]Massachussetts Institute of Technology, [2]Draper, [3]Draper Scholar, [4]University of Michigan

ABSTRACT

Decision Support Systems (DSS) can aid leaders confronting complex environmental challenges. A process of systems analysis of interviews to understand stakeholder objectives, satellite data to analyze environmental trends, integrated modeling towards actionable insights, and user studies to evaluate DSS utility, is employed to address previous gaps in DSS development. Novel insights and positive feedback are obtained by users in Indonesia. The DSS design process can be further applied to environmental management varying from indigenous forests to protection of DoD installations from environmental threats.

INTRODUCTION

- Local leaders in Pekalongan, Indonesia face challenging decisions regarding how and where to implement flood mitigation interventions (Marfai, 2014)
- Decision support systems (DSS) can supplement decision making, but often are not used by leaders due to lack of stakeholder engagement in DSS design (Diez *et al*., 2009)

Severe coastal flooding and land subsidence affect the natural ecosystem, economy, and public health of Pekalongan City

METHODS

- Systems analysis of stakeholder interviews guides DSS development and the selection of remote sensing analyses and other local economic and infrastructure datasets
- Evaluations of DSS prototype by end-user stakeholders identifies positive areas and areas for improvement

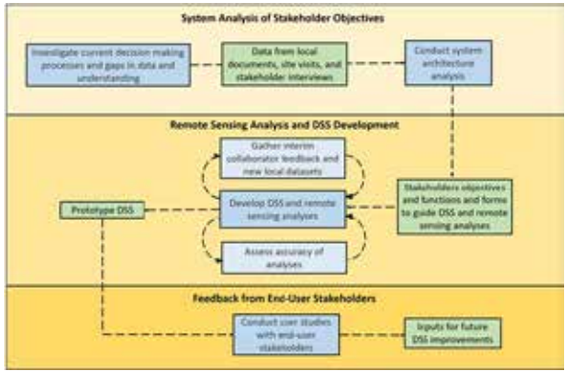

Phases of collaboration to address gaps in stakeholder engagement and increase satellite data use

SYSTEMS ANALYSIS OF STAKEHOLDER OBJECTIVES

- Stakeholder interviews are used to identify objectives, and translate them into functions and forms via system architecture framework (Kazansky *et al*., 2016)

Stakeholder Interviews for Pekalongan

Stakeholder Category	Stakeholder Name	Stakeholder Organization
Academic	Dr. Muhammad Helmi	CoREM, Universitas Dipongoro
	Dr. Joga D. Setiawan	
	Dr. Anindya Wirasatriya	
Local Government	Ibu Anita Heru	Pekalongan City Regional Development and Planning Agency
	Mr. Slamet Miftakhudin	
NGO	Mr. Arif Gandapurnama	Mercy Corps
	Ibu Henni Hendarti	Deltares
	Mr. Aji Abimayu	Kemitraan

SATELLITE REMOTE SENSING

- System architecture framework outputs target satellite remote sensing analyses to stakeholder objectives

Permanent water – extent and year water became permanent (2000 – 2021)

- Areas of increasing permanent water can identify areas of risk for leaders

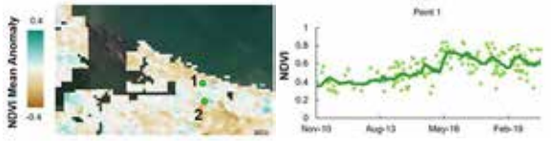

NDVI-trends in areas classified as mangroves (2010-2021)

- Mangrove degradation can be identified and mangroves can be evaluated for flood mitigation

INTEGRATED INFORMATION FOR INSIGHTS

- Environment-vulnerability-decision-technology (EVDT) modeling framework is used to add local socioeconomic data alongside environmental information (Reid *et al*., 2019)
- Local infrastructure and land use information integrated alongside satellite-based flood analyses aids decisionmakers in identifying areas of flood risk and evaluating interventions

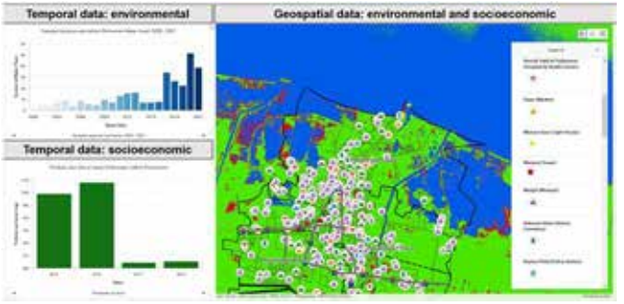

DSS UI incorporating satellite remote sensing analyses alongside local socioeconomic information

USER STUDIES TO MAXIMIZE UTILITY

- Feedback was gathered from users to evaluate DSS prototype
- Positive ratings and desire to institutionalize indicate DSS utility

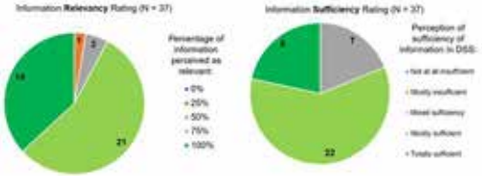

Survey results on DSS prototype from stakeholder evaluation sessions

CONCLUSIONS

- Systems analysis of interviews aids in DSS development
- The spatial coverage and temporal consistency of satellite data provides environmental insights useful to decision makers
- EVDT integrated modeling framework facilitates inclusion of local data for additional context and actionable insights

Physiological Indicators of Situation Awareness

Kieran J. Smith[1,2], Tristan C. Endsley [3], and Torin K. Clark [1]

[1]University of Colorado Boulder, [2] Draper Scholar, The Charles Stark Draper Laboratory, Inc., [3] The Charles Stark Draper Laboratory, Inc.

ABSTRACT

Could these metrics estimate objective measurements of operator perception, projection, and comprehension?

Individual psychophysiological, neurophysiological, and behavioral metrics correlate with various measures of Situation Awareness

(Zhang et al., 2020).

INTRODUCTION

In human-autonomy teams, autonomous systems benefit from access to internal human states (Carroll et al., 2020). Situation Awareness (SA), one of these internal states, is critical for safety (Endsley 1995) but not easily observable. SA includes an operator's perception of elements in the environment, comprehension of those elements, and projection of the current state into the future (Endsley, 1988).

1. **Perception**
2. **Comprehension**
3. **Projection**

No prior work has used a full suite of physiological signals to estimate objective measures of SA. This work will incorporate physiological features novel to SA literature.

METHODS

Participants (N=3) completed 12 trials of a modified Multi-Attribute Task Battery II simulation (Santiago-Espada et al., 2011) followed by an SA assessment targeting all 3 levels of SA, all while wearing a suite of physiological sensors.

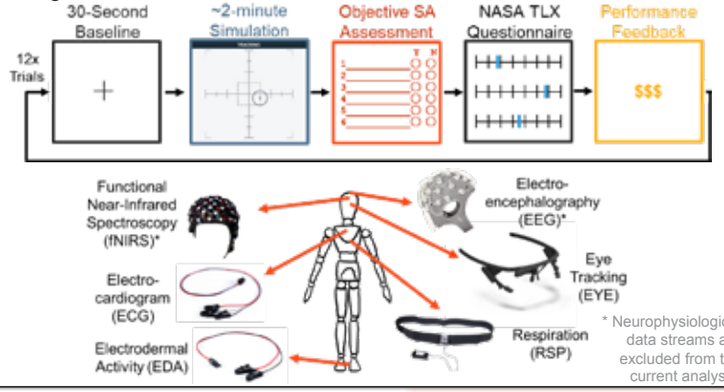

* Neurophysiological data streams are excluded from the current analysis.

RESULTS

Single-feature Spearman-Rank correlations were calculated between each physiological feature and each SA Score: perception, comprehension, projection (out of 6), and a total score (out of 18).

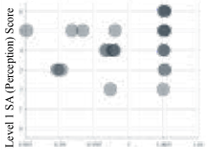

r	0.45
r^2	0.20
p	0.006

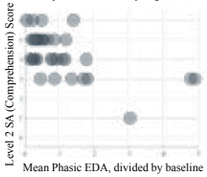

r	-0.50
r^2	0.25
p	0.002

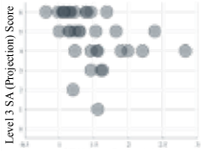

r	-0.58
r^2	0.34
p	0.0002

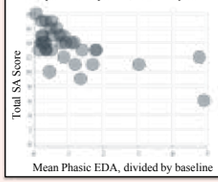

r	-0.55
r^2	0.30
p	0.0005

Regressions using combinations of features were investigated using LASSO analysis, an automated process for down-selecting the most important features from a large feature set.

Models that performed similarly across leave-one-subject and -trial out cross-validations are presented here.

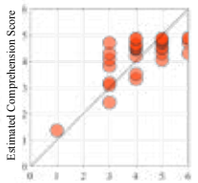

r^2	0.50
r^2_{adj}	0.49
Q^2_{subj}	0.53
Q^2_{trial}	0.48

Predictor: Minimum Tonic EDA (Raw Baseline):Area under SCRs (Last 20, Divided by Baseline)

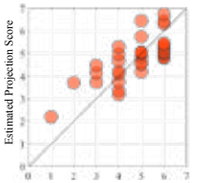

r^2	0.54
r^2_{adj}	0.51
Q^2_{subj}	0.52
Q^2_{trial}	0.47

Predictors: Mean Phasic Skin Conductance:RSP Rate & Area under SCRs:RSP Rate

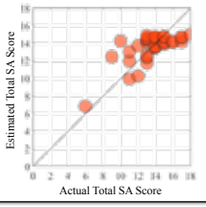

r^2	0.51
r^2_{adj}	0.48
Q^2_{subj}	0.48
Q^2_{trial}	0.42

Predictor: Max Phasic EDA (Final, Divided by 1st Baseline): #SCRs (Baseline, less 1st Baseline)

DISCUSSION

Single correlates explained over a third of the variance in SA scores

- Prior work has found a negative correlation between SA and heart-rate variability (HRV; RMSSD, not pNN50).
- Prior work has found positive correlations between SA and total EDA (not phasic EDA).

Single-predictor models explained over half of the variance in SA Scores. However, more work is needed to provide reliable estimates of human operator SA to an autonomous teammate.

CONCLUSIONS

Physiological signals provide a promising avenue to understand and estimate operator SA.

Future work is in progress to recruit additional participants, analyze neurophysiological data, and incorporate cognition-informed features into more advanced models.

ACKNOWLEDGMENTS

This material is based upon work supported by the National Science Foundation Graduate Research Fellowship and a Draper Scholarship

Assessing the Impact of Non-Pharmaceutical Interventions on Consumer Mobility Patterns and COVID-19 in the US

Joseph Zuccarelli (Draper Scholar)[1,2], Laura Seaman[1], Kevin Rader[2], Kosuke Imai[2]

[1]The Charles Stark Draper Laboratory, Inc., [2]Harvard University

ABSTRACT

The COVID-19 pandemic markedly changed consumer mobility patterns. In this project, we investigate these changes as they relate to the initial spread of the disease at the county-level within two states—MA and MI. Specifically, we use mixed effects models to quantify (1) the relationship between government non-pharmaceutical interventions (NPIs) on point-of-sale (POS) transactions, and (2) the relationship between subsequent changes in POS transactions and COVID-19 cases. Our analysis reveals a significant negative association between NPI stringency and POS transaction rates, and a significant positive association between changes in POS transaction rates and COVID-19 case growth rates.

INTRODUCTION

Research Questions

- How did early NPIs affect consumer mobility patterns?
- How did changes in consumer mobility patterns affect the initial spread of COVID-19?

Literature Review

- Methods: Event Study, Interrupted Time Series
- Data: NPIs, Mobility Measures (Google & SafeGraph), COVID-19 Cases & Deaths (State & County-Level)
- Results: Early NPIs were effective against COVID-19

METHODS

Data (MA & MI Daily County-Level Observations)

- NPI Stringency Levels, POS Transaction Counts, COVID-19 Case & Testing Counts (01JAN2020 - 30MAY2020)

Mobility Modeling

- Negative Binomial Mixed Models (Autoregressive Covariance Structure)

$$\log\left(\frac{1000 \times transactions_{ij}}{population_{ij}}\right) = \beta_0 + \beta NPI_{ij} + \beta weekend_{ij} + \gamma_{0j}$$
$$i \equiv date\,;\; j \equiv county$$

COVID-19 Modeling

- Linear Mixed Models (Autoregressive Covariance Structure)

$$case\ growth\ rate_{ij} = \beta_0 + \beta_1 \Delta transactions_{ij} + \beta_2 test\ rate_{ij} + \beta_3 weekend_{ij} + \gamma_{0j}$$
$$i \equiv date\,;\; j \equiv county$$

$\Delta transactions$: Lagged % change vs. pre-pandemic baseline

MOBILITY MODELING

Results

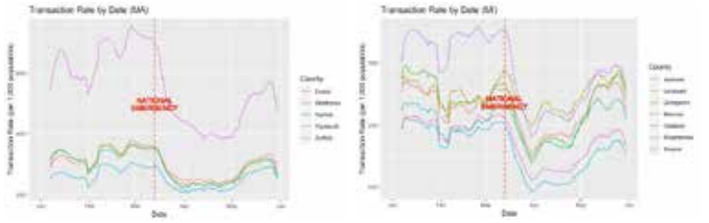

Mobility Modeling Results (MA)

NPI	Fixed Effects	e^{β}	95% CI	*p*-value
National Emergency	Intercept	353.28	(279.49,446.56)	0.00***
	Effective	**0.86**	**(0.80,0.93)**	**0.00***
	Weekend	0.87	(0.86,0.88)	0.00***
Workplace Closing	Intercept	345.31	(273.19,436.47)	0.00***
	Required (all)	**0.89**	**(0.82,0.96)**	**0.00****
	Weekend	0.87	(0.85,0.88)	0.00***
Gathering Restrictions	Intercept	371.96	(294.58,469.66)	0.00***
	Restrict 101-1,000	**0.92**	**(0.86,0.99)**	**0.03***
	Restrict 11-100	**0.80**	**(0.74,0.86)**	**0.00*****
	Restrict < 10	**0.77**	**(0.71,0.84)**	**0.00*****
	Weekend	0.87	(0.85,0.88)	0.00***
Stay-at-Home Reqs.	Intercept	347.44	(274.89,439.13)	0.00***
	Recommended	**0.88**	**(0.81,0.95)**	**0.00****
	Weekend	0.87	(0.85,0.88)	0.00***

Mobility Modeling Results (MI)

NPI	Fixed Effects	e^{β}	95% CI	*p*-value
National Emergency	Intercept	237.06	(205.53,273.43)	0.00***
	Effective	**0.89**	**(0.83,0.96)**	**0.00****
	Weekend	0.82	(0.81,0.83)	0.00***
Workplace Closing	Intercept	254.76	(221.02,293.65)	0.00***
	Required (some)	**0.84**	**(0.79,0.90)**	**0.00*****
	Required (all)	**0.68**	**(0.64,0.73)**	**0.00*****
	Weekend	0.81	(0.80,0.82)	0.00***
Gathering Restrictions	Intercept	284.98	(242.80,334.49)	0.00***
	Restrict 101-1,000	**0.94**	**(0.88,1.01)**	**0.08****
	Restrict 11-100	**0.79**	**(0.72,0.86)**	**0.00*****
	Restrict < 10	**0.64**	**(0.57,0.71)**	**0.00*****
	Weekend	0.82	(0.80,0.83)	0.00***
Stay-at-Home Reqs.	Intercept	239.41	(207.41,276.36)	0.00***
	Recommended	**0.97**	**(0.90,1.03)**	**0.32**
	Required	**0.82**	**(0.76,0.89)**	**0.00*****
	Weekend	0.82	(0.80,0.83)	0.00***

Discussion

- Each NPI is associated with a significant decrease in POS transactions (e^{β} NPI fixed effect **coefficients < 1**)
- As the stringency of NPIs increases, POS transactions decrease
- Results confirm previous findings that early NPIs reduced human mobility (Mendez-Brito *et al.*, 2021)
- Limitations: Generalizability, confounding, spillover effects

COVID-19 MODELING

Results

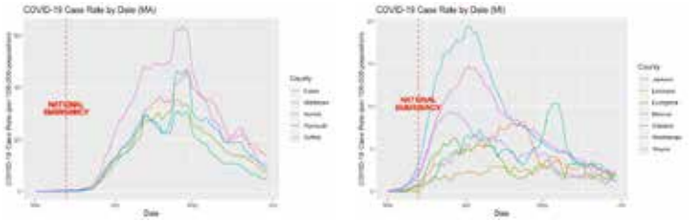

COVID-19 Modeling Results (MA)

Lag Period	Fixed Effects	β	95% CI	*p*-value
08 Days	Intercept	31.83	(22.87,40.79)	0.00***
	Δ Transactions	**0.17**	**(-0.06,0.40)**	**0.15**
	Test Rate	-10.57	(-15.67,-5.48)	0.00***
	Weekend	-33.10	(-42.35,-23.85)	0.00***
10 Days	Intercept	31.39	(22.61,40.17)	0.00***
	Δ Transactions	**0.23**	**(-0.01,0.47)**	**0.06**
	Test Rate	-9.57	(-14.89,-4.26)	0.00***
	Weekend	-32.61	(-41.86,-23.36)	0.00***
12 Days	Intercept	30.46	(21.77,39.15)	0.00***
	Δ Transactions	**0.30**	**(0.06,0.54)**	**0.02***
	Test Rate	-8.25	(-13.81,-2.68)	0.00***
	Weekend	-31.42	(-40.76,-22.07)	0.00***
14 Days	Intercept	28.47	(19.70,37.24)	0.00***
	Δ Transactions	**0.39**	**(0.13,0.65)**	**0.00****
	Test Rate	-6.08	(-12.17,0.01)	0.05*
	Weekend	-29.49	(-39.06,-19.93)	0.00***

COVID-19 Modeling Results (MI)

Lag Period	Fixed Effects	β	95% CI	*p*-value
08 Days	Intercept	18.22	(10.36,26.08)	0.00***
	Δ Transactions	**0.19**	**(0.01,0.37)**	**0.03***
	Test Rate	-10.30	(-16.12,-4.47)	0.00***
	Weekend	-23.02	(-31.83,-14.21)	0.00***
10 Days	Intercept	16.54	(8.98,24.10)	0.00***
	Δ Transactions	**0.14**	**(-0.04,0.32)**	**0.12**
	Test Rate	-9.50	(-15.26,-3.75)	0.00***
	Weekend	-22.43	(-31.22,-13.64)	0.00***
12 Days	Intercept	15.94	(8.61,23.26)	0.00***
	Δ Transactions	**0.13**	**(-0.05,0.31)**	**0.15**
	Test Rate	-9.27	(-15.02,-3.52)	0.00***
	Weekend	-21.62	(-30.44,-12.80)	0.00***
14 Days	Intercept	15.32	(7.98,22.65)	0.00***
	Δ Transactions	**0.09**	**(-0.08,0.27)**	**0.31**
	Test Rate	-9.03	(-14.79,-3.27)	0.00***
	Weekend	-22.46	(-31.29,-13.64)	0.00***

Discussion

- Significant positive association between lagged Δ POS transactions and case growth rates (β Δtransactions fixed effect **coefficients > 0**)
- Optimal lag period undefined (MA ~ 12-14 days, MI ~ 8-10 days)
- Previous studies found stronger associations between human mobility and case growth rates (Badr *et al.*, 2020; Gatalo *et al.*, 2021)
- Limitations: Generalizability, confounding, limited mobility measure

Information processing in autonomous systems

Eric Wendel[3], Joseph Hollmann[1], John Baillieul[2]

[1]The Charles Stark Draper Laboratory, Inc., [2]Boston University, [3]Draper Scholar

ABSTRACT

We present progress towards the construction of **information-theoretic adaptive sensing and control strategies** based on probabilistic matching principles from **communications theory.** Specifically, we design a controller that achieves the control system **input-output capacity** subject to an average input power constraint at the minimum admissible **code rate** necessary for achieving a desired mean square error performance criteria. This provides insights into fundamental **information/energy/accuracy trade-offs** in control and estimation with relevance to a large class algorithms – from LQG controllers to deep neural networks.

Minimum information steering

What control signal bit depth and sampling rate are required to steer a robot to its destination?

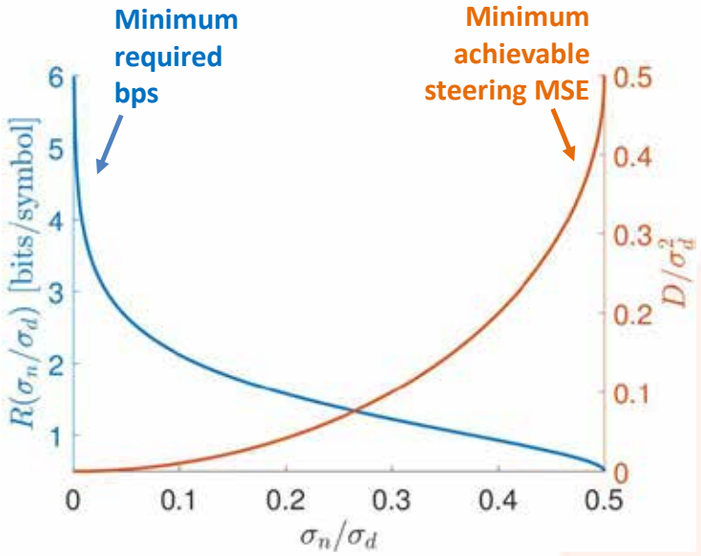

Control system process noise

Control system as communications channel

The information flow rate through a control system is the mutual information between its input and output.

- **Task**: design a controller (encoder) F and estimator (decoder) G that steer a linear system from its uncertain initial condition x_0 to a varying steering objective x_d.
- **Solution**: **maximize the information flow** through the control system while **minimizing the information flow** from the source of uncertainty. This yields probabilistic matching conditions.

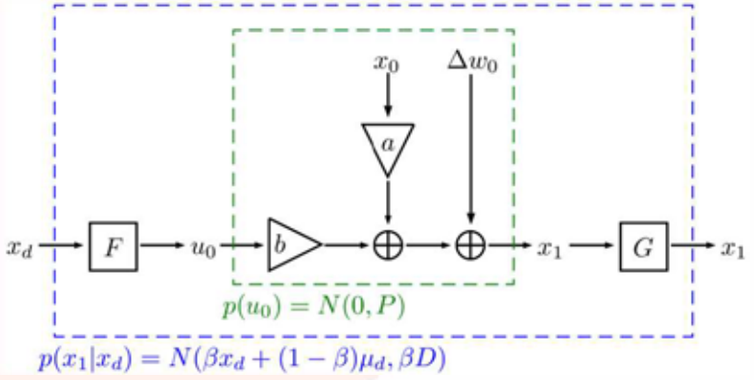

Robot lost in a hallway

How to adapt to visual information?

- **Task**: The robot must avoid obstacles and round the corner without a map and with partial scene knowledge.
- The information-theoretic approach starts from a statistical characterization of algorithms for detection and tracking of visually distinctive features (shown below: ORB + KLT in OpenCV).
- We seek sensing and control strategies based on maximizing and minimizing information flow from the scene through the robot.

Global Localization via Neural Network Powered Computer Vision

Lena Downes[1,3], Ted Steiner[2], Jonathan How[1]

[1]MIT, [2]Draper, [3]Draper Scholar

ABSTRACT

Cross-view image geolocalization provides an estimate of an agent's global position by matching a local ground image to an overhead satellite image without the need for GPS. Cross-view geolocalization is challenging since the images have significant viewpoint differences. Existing works have demonstrated localization in constrained scenarios over small areas but have not demonstrated wider-scale localization. They have also focused on panoramic ground cameras and have not developed uncertainty estimation techniques. My approach, called Restricted FOV Wide-Area Geolocalization (ReWAG), combines a neural network with a particle filter to achieve global position estimates for agents with limited FOVs moving in GPS-denied environments, scaling efficiently to city-scale regions. In the future, I plan to train my neural network to reliably estimate the uncertainty of the network output.

Problem: Unreliable GPS Localization

GPS Jamming

Jamming— bad actor blocking GPS signal from reaching the agent

Spoofing— bad actor feeding the agent false GPS signals

Urban Canyons— GPS signal bouncing off tall buildings and reducing accuracy

Motivating Applications

- Rider pinpointing location for Uber pickup
- Military robot rescuing wounded soldier
- Last mile delivery robotics
- Driverless car driving home

Lost last mile delivery robot

Background

Cross-view Geolocalization

Meaning: match images of vastly different viewpoints

Method: Siamese-like networks

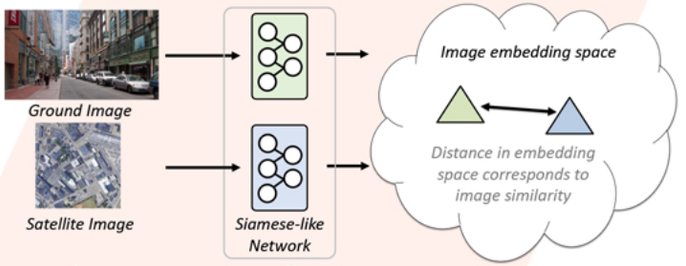

Database Source: satellite images are more widely available and more compressible than ground images

Google Street View Coverage (source: google.com/streetview/explore)

Gaps

Cross-view geolocalization gaps in robotics applications–

1. city-wide temporal localization
2. limited field of view ground camera
3. uncertainty quantification

Contributions

Scalability— improved performance on coarse satellite image database through trinomial loss training with Siamese network

Hardware Simplicity— improved performance on limited FOV images with pose-aware embeddings

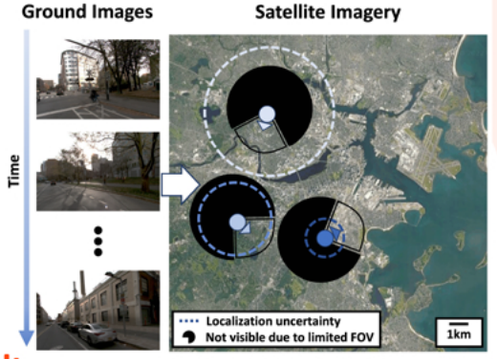

Results

Initial localization error in Boston. Satellite image shows size of search area.

Final localization error of less than 45 m.

Conclusions

We can accurately localize without GPS across city-scale search areas with only images and odometry.

Learning-Enhanced MPC for Fixed-Wing sUAS

C. Alexander Hirst[1,2], Chris Reale[2], and Eric Frew[1]

[1]University of Colorado Boulder, [2]Charles Stark Draper Laboratories

ABSTRACT

Fixed-wing small uncrewed aircraft systems (FW-sUAS) provide a platform for extended information gathering missions. However, their complex and coupled dynamics make precise, agile control challenging. This work enables high performance path-following control by augmenting a nonlinear model predictive control (MPC) algorithm with a learned meta-level policy, which dynamically parameterizes the underlying MPC online. The algorithm demonstrates improved performance with reduced online computation compared the state-of-the-art MPCC baseline.

INTRODUCTION

- Traditional FW-sUAS path-following guidance algorithms limit performance and assume simple paths composed of straight lines and circles.
- FW-sUAS are deployed in stochastic wind fields which significantly influence aircraft dynamics, requiring fast online adaptation with limited onboard computation.
- Model predictive contouring control (MPCC) is a state-of-the-art path-following MPC, but results in a **complex joint optimization** of controls and path reference [1,2].

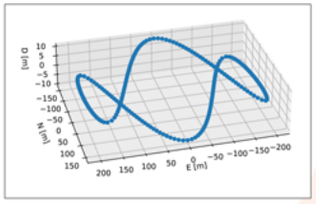

METHODS

- We implement 3D MPCC for FW-sUAS and improve it with a meta-level policy π_{ML} for dynamic parameterization.
- The meta-level policy search is formulated as a stochastic decision-making problem, for which the optimal solution can be approximated using the approximate dynamic programming method one-step lookahead with rollout (OLR-MPC). This expert meta-policy performs well but is too expensive to run online on embedded hardware.
- A learned meta-level policy is trained to imitate the expert – but computationally expensive – meta-level policy using the DAgger algorithm [3]. The learned meta-level policy enables online, onboard deployment (LE-MPC).

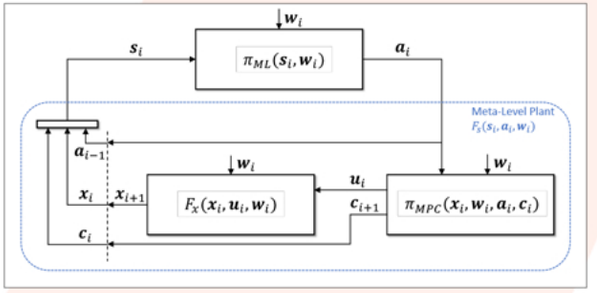

RESULTS

- MPCC, OLR-MPC, and LE-MPC were tested over 500 Monte Carlo runs each, following a 3D Lissajous curve. Stochastic wind fields were simulated using the Dryden turbulence model.

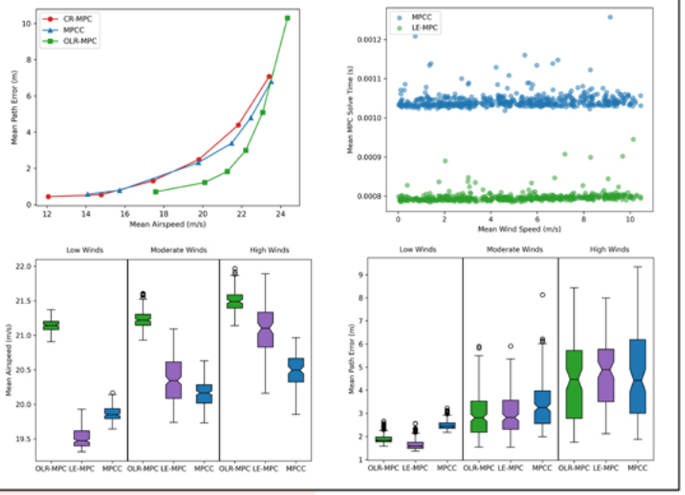

DISCUSSION

- Results were binned by windspeed into low (0-4 m/s), medium (4-8 m/s), and high (8+ m/s) wind conditions.
- OLR-MPC outperforms MPCC in low/moderate/high winds by lower path-following error (-23.0% / -13.4% / -3.5%) and higher average airspeed (+6.4% / +5.3% / +5.0%).
- LE-MPC successfully imitates OLR-MPC via DAgger, outperforming MPCC overall by reducing average path-following error (-14.9%) and increasing airspeed (+0.27%) over the 500 runs. LE-MPC also significantly reduces computation time (-23.7%) compared to MPCC.
- LE-MPC is inherently limited by the performance of the expert meta-level policy. However, the meta-level policy search as formulated is readily admissible to reinforcement learning algorithms, which could improve performance beyond what has been achieved in this work.

CONCLUSIONS

- The proposed algorithm (LE-MPC) combines offline imitation learning with online MPC to achieve **accurate 3D path following** in **dynamic environments** at **higher airspeeds**, with **less computation** compared to state-of-the-art MPCC. The algorithm is formulated to follow arbitrary smooth arc-length parameterized curves.
- Future work will conduct field deployments on the CU Boulder RAAVEN FW-sUAS, beginning summer 2023.

REFERENCES

1. Hirst, C. A., Bird, J. J., Reale, C., & Frew, E. (2022, March). Nonlinear Model Predictive Control for Agile Guidance of Fixed-Wing sUAS. In 2022 IEEE Aerospace Conference (AERO) (pp. 1-11). IEEE.
2. Romero, A., Sun, S., Foehn, P., & Scaramuzza, D. (2022). Model predictive contouring control for time-optimal quadrotor flight. IEEE Transactions on Robotics, 38(6), 3340-3356.
3. Ross, S., Gordon, G., & Bagnell, D. (2011, June). A reduction of imitation learning and structured prediction to no-regret online learning. In Proceedings of the fourteenth international conference on artificial intelligence and statistics (pp. 627-635). JMLR Workshop and Conference Proceedings.

DRAPER

Decentralized Decision Making over Random Graphs

Sam Fedeler (Draper Scholar)[1], Marcus Holzinger[1], William Whitacre[2]

[1]University of Colorado Boulder, [2]Charles Stark Draper Laboratories

ABSTRACT

We propose a novel approach for solving the space domain awareness (SDA) sensor tasking problem using decentralized Monte Carlo Tree Search. Random graphs are used to ensure robust communication and evaluate upper bounds on communication gaps. Asymptotic analysis of the algorithm is conducted to consider the effect of discrete communication on local reward distributions. A simulation using the VADeR observatory is presented alongside theoretic results. This study is the first known methodology to fully decentralize the SDA sensor tasking problem in an optimally convergent manner. Our approach can be extended to other decentralized systems beyond SDA, and it marks a crucial step towards meeting the evolving demands of the near-Earth environment.

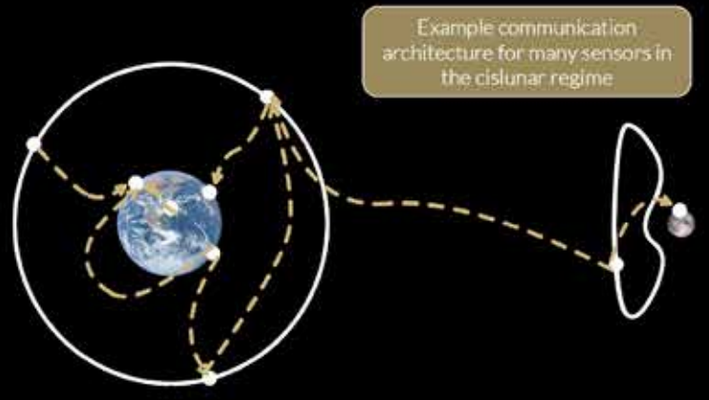

Communication is posed as a regular random directed graph. In such a graph, each node has a specific outdegree k, and we wish to determine the necessary value of k for guarantees in communication. Given the number of agents N and outdegree k, we may probabilistically infer connectivity, robustness to loss of edges, and graph diameter.

Connectivity:

$$P(\mathcal{E}_0) = \left(\frac{\binom{N-1}{k}}{\binom{N}{k}}\right)^N = (1-\frac{k}{N})^N \approx e^{-k}$$

$$P(\lambda(D) \geq 1) = (1 - P(\mathcal{E}_0))^N = (1 - e^{-k})^N$$

We find the minimum number of communication intervals k to determine connectivity with probability $\Delta^{\frac{1}{N}}$. Further results in robust connectivity in paper.

$$k = -\text{floor}\{\log(1 - \Delta^{\frac{1}{N}})\}$$

Diameter:

$$d(G,k) = (1 + \eta_k + o_N(1)) \log n$$

Diameter maximally bounded by Addario-Berry et al.

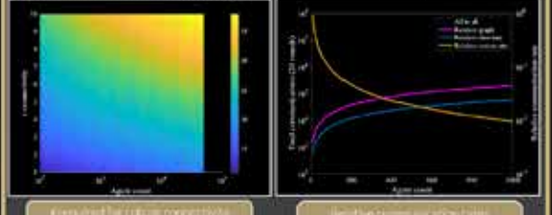

k required for robust connectivity against agent count.

Relative communication rates compared to ADeR and directed random graph architectures.

We assume agents forward their current best action trajectories alongside those of any other agents they are aware of. This may change the local value of an action for an agent, making the problem **nonstationary** in a discontinuous manner!

Random Graph Guarantees

We apply asymptotic analysis of the immediate multi-armed bandit (MAB) problem then extend that analysis to a hierarchical tree of bandits. This problem is modified from a traditional MAB in that "breakpoints" may occur, where the payoff distribution of an action may suddenly change (because of new information about what other agents might do!).

We apply a policy called D-UCB as follows: In search, choose the action that maximizes the upper confidence bound in payoff, discounting less recent results.

$$I_t = \max_{i \in \{1,\dots,K\}} \bar{X}_{i,t}(\gamma) + c_{i,t}(\gamma)$$

$$\bar{X}_{i,t}(\gamma) = \frac{1}{N_{i,t}(\gamma)} \sum_{s=1}^{t} \gamma^{t-s} X_s \mathbb{1}_{\{i_s = i\}}$$

$$c_{i,t}(\gamma) = 2B\sqrt{\frac{\xi \log(n_t)}{N_{i,t}(\gamma)}} \qquad n_t(\gamma) = \sum_{i=1}^{K} N_{i,t}(\gamma)$$

Asymptotic analysis:

1) $E_T[\bar{N}_i(t)] = O(t^{\frac{1+\beta}{2}} \log(t))$

2) $|E_T[X_t] - \mu^*| \leq |\delta_T^*| + O(|\mathcal{A}| t^{\frac{\beta-1}{2}} \log(t))$

3) $P(|X_t - E\,X_t| \geq \Gamma_t) \leq \epsilon$

$\Gamma_t = 2\sqrt{2 n_t (2\gamma)^{\beta-1}} \frac{1+\sqrt{\gamma}}{1-\sqrt{\gamma}} < \alpha < 1$

4) $|\bar{X}_{i,n_{i,t}} - \mu_{i,t}^*| = O(|\mathcal{A}| t^{\frac{\beta-1}{2}} \log(t))$

Note: breakpoints occur as: $E[\Upsilon_t] = O(t^\beta), \quad \beta \in [0,1)$

1) Upper bound on the selection of suboptimal actions
2) Convergence of expected payoff converges to optimal payoff
3) Concentration of the payoff about the expected payoff
4) Extend analysis from a MAB to a tree

Implication: The resultant methodology will converge to the locally optimal action for an agent over time. Further analysis is needed to consider the potential for globally suboptimal "trap states", but numerical analysis in the following example demonstrates promising initial results.

Theoretic Convergence

The algorithm is characterized using a weeklong geostationary tracking simulation of 202 objects with the Vision, Autonomy and Decision Research (VADeR) observatory.

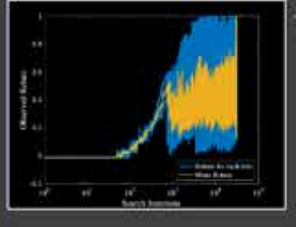

1)

1) Observed returns (with mean alongside tree search iterations), demonstrating numerical convergence of the algorithm. Note growth in potential returns alongside exploration of suboptimal actions—this is good behavior!
2) Unique objects observed by each sensor, demonstrating full joint custody of the catalog while each sensor cannot maintain the catalog by itself.
3) Object positional covariance bounds over time, demonstrating steady state custody of all objects.

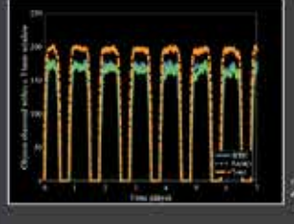

2)

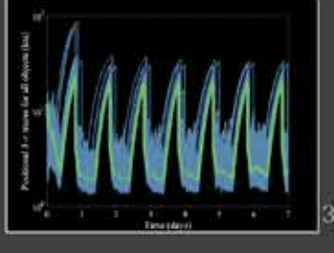

3)

These results demonstrate that the two sensors we house at CU may successfully maintain custody of the local geostationary environment. Note these are initial results with inflated assumptions on process noise and the time to observe an object. However, these results also assume nightly observation, which simply isn't feasible with Boulder weather conditions. I am currently applying this research to the observatory itself, so we will fortunately have the opportunity to present realistic results! Empirical validation with the VADeR observatory will be presented at AMOS 2023 — keep tuned!

Simulated Results

Questions? Feel free to reach out at samuel.fedeler@colorado.edu!